Surface X-ray Diffraction Studies of the Electrochemical Interface

by

Gary Steven Harlow

Oliver Lodge Laboratory, Department of Physics

University of Liverpool

This thesis is submitted in accordance with the requirements of the University of Liverpool for the degree of Doctor of Philosophy

October 2016

Viva Voce Examination

15:30, 23rd June 2016

Oliver Lodge Building, University of Liverpool

Examiners

Prof. Andrea E. Russell

Department of Chemistry, University of Southampton

Prof. Peter Weightman

Department of Physics, University of Liverpool

PhD Advisors

Primary: Prof Christopher A. Lucas

Secondary: Dr Vinod R. Dhanak

DECLARATION

I, Gary Steven Harlow, declare this thesis is a presentation of my own work except where indicated in the text. It has not been previously submitted, in part or whole, to any university or institution for any degree, diploma, or other qualification.

Gary Steven Harlow

31st March 2016

Signed: *Original submitted copy signed: Gary Harlow*

ABSTRACT

This thesis describes the application of *in-situ* surface X-ray diffraction (SXRD) experiments to the study of electrochemical interfaces. Measurements performed at synchrotron radiation facilities are used to provide in-sight into the surface structure of electrodes and the electrochemical double layer. The impact of structural changes on electrochemical reactivity, and likewise the impact of electrochemical processes on electrode structure are discussed. Measurements of the Au (111) reconstruction in alkaline solution indicate that the presence of CO causes the partial lifting of the reconstruction; it is suggested that this leads to an increase in defects and this is the underlying reason for CO promoted gold catalysis. *In-situ* SXRD measurements with a non-aqueous electrolyte are presented, representing a technological advance in the study of electrochemical interfaces. Crystal truncation rods (CTRs) measured at the Pt (111) / non-aqueous acetonitrile interface are used to determine the structure of both the electrode surface and the electrolyte close to the interface. The results indicate that acetonitrile undergoes a potential dependant reorientation but, in the presence of molecular oxygen, the acetonitrile molecules close to the electrode are dissociated and therefore cannot reorient. Measurements of CTRs at the Pt (111) / electrolyte interface for several aqueous electrolytes are combined with CTRs measured in non-aqueous acetonitrile to explore the dependence of surface relaxation on adsorption. Fits to CTRs are also used to determine the double layer structure at aqueous Pt (111) / acetonitrile interfaces and how it varies with acetonitrile concentration. The results indicate that the acetonitrile adsorption increases with concentration and that the double layer region compresses.

ACKNOWLEDGEMENTS

I would like to thank my supervisor Professor C.A. Lucas for introducing me to surface X-ray diffraction and its combination with electrochemistry, his continuing support throughout my PhD, and his rare dedication and enthusiasm to science.

Thank you to Dr N.M. Markovic for allowing use of his lab at Argonne, and his former to postdocs Jakub Staszak-Jirkovský and Ram Subbaraman for helping with the preparation of experiments. Paul Thompson deserves a huge thank you for all his help with experiments, chauffeur services, and advice about the best bars in Chicago. Keith Williams from the physics workshop deserves a mention for all the work he has put into the construction of the electrochemical cells and sample environments. Thank you to Kayla Friedman and Malcolm Morgan (Cambridge, UK) for producing the template used to produce this document.

Many thanks to Dr V. Dhanak for giving me the opportunity to work in his laboratory and learn all about UHV and surface science, also to Ian McLeod, and David Hesp for training me in the use of UHV equipment. Thank you to Naomi Sisson for teaching me the proper way to do electrochemistry.

I would like to thank my friend (and work wife) Elizabeth Cocklin for the many cups of tea, gossip, proof reading, and excellent conversation. Thank you to Iain Aldous for his many late nights at the synchrotron, drinking sessions, and general humour. Also Dr L.J. Hardwick for his enthusiasm, experimental help and heated star trek debates.

Last but not least I would like to thank Janette Roberts (Grandma) for her unwavering support, without which thesis would not exist.

CONTENTS

LIST OF APPENDICES

1 INTRODUCTION

The discipline of electrochemistry underpins many technologies, such as those for the storage of energy, electroplating, the extraction of metal ores, the processing of chemicals, and sensors for a variety of chemical substances. In the majority of electrochemical systems there exists a junction between a solid metal conductor (the electrode) and a liquid ionic conductor (the electrolyte). The interfacial region where these two mediums meet is known as the electrochemical interface and its structural and electronic composition has a profound effect upon almost all electrochemical processes. A greater understanding of such interfaces is therefore expected to lead to advances in the many fields which depend upon electrochemical systems.

Cyclic voltammetry, the measurement of current as a function of potential, is the primary tool of electrochemistry. This technique provides a wealth of information about the transfer of electrons but lacks any true chemical or structural sensitivity. A brief overview of electrochemistry, the electrochemical interface, and voltammetry is given in Chapter 2. To gain a more complete picture voltammetry must be combined with spectroscopic techniques, and if the interfacial region is to be investigated, these must be

surface sensitive. Unfortunately, many of the techniques commonly used to investigate surfaces rely on ultra-high-vacuum (UHV) and the free movement of electrons. Some success has been achieved with *ex-situ* measurements where an electrode is transferred from an electrochemical cell directly to a UHV chamber [1–4]. The idea is that when the electrode is removed part of the double layer structure that forms at the interface will remain on the electrode [5]. The problem with this approach is that in the absence of both electrolyte and potential control one can never be completely confident that the interface is equivalent to its true electrochemical analogue. It is therefore preferable to make measurements *in situ*, i.e. in an electrochemical cell with potential control. Optical techniques such as infrared, surface enhanced Raman and sum frequency generation spectroscopies are able to provide information about the chemical nature and even the orientation of chemical species close to the electrode surface. However, if one wants to know the atomic scale structure of either the electrode or the arrangement of species close to it, there are really only two techniques capable of providing this information. Scanning tunnelling microscopy (STM) is one option but it can be extremely time consuming, imaging mobile species such as silver or gold at room temperature represents a significant challenge. The alternative, *in-situ* surface X-ray diffraction (SXRD) is the principle technique used throughout this thesis. SXRD is capable of simultaneously providing information about the surface of an electrode and the electrolyte above it. The principles behind surface diffraction are discussed in Chapter 3 but there are also several comprehensive reviews available [6–9]. One of the drawbacks of *in-situ* SXRD is that an intense X-ray source is required, typically this is a synchrotron. The principle behind synchrotron radiation and the details of how to perform an *in-situ* SXRD experiment are discussed in Chapter 4.

A major feature of electrochemical surface science is the use of single crystal electrodes. If one is to study the interface of an electrode, that electrode should be well defined. A single crystal can have a surface that is terminated at a particular crystal plane of atoms. The surface structure of a single crystal does not necessarily have the same arrangement as the bulk of a crystal. The termination of the bulk often leads to the surface reconstructing (in which it has a different periodicity) or relaxation (in which the surface layers are expanded or contracted away from the bulk position). Such differences are a manifestation of the thermodynamic need to find a minimum energy configuration because the local electronic environment of the atoms at the surface is different to that of atoms in the bulk. What is more is that in the electrochemical environment both relaxation and reconstruction are affected by potential, however most models of the electrochemical interface assume the positive cores of the atoms in an electrode remain static.

The activity of gold in both heterogeneous and electro catalysis can be surprisingly high, and yet, the driving force for such behaviour remains largely unknown. The Au (111) surface in aqueous alkaline media is a pertinent example, where adsorbed carbon monoxide acts as a promoter for the electro-oxidation of certain alcohols. The onset of oxidation towards formaldehyde seems to occur at a lower potential in the presence of adsorbed CO [10]. This effect is only seen on hexagonal Au (111) and hexagonally reconstructed Au (100) faces, which suggests a structural link; where both surfaces are reconstructed at negative potentials in alkaline media. In Chapter 5 SXRD is used to explore the potential dependence of the Au (111) reconstruction and its modification by CO adsorption. Measurements made in the presence of methanol and ethanol are also examined. The results suggest that both CO and methanol cause a partial lifting of the surface reconstruction whereas ethanol seems to protect it. It is suggested that this partial lifting increases the number of catalytically active defect sites. In the

baseline alkaline solution, a potential induced change in lateral compression is also observed. at a potential just before a voltammetric feature that has been previously reported and linked to the surprising enhancement of gold catalysis by carbon monoxide. This chapter highlights the intimate relationship between electrode structure and chemical reactivity in gold electrocatalysis.

Non-aqueous electrolytes have been extensively studied across many biological and energy storage systems and play a crucial role in many future energy technologies. In particular the reduction of O_2 in non-aqueous electrolytes has been widely investigated; this is the key reaction in lithium oxygen batteries [11–13] . The high theoretical energy density of Li-O_2 batteries has the potential to transform energy storage[14]; therefore an increased fundamental understanding of non-aqueous interfaces could be considered as a pre-requisite to further technological development. In Chapter 6 the application of *in-situ* SXRD is extended to non-aqueous interfaces with the introduction of a new design of electrochemical cell. The natural choice for this first non-aqueous study is acetonitrile (MeCN) with a Pt (111) electrode. MeCN is one of the most studied non-aqueous electrolytes for oxygen reduction because of its relative stability towards reduced O_2 species [15]. The Pt (111)/MeCN aqueous interface is also notable because of the interesting chemisorption properties of acetonitrile; MeCN can undergo reversible reduction and re-oxidation without any desorption of the products. In contrast, in non-aqueous acetonitrile the MeCN molecule is thought to undergo a potential dependant change in its orientation at the Pt (111) interface. In Chapter 6 *in-situ* SXRD measurements showing how this interface behaves both with and without the presence of molecular oxygen are presented. The use of non-aqueous solvents also opens up a greater potential range and allows the investigation of many phenomena previously inaccessible to SXRD.

Platinum is one of the most important (and therefore studied) electrode materials in electrochemistry because of its high catalytic properties; especially towards oxygen and hydrogen evolution, key reactions in fuel cell technologies [16]. Both the effects of anion adsorption and the interaction between cations in the double layer impact the reactivity of such interfaces. In Chapter 7 SXRD measurements of the Pt (111)/electrolyte interface are presented for a variety of electrolytes with different anions ($HClO_4$, H_2SO_4, and KOH). The effect of MeCN concentration in $HClO_4$ electrolytes and how this affects the structure of the electrochemical interface is then investigated. Linking up measurements of surface relaxation for the aqueous systems measured in Chapter 7 with the non-aqueous data presented in Chapter 6 allows the relationship between relaxation and adsorption to be investigated. In particular measurements made in the absence of hydrogen in aprotic MeCN can be used to separate field induced effects from adsorbate induced effects. Measurements of surface relaxation as a function of potential in several electrolytes are used to further understand adsorption processes.

2 ELECTROCHEMISTRY AT METAL/LIQUID INTERFACES

When two phases with different chemical potentials (Fermi-levels) are in contact the tendency will be to equalise their chemical potential through an exchange of charge. This generally results in the formation of one or more double layers at the interface, that is layers with equal but opposite charge. For a metal this induced charge is found at the surface, as opposed to a semi-conductor where a lower free-carrier density can result in the charge being distributed over large distances from the surface. For liquids, ionic species provide the charge for equilibration with another phase. Electrochemistry is an important and vast area of science that is interested in phenomena at electrode-electrolyte junctions, with the application of a potential. The electrode and electrolyte are of different phases where the most common situation is a metal-liquid junction.

In this chapter a basic description of electrochemistry at metal-liquid interfaces is presented[1]. The chapter will begin with a description of chemical reactions at electrodes and the effect of potential; followed by a discussion of the various 'double layer' models. This is followed by a derivation of the Butler-Volmer equation for single electron transfer and finally a discussion of cyclic voltammetry.'

[1] *Source material is references* [17–22] *which also make excellent further reading.*

2.1 Electrode Reactions

While charge in a metal is carried by electrons, in a liquid electrolyte it is carried by ions. At the metal-electrolyte interface the conversion between ionic and electric charge occurs as a result of electron transfer. At its most basic an electrochemical cell consists of two electrodes and the electrolyte. The electrode where electrons transfer from the electrolyte to the electrode is called the anode whereas the electrode where electrons are transferred from the electrode to the electrolyte is the cathode. Therefore, in an electrochemical cell there are two spatially separated half-reactions, an oxidation reaction at the anode, and a reduction reaction at the cathode. This is summarised with the following chemical reactions, where x, y are the stoichiometric coefficients and n is the number of electrons.

$$\begin{aligned} xR + ne^- &= yO \quad \text{(reduction at cathode)} \\ yO &= xR + ne^- \quad \text{(oxidation at anode)} \end{aligned} \tag{2.1}$$

The atom or molecule to be reduced is the oxidant, O, whereas the species to be oxidised, R, is the reductant. Taken together O and R form a redox couple. Whether a particular reaction occurs or not depends upon the cell potential; the potential difference between the two electrodes which exists even in the absence of current. Conceptually this cell potential can be divided into an individual electrode potential for each electrode. The electrode potential corresponding to one of the half reactions above is called the redox potential, of that reaction. Electrode potentials cannot be directly measured; instead they are compared against a standard reference electrode. The traditional standard reference is the normal hydrogen electrode (NHE) and consists of a platinum black electrode in hydrochloric acid in equilibrium with hydrogen gas where the activities are unity. The equilibrium reaction is:

$$H^+ + 2e^- \rightleftharpoons H_2 \tag{2.2}$$

Electrode redox potentials can be measured (with respect to NHE) by making the second electrode NHE. The redox potential of a given half reaction is denoted E^o. When the potential of the electrode (against NHE) is made more negative, the energy of the electrons is increased and they are more likely to transfer to the electrolyte species (reduction). Conversely when the electrode is made more positive, electrons from species in the electrolyte are more likely to transfer to the metal (oxidation). The overall chemical reaction in a cell will have a change in Gibbs free energy (ΔG) related to the cell potential (E_{cell}) as in equation 2.3. Where the Gibbs free energy is the difference between enthalpy and the product of temperature and entropy, the more negative ΔG the more favourable the reaction. F denotes the Faraday constant.

$$\Delta G = -nFE_{cell} \tag{2.3}$$

If all the reactants in the electrochemical cell have an activity of one (a = 1), where activity is the effective concentration once factors such as temperature and pressure are considered, then this will become:

$$\Delta G_0 = -nFE^0_{cell} \tag{2.4}$$

Tables of the standard electrode potentials (E^o) are available and the cell potential will be the sum of the standard electrode potentials for each of the half reactions (where careful attention is needed with the signs). That is:

$$E^0_{cell} = E^\ominus_R + E^\ominus_O \tag{2.5}$$

Therefore, the direction of the cell reaction that is thermodynamically favoured can be determined. Even when the activity is not unity the Nernst equation (2.6) can be used to convert the standard redox potentials to a suitable potential.

$$E = E^{\ominus} + \frac{RT}{nF} ln \frac{a_{Ox}}{a_{Red}} \quad (2.6)$$

In the Nernst equation R is the universal gas constant (~8.3 J K^{-1}), T the absolute temperature and $a_{ox/red}$ the activity of the reductant and oxidant. When the electrode potential is equal to the redox potential there will be a dynamic equilibrium. The net current will be zero but there will be electrons flowing in both directions. A net current, however, can be induced by increasing or decreasing the electrode's potential, the difference between E^{o} and the actual potential is called overpotential (η). Often the Tafel equation (2.7) is used to describe the relationship between overpotential and current (i).

$$\eta = a + b \log i \quad (2.7)$$

Where a and b are constants for a given electrode/reaction. If a small overpotential produces a large current the electrode is considered efficient for that half-reaction.

2.2 Electrical Double Layers

It was mentioned in the introduction to this chapter that the formation of one or more double layers results whenever two separate phases with different chemical potentials are brought into contact. The first theory of an electrical double layer at the metal-liquid interface was proposed by Helmholtz in 1853. Essentially the model recognises that if the charge of the metal electrode is q^{m} then in order for interface to remain neutral it must be matched by a solution charge q^{s} such that:

$$q^m = -q^s \tag{2.8}$$

This happens through a rearrangement of ions and molecules in the electrolyte. A potential gradient at the interface causes ions to be either attracted to or repelled from the electrode. In this model there is a build-up of charge in a layer close to the electrode surface. It is assumed that a solvation shell surrounds the ion cores preventing them directly contacting the electrode. The plane parallel to the electrode through the centre of the ions closest to the electrode is known as the Outer Helmholtz Plane (OHP) in modern terminology. The net charge of the ions in the OHP and the charge of the electrode are assumed to perfectly balance. Later in 1910 Gouy [23], and independently Chapman , proposed an alternate model. They said that there are no defined layers of ions but instead a distribution of diminishing charge out from the electrode, the ions were assumed to be point like. Such a model, however, fails when an electrode is strongly polarised, it predicts an infinite charge close to the electrode. In reality the size of ions and their solvation shells will impose a limit on the number of ions that can approach the electrode. A solvation shell is the layer of solvent species that surround ionic species, bonded for example through hydrogen bonding. Stern solved this by combing the Gouy-Chapman and Helmholtz models in 1924 [24]. In this model there is a layer of charge in the OHP, but the electrolyte remains electro-neutral through a diffuse region out towards the bulk electrolyte. Stern also introduced the idea of an inner Helmholtz plane (IHP) but the concept was only later fully developed by Grahame [25]. This is a layer of closest approach consisting of ions with only a partial solvation sheath in contact with the electrode, perhaps even chemically bonded to the electrode. This remained unchanged until Bockris and Potter [26] suggested that in a polar solvent (i.e. water) the dipolar properties lead to it preferentially ordering at the electrode's surface in a solvent layer (SL). Up until the 1980s the potential at the metal interface was generally considered a

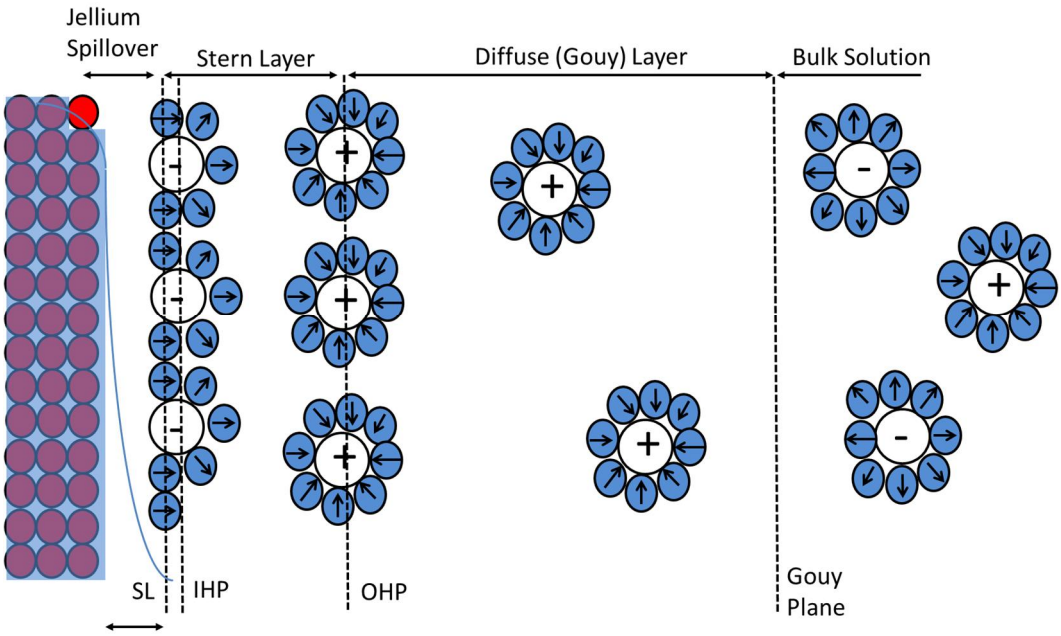

Figure 2.1. Schematic to illustrate the double layer model described in the text. SL is the solvent layer, IHP and OHP are the inner and outer Helmholtz planes. Arrows indicate the direction orientation of solvent molecules.

sharp step function, the idea of a continuous electron distribution out from just inside the electrode into the electrolyte was mainly developed by Goodisman [27] and then Schmickler [28]. In this model the metal electrode is modelled as jellium, i.e. a uniform electron gas over a smeared out positive background that is a step function at the electrode surface. The electron plasma penetrates into the electrolyte because of the small relative mass of an electron. The electron density has a decay constant of about 0.5 Å and the distance just inside the metal where the electron density decays from a constant is called the Thomas-Fermi length (which is around 1 Å). The jellium model however is best suited to polycrystalline metals where local effects due to crystal structure are averaged out. For single crystals, efforts have been made to replace the positive background with

pseudopotentials (e.g.[29]). In Figure 2.1 an overview of the model presented in this section is illustrated.

2.3 Cyclic Voltammetry

In general, there is detailed information to be gained from measuring the current response as a function of potential, this is known as voltammetry. Unfortunately, if a large current is required there will be an appreciable voltage drop due to the passage of current in the solution phase. The potential difference between a working electrode and a reference electrode is given by:

$$E_{cell} = (\phi_m - \phi_s) + (\phi_s - \phi_{ref}) + iR \qquad (2.9)$$

The three terms represent a voltage drop at the metal solution interface$(\phi_m - \phi_s)$, a voltage drop at the reference electrode interface $(\phi_s - \phi_{ref})$ and an Ohmic voltage drop due to passage of current in the solution$(\mathbf{iR})$. In order to measure the voltage drop at the working electrode as a function of current (voltammetry) the last term needs to be negligible. The potential drop at the reference electrode should be constant, but a large current can also affect the stability of such an electrode. To resolve this a 'three electrode' setup is often used. The reference electrode is given an extremely high impedance and is used to control the potential, whereas an additional **co**unter electrode completes the current path. Figure 2.2 illustrates the standard three electrode experimental setup for the study of a single crystal electrode. There is a working electrode where the reaction of interest takes place and a reference electrode that sits inside a luggin capillary

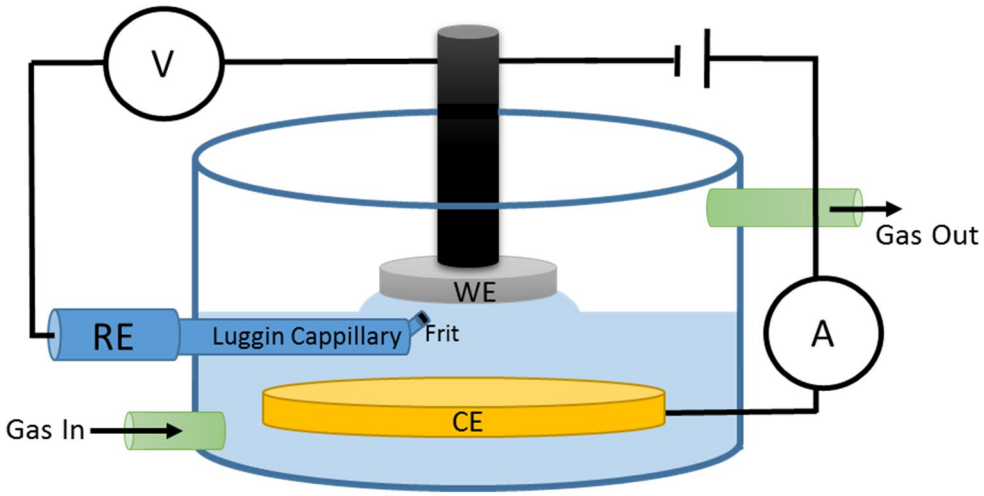

Figure 2.2: Illustration of a three electrode electrochemical cell. WE, CE, and RE are the working, counter, and reference electrodes respectively. A luggin capillary with a fritted end prevents any reaction products altering the potential of the reference electrode. The working electrode is in the so called 'hanging meniscus' geometry.

allowing a well-defined small reference point near the working electrode to be measured. There is a counter electrode which should have a surface area much larger than the working electrode so that half-reactions at this electrode can occur quickly and not affect those at the working electrode.

In a cyclic voltammetry experiment the potential starts at E_1 and is swept linearly at a rate v_s to a potential E_2 and then back to E_1. In the negative going sweep a species A is reduced to a species B and on the reverse sweep B is oxidised to A. If one assumes an outer-sphere single electron transfer reaction, the current will initially remain constant until the electrode is positive enough for electron transfer to occur. The current will then begin to increase exponentially (in accordance with Butler-Volmer kinetics) until it reaches a maximum determined by the diffusion of species A to the electrode surface. With yet further overpotential the current begins to reduce as the path required for

diffusion increases. The region closest to the electrode, devoid of species A, expands outwards. The opposite happens on the reverse cycle. A cyclic voltammogram is shown in Figure 2.3. For a reversible reaction the peak potentials will be unaffected by sweep rate v_s, whereas for irreversible reactions they will shift by $\sim\frac{RT}{\alpha F}$ for every factor of 10 the sweep rate increases by. The difference between the two peaks at 25 °C will be 59 mV for a single electron transfer, for n electrons it will be:

$$|E_p^{ox} - E_p^{red}| = 2.218\frac{RT}{nF} \quad (2.10)$$

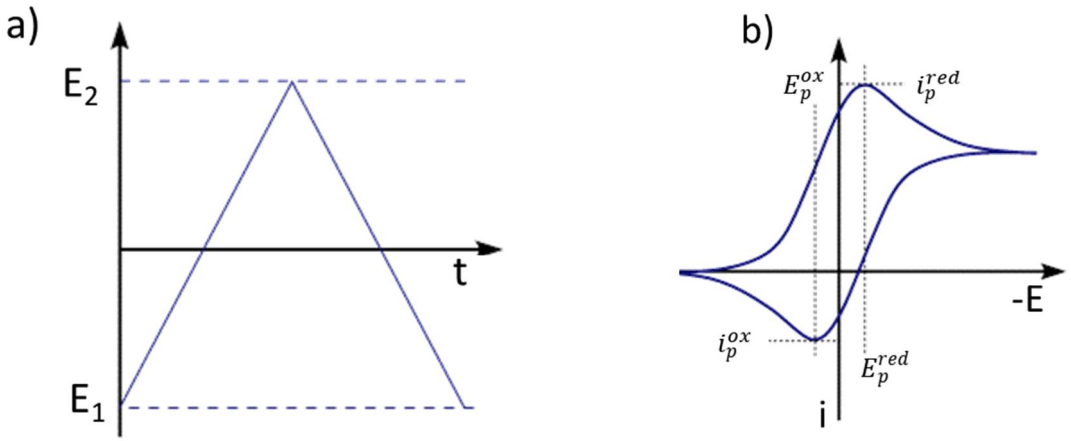

Figure 2.3: Cyclic voltammetry. a) Graph showing the variation of potential with time for one cycle of cyclic voltammogram. b) This is a typical voltammogram, the graph shows the variation of current with potential for a reversible reaction. I_p and E_p are the peak currents and potentials shown both for the oxidation and reduction reactions.

3 SURFACE X-RAY DIFFRACTION

In 1912 Max Von Laue, after a conversation with Ewald, wanted to find out whether with a suitable wavelength (i.e. X-rays) the ordered array of atoms in a crystal would act like an optical diffraction grating. Although Sommerfeld, his supervisor at the time, believed that the thermal motion of atoms would distort any such grating too much to be useful; Laue along with two technicians (Knipping and Friedrich) managed to 'borrow' equipment from elsewhere and preform experiments that eventually won Laue the 1914 Nobel Prize in physics [30].

Surface X-ray diffraction is the central measurement technique used in the work to be presented, this chapter establishes the main principles behind X-ray diffraction and in particular its application to surfaces. The approach taken begins with the traditional idea of an optical diffraction grating and builds up a theory of atomic diffraction, this will involve considering the interaction of X-rays with real atoms, the symmetry of crystals and the thermal motion of atoms. Additionally, the contribution that an electrolyte makes to the diffraction pattern is considered. The structure factor for the (111) face of a face-centred cubic crystal is calculated as it is most relevant to the work later presented in this thesis.

3.1 Optical Diffraction Gratings

Consider the case of optical diffraction[1], a wave front meets several periodically spaced apertures and forms new wave fronts, as these progress - they interfere. Where peak meets peak, or trough meets trough, the intensity is greater but where peak meets trough destructive interference occurs, resulting in less intensity. When an optical screen is placed in the path of the progressing wave this interference, or diffraction, pattern can be seen. If one were to rotate and move the screen freely, or better yet create a 3D map of the diffraction pattern using some form of photo-counter they would discover that a 1D grating creates planes of intensity, and the 2D grating leads to rods of intensity.

The type of diffraction that occurs from an aperture such as those in a diffraction grating is known as Fraunhofer diffraction, and generally is the Fourier transform of the aperture. However, when apertures are arranged periodically we can gain a lot of information about their arrangement from assuming that pattern is a sum of complex amplitudes, that is:

$$Ae^{i\varphi} = f\sum_{N=0}^{N-1} e^{iN\delta} = f\,\frac{1 - e^{iN\delta}}{1 - e^{i\delta}} \qquad (3.1)$$

Where the summation is evaluated using the standard formula for summing a geometrical progression. Since the contribution from each aperture will have equal magnitude, this can be taken out as a common factor, f. N is the number of slits, and δ is the phase

[1]*The approach generally follows that taken by Jenkins and White in their book on optics* [31] *(see page 357, 4th Ed.) with further elaboration on phase/path differences and substitutions to aid the transition to atomic gratings in the next section.*

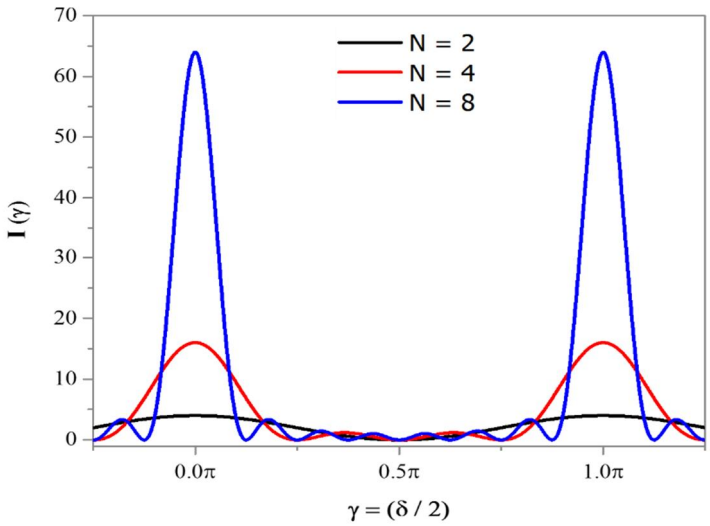

Figure 3.1. N-Slit interference function showing that as a function of phase diffrence the interference/diffraction maxium occur at ineger multiples of γ=δ/2. The intesnity maxium is also a function of the number of slits, $I=N^2$.

difference from one slit to the next. The intensity is calculated by multiplying equation 3.1 with its complex conjugate:

$$\boldsymbol{I(\delta) = A^2 = |f|^2 \frac{(1 - e^{iN\delta})(1 - e^{-iN\delta})}{(1 - e^{i\delta})(1 - e^{-i\delta})}} \qquad (3.2)$$

Then combining equation 3.2 with Euler's formula and the substitution γ=δ/2 we arrive at:

$$\boldsymbol{I(\gamma) = |f|^2 \frac{\sin^2(N\gamma)}{\sin^2(\gamma)}} \qquad (3.3)$$

The factor $\frac{\sin^2(N\gamma)}{\sin^2(\gamma)}$ represents the interference of N slits and is known as the N-slit interference function. Maximum values can be found where γ is an integer multiple of π

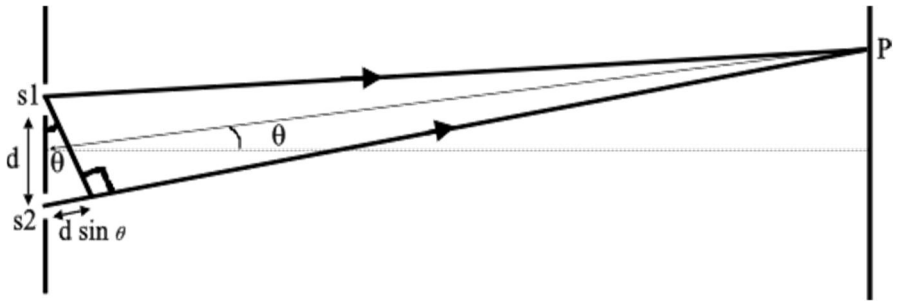

Figure 3.2. Illustration indicating how the oath difference between two diffracted waves is calculated. This is the difference in path between a wave leaving slit s1 and a wave leaving slit s2 at some point P defined by its angle θ to the central axis.

(i.e. γ= 0, π, 2 π, ...). This is shown graphically in Figure 3.1, where the peaks become sharper as N increases. The peaks where γ is an integer multiple of π are known as the principle maxima. By taking limits as γ tends to nπ it can be found that the maximum intensity of each principle maxima is N^2.

Between two principal maxima there will also be N – 1 minima and N – 2 secondary maxima, where the intensity is much less than the principle maxima. The secondary maxima that are closer to the principle maxima have greater intensity. Since the phase difference will simply be $2\pi \times \Delta path/\lambda$, that is the fraction that the path difference is of the wavelength, the phase difference, δ, is given by equation 3.4. Where the path difference can be obtained from the geometrical construction in Figure 3.2.

$$\boldsymbol{\gamma = \frac{\delta}{2} = \frac{\pi d \sin\theta}{\lambda}} \qquad (3.4)$$

Combining equation 3.4 with equation 3.3 the interference of a 1-dimensional diffraction grating can be calculated as eqn. 3.5.

$$\boldsymbol{I(\theta) = |f|^2 \frac{\sin^2(N\pi d \sin\theta/\lambda)}{\sin^2(\pi d \sin\theta/\lambda)} = |f|^2 S_1(N, d, \theta, \lambda)} \qquad (3.5)$$

A similar argument as above can be used to extend the function to describe a 2-dimensional grating.

$$\boldsymbol{I_{2d}(\theta) = |f|^2\, S_1(N_1, d_1, \theta, \lambda)\, S_2(N_2, d_2, \theta, \lambda)} \tag{3.6}$$

An interesting historical aside [31] to consider before moving the discussion onto atomic diffraction gratings is that of 'ghosts'. Before the advent of the laser, the manufacture of good quality diffraction grating was extremely difficult, and even now no diffraction grating is perfect. There will always be deviations from the ideal grating. Most of these errors can be classified as random or periodic. Random errors will affect the width of the maxima and periodic ones will give rise to false lines known as 'ghosts'. A further type of fault is a continually increasing one, this will give the grating a kind of focal property. Since no real crystal will be perfect we should also expect these kinds of effects from atomic diffraction gratings.

3.2 Atomic Diffraction Gratings

The goal now is to apply the method and principles introduced above to atomic diffraction gratings[1]. The main assumption is that the atoms are arranged in a periodic manner, i.e. a basis is translated along three lattice vectors $\mathbf{a_1}$, $\mathbf{a_2}$, and $\mathbf{a_3}$. One major difference from an optical grating lies in that the electrons of atoms **reflect** the incident waves. Generally, it's not the interference of waves that have traversed the grating via

[1] *A combination of the various approaches and derivations given in references* [6–9,32] *are presented. Individual equations are not referenced since they frequently occur and can mostly be derived from basic considerations.*

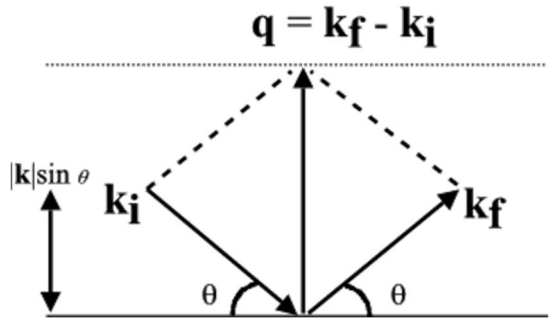

Figure 3.3. Illustration showing how momentum transfer, q is calculated**.** It is easy to see that the magnitude of the vector q is given by: |**q**|= 2|**k**|sinθ = $\frac{4\pi}{\lambda} sin\theta$. This is the fundamental quantity conserved in elastic scattering.

different paths but rather their interference as they are reflected back from different layers of a crystal, a process known as Bragg diffraction[33], that is of interest.

The process by which electrons 'reflect' X-rays is known as Thompson scattering [34] and classically is the result of X-rays causing an electron to oscillate and thereby radiate a secondary spherical wave with equal wavelength. The wave $A_f e^{(-i\boldsymbol{k_f}\cdot\boldsymbol{r_e})}$ at a radial distance R_0 that results from the scattering of an incident wave $A_i e^{(-i\boldsymbol{k_i}\cdot\boldsymbol{r_e})}$ by an electron at $\mathbf{r_e}$ is given by the Thompson formula[34]:

$$\boldsymbol{A_f e^{(-ik_f\cdot r_e)}} = \boldsymbol{A_i \frac{e^2}{4\pi\epsilon_0 mc^2} \frac{1}{R_0} e^{(-ik_i\cdot r_e)}} \qquad (3.7)$$

In Figure 3.3 the useful concept of moment transfer is defined; we can use this and the substitution $r_0 = \frac{e^2}{4\pi\epsilon_0 mc^2}$ (known as the Thompson scattering length) to rewrite equation 3.7 in a simpler form:

$$\boldsymbol{A_f = A_i \frac{r_0}{R_0} e^{(-iq\cdot r_e)}} \qquad (3.8)$$

It seems intuitive that since waves are reflected in atomic diffraction, the path difference will be twice that of the waves that were transmitted in the optical case. The diagram in Figure 3.4 gives a construction showing this path difference. For the interference to be constructive the path difference must be some integer multiple of the wavelength, this is formalised in equation 3.9 and widely known as Bragg's law[33].

$$2d_{hkl}\sin(\theta) = n\lambda \tag{3.9}$$

The two crystal planes shown in Figure 3.4 would be analogous to where N=2 in Figure 3.1 (i.e. that of a double slit). In a real crystal N is normally very large and the atoms could of course be replaced by any basis. In fact, there are also an infinite number of such sets of planes one could choose, where the reflected wave from one layer would interfere with the reflected wave from the next layer down, and so on. To distinguish between such planes in crystals it is standard to use Miller notation. The Miller index *(hkl)* describes where the plane would intercept the unit cell's lattice vectors. Each lattice point is given by equation 3.10, where the $\mathbf{a_i}$'s are basis vectors and the n_i's arbitrary integers, then *(hkl)* would describe a plane that intercepts at $\mathbf{a_1}$/h, $\mathbf{a_2}$/k and $\mathbf{a_3}$/l, by convention this is then multiplied by a suitable integer to yield whole number indices with no common factors.

$$\boldsymbol{R} = \boldsymbol{n_1 a_1} + \boldsymbol{n_2 a_2} + \boldsymbol{n_3 a_3} \tag{3.10}$$

These different sets of planes, which lead to the interference of reflected waves, must themselves form a lattice, where each point is given by equation 3.11, with basis vectors $\mathbf{b_1}$, $\mathbf{b_2}$ and $\mathbf{b_3}$. This is known as the reciprocal lattice; each lattice point corresponds to a particular set of lattice planes (that can undergo Bragg diffraction).

$$\boldsymbol{G} = \boldsymbol{hb_1} + \boldsymbol{kb_2} + \boldsymbol{lb_3} \tag{3.11}$$

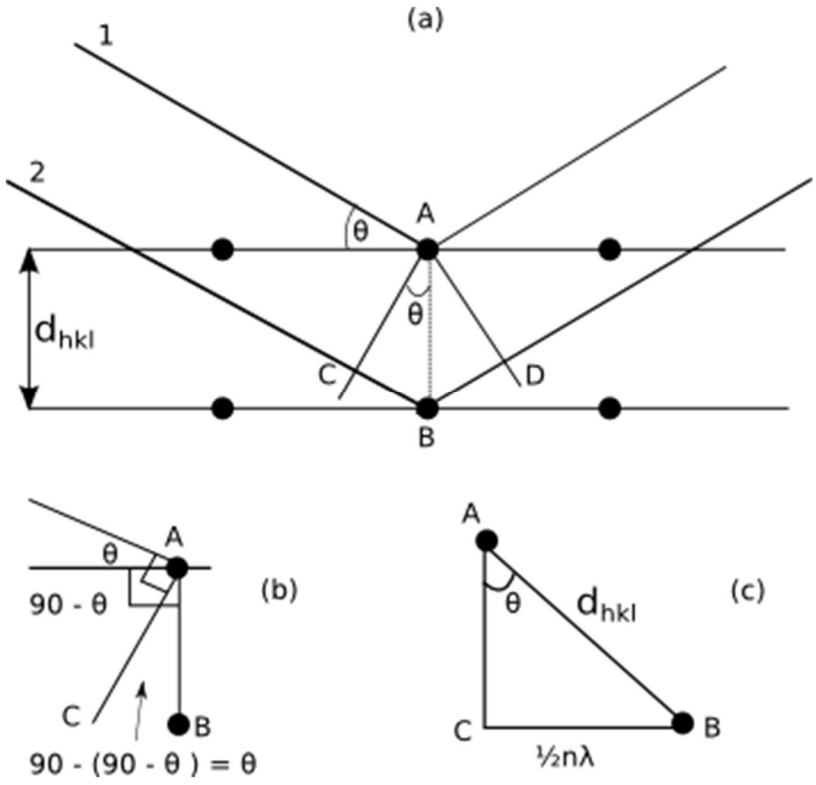

Figure 3.4: Geometrical constructions demonstrating Bragg's law by considering the scattering from crystal planes.

(a) Ray 1 reflects from atom A and ray 2 from atom B on the next plane, both rays are from the same source and therefore parallel. The lines AC and AD are at right angles to incoming and outgoing waves respectively. The path difference is given by CB + DB. Using the fact that the angle CAB is (see (b)) and then forming the right triangle ACBA (shown in c) the path difference can be given as $2d_{hkl}\sin(\theta)$. For constructive interference this should be an integer multiple of the wavelength.

Using the path difference from equation 3.9 and the definition of momentum transfer in Figure 3.3 the phase difference γ used for optical diffraction (eq. 3.4) above can be rewritten for the Bragg diffraction as equation 3.12.

$$\boldsymbol{\gamma = \frac{\delta}{2} = \frac{\pi\, 2d \sin\theta}{\lambda} = \frac{qd}{2}} \tag{3.12}$$

It is then straightforward to substitute equation 3.12 into equation 3.3 and arrive at the N-slit interference function for a 1-dimensional crystal undergoing Bragg diffraction. Extending this to a 3-dimensional crystal yields equation 3.13 where a pre-factor to account for Thompson scattering (equation 3.8) has also been included.

$$\boldsymbol{I(q) = (A_i \frac{r_0}{R_0})^2 |f(q)|^2 \frac{sin^2(½N_1 q a_1)}{sin^2(½q a_1)} \frac{sin^2(½N_2 q a_2)}{sin^2(½q a_2)} \frac{sin^2(½N_3 q a_3)}{sin^2(½q a_3)}} \tag{3.13}$$

Just as in the optical case, this function has maxima when γ is an integer multiple of π, that is, $½qa_i = \pi n_i$. The integers n_i where this condition is met must be equivalent to the Miller indices, i.e. planes that reflect X-rays. This leads to what are known as the Laue conditions of diffraction:

$$\begin{aligned} \boldsymbol{a_1 . q} &= \boldsymbol{2\pi h} \\ \boldsymbol{a_2 . q} &= \boldsymbol{2\pi k} \\ \boldsymbol{a_3 . q} &= \boldsymbol{2\pi l} \end{aligned} \tag{3.14}$$

The general solution to the above set of equations is a vector **q**, (i.e. G from equation 3.11), with basis vectors:

$$\begin{aligned} \boldsymbol{b_1} &= \boldsymbol{2\pi \frac{a_2 \times a_3}{a_1 \cdot (a_2 \times a_3)}} \\ \boldsymbol{b_2} &= \boldsymbol{2\pi \frac{a_3 \times a_1}{a_2 \cdot (a_3 \times a_1)}} \end{aligned} \tag{3.15}$$

$$\boldsymbol{b_3 = 2\pi \frac{a_1 \times a_2}{a_3 \cdot (a_1 \times a_2)}}$$

The Laue conditions are all met at principle maxima called Bragg peaks. The scattered intensity at such maxima is then given by:

$$\boldsymbol{I(q) = (A_i \frac{r_0}{R_0})^2 |f(q)|^2 N_1^2 N_2^2 N_3^2} \quad (3.16)$$

In the earlier discussion on optical diffraction the factor $|f|^2$ was conveniently left untreated and merely described as the Fourier transform of a single slit. The same is true for atoms. The Fourier transform of the electron density of a single atom is given by equation 3.17 and known as the atomic form factor which is derived by summing the scattering of all electrons around the atom.

$$\boldsymbol{f(q) = \int_{-\infty}^{+\infty} \rho(r) e^{(iq \cdot R)} d^3 r} \quad (3.17)$$

The atom is assumed to be spherically symmetrical and therefore the form factor only depends on the magnitude of q and not its direction. The atomic form factors for most elements are tabulated in the International Tables of Crystallography [35] which list appropriate coefficients for the Cromer-Mann equation. The Cromer-Mann equation (3.18) provides a good analytical approximation of the q dependence of atomic form factors, where q is less than ~20 $Å^{-1}$.

$$\boldsymbol{f(q) = \sum_{i=1}^{4} a_i e^{-b_i (q/4\pi)^2} + c} \quad (3.18)$$

In practice the form factor needs to account for the resonant effect of photon energies close to adsorption edges, anomalous dispersion. The dispersion corrected form factor is

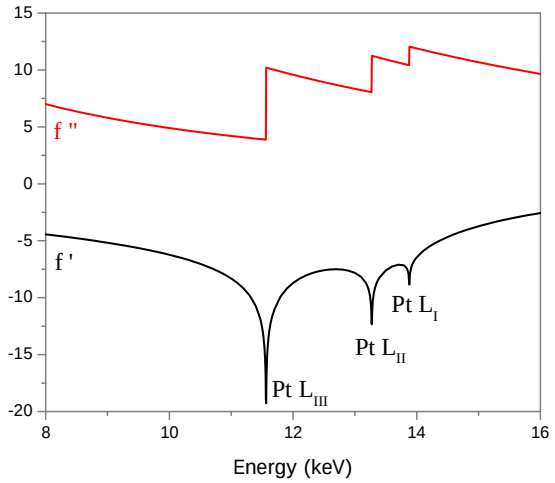

Figure 3.5. Graph showing the variation of the f' and f'' terms of the atomic scattering factor for Pt with incident X-ray energy. Discontinuities can be see where the L-edges are indicated. Data from [36].

given in equation 3.19 and includes an extra complex term account for any shift in phase that occurs.

$$\boldsymbol{f(q, E) = f(q) + f'(E) + if''(E)} \tag{3.19}$$

Tabulations by Brennan and Cowan [36] show the energy dependence of the f' and f'' terms for most atoms which can be easily interpolated to find their values. The dependence of f' and f'' over a typical energy range (8 keV – 16 keV) are plotted in Figure 3.5 for Pt, where the L-edges are indicated.

When the repeated basis (or unit cell) contains more than one atom (possibly of different types) the contributions from each atom must be summed. Such a summation is presented below, and known as the structure factor and will be direction dependent.

$$F(q) = \int_{-\infty}^{+\infty} \rho(r) e^{iq \cdot R)} d^3 r = \sum_{j=1}^{N} f_j e^{(iq \cdot r_j)} \quad (3.20)$$

Where f_j is the form factor for each atom j and relative atomic position of the atom j in the unit cell is given by the vector $\mathbf{r_j}$. The structure factor is often given in component form as:

$$F_{hkl} = \sum_{j=1}^{N} f_j e^{2\pi i(hx_j + ky_j + lz_j)} \quad (3.21)$$

An additional factor inside the summation is also needed to account for the thermal vibration and static disorder of then atoms, the so-called Debye-Waller factor:

$$f_{dwf} = e^{-\frac{1}{2}(q<u>)^2} \quad (3.22)$$

Where <u> is a space average of the atomic displacements across the entire crystal, in the simplest case it is assumed isotropic and therefore just a scalar. The effect of the Debye-Waller factor is more pronounced with larger momentum transfer.

3.3 Surface Diffraction

If one of the Laue conditions are not met, say for example along the L direction then the N-slit interference function associated with that condition can be evaluated by assuming there is a semi-infinite number of layers[32]:

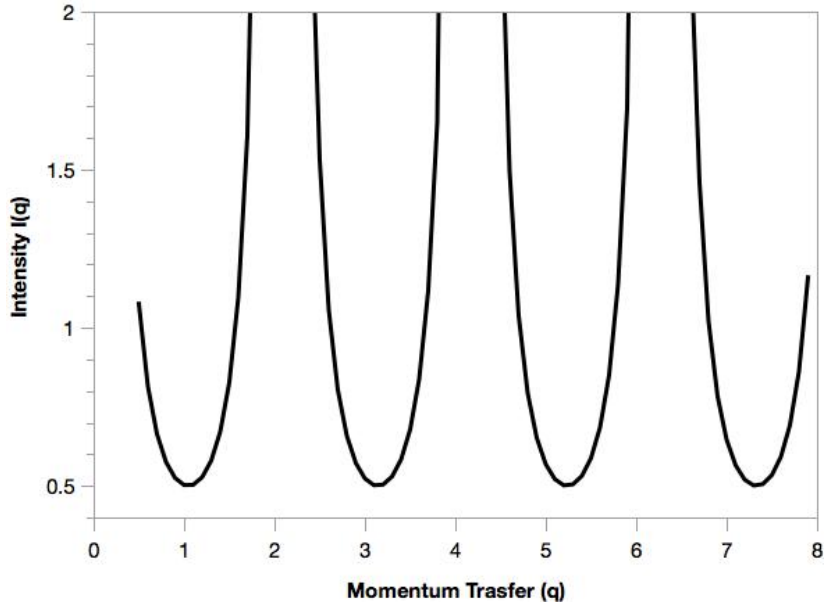

Figure 3.6. Plot of equation 3.23 showing the variation of intensity as one of the diffraction conditions is relaxed for a semi-infinite crystal. **Note:** In practice the Bragg condition can't be kept if all components of **q** are varied, therefore the x-axis is normally given in units of q_z, or, equivalently, L the reciprocal lattice coordinate in that direction.

$$I(q) = \lim_{N_3 \to \infty} (A_i \frac{r_0}{R_0})^2 |F(q)|^2 N_1^2 N_2^2 \frac{\sin^2(\frac{1}{2} N_3 q a_3)}{\sin^2(\frac{1}{2} q a_3)}$$

$$= (\mathbf{A_i} \frac{\mathbf{r_0}}{\mathbf{R_0}})^2 |\mathbf{F(q)}|^2 \mathbf{N_1^2 N_2^2} \frac{\mathbf{1}}{\mathbf{2 \sin^2(\frac{1}{2} q a_3)}} \ \mathbf{(for\ q a_3 \neq 2\pi l)} \qquad (3.23)$$

This leads to streaks of intensity between the Bragg peaks called crystal truncation rods (CTRs), such as in Figure 3.6. In theory the same argument can be applied to the other two directions. However, these streaks of intensity are known as CTRs because they are only seen where there is a sharp interface, such as a surface. There is not a sharp interface at the edges of the beam or where the beam is attenuated by the sample. In these cases, the Fourier transform decays much faster than the CTR in reciprocal space, causing the scattering to retract close to the Bragg peaks. The Fourier transform of a step function,

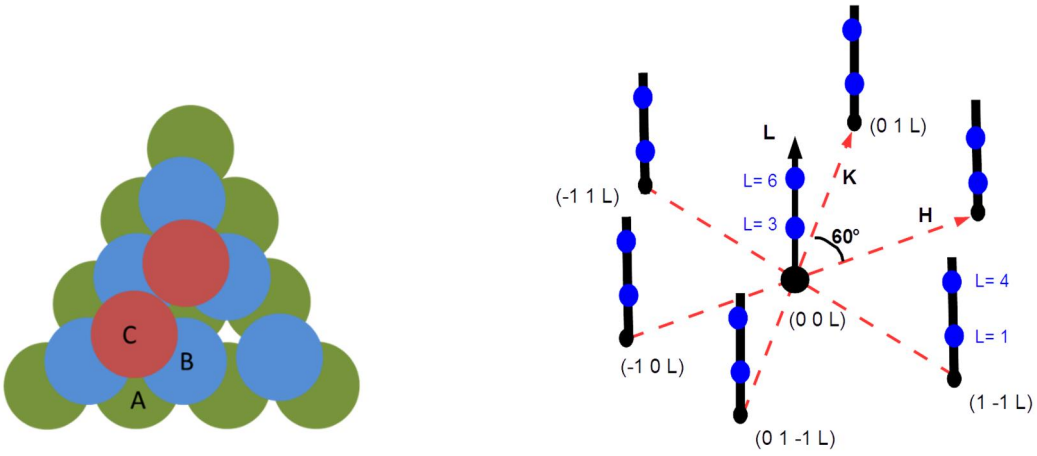

(B) Real space (A) Reciprocal space

Figure 3.7. Real and reciprocal space structure for the (111) face of face-centred cubic crystal. (A) shows the ABC stacking arrangment of the stoms whereas (B) shows the arrangment of the reciprocal lattice points that meet the diffraction condition and the truncation rods through them.

such as the surface, decays at a much slower rate. If the surface itself is rough this will also result in the intensity falling off more sharply. Unfortunately, this kinematical approximation is not valid at or close to the Bragg peaks as it predicts an infinite intensity. A full dynamical theory is needed to describe the intensity close to Bragg peaks.

The effect of adsorption should also be included, although practically it has only a small impact upon a CTR. This can be done by summing up the amplitudes from a semi-infinite number of layers undergoing scattering (eq. 3.1), but with adsorption, ε, from one layer to the next.

$$\boldsymbol{A_{total}} = \sum_{j=-\infty}^{0} \boldsymbol{f \cdot f_{dwf} \cdot e^{-(iq_3 \cdot a_3 - \epsilon)j}} = \frac{\boldsymbol{f \cdot f_{dwf}}}{\boldsymbol{1 - e^{(-iq_3 \cdot a_3 + \epsilon)}}} \qquad (3.24)$$

Where the top layer is at z = 0. The pre-factors from the Thompson formula and the contributions from the other directions (i.e. $N_1^2 N_2^2$) are constant and have been left out for simplicity. In the limit as ε becomes infinitesimal we retrieve equation 3.23 since equation 3.24 would then be equivalent to equation 3.1. For the rest of this discussion adsorption from the crystal is ignored.

The work presented in this thesis was performed on face-centred cubic crystals, prepared such that the surface was terminated at a (1 1 1) face. Before continuing, the CTR for such a surface is derived. Figure 3.1.7 (a) shows how the atoms are arranged for this face. It's standard practice in surface X-ray diffraction to transform the Miller indices such that L is perpendicular to the surface and H and K are in the plane (where possible). Equations 3.25 show the relationship between the [1 1 1] surface reciprocal space coordinates and the more standard conventional unit cell coordinates.

$$\begin{aligned} \boldsymbol{h_{bulk}} &= \frac{\mathbf{2}}{\mathbf{3}}\boldsymbol{h_s} - \frac{\mathbf{2}}{\mathbf{3}}\boldsymbol{k_s} + \frac{\mathbf{1}}{\mathbf{3}}\boldsymbol{l_s} \\ \boldsymbol{k_{bulk}} &= \frac{\mathbf{2}}{\mathbf{3}}\boldsymbol{h_s} + \frac{\mathbf{4}}{\mathbf{3}}\boldsymbol{k_s} + \frac{\mathbf{1}}{\mathbf{3}}\boldsymbol{l_s} \\ \boldsymbol{l_{bulk}} &= -\frac{\mathbf{4}}{\mathbf{3}}\boldsymbol{h_s} - \frac{\mathbf{2}}{\mathbf{3}}\boldsymbol{k_s} + \frac{\mathbf{1}}{\mathbf{3}}\boldsymbol{l_s} \end{aligned} \qquad (3.25)$$

Figure 3.7 (b) shows a reciprocal space map for the (1 1 1) surface, where by definition the lattice points are the planes giving rise to Bragg diffraction. For the (1 1 1) face the layers are stacked in an ABC arrangement along the surface normal This means along this direction the unit cell repeats every three layers and therefore the reciprocal lattice points along this direction will be separated by 3. The units for h and k are $a^* = b^* = 4\pi/\sqrt{3}a_{NN}$ whereas for l it will be $c^* = 2\pi/\sqrt{6}a_{NN}$, a_{NN} is the nearest-neighbour distance. The (0 0 l) CTR has no in-plane components of momentum transfer and is known as the specular CTR. The CTRs from the (1 1 1) termination of the bulk crystal

can computed in a manner similar equation to 3.24, where a semi-infinite number of layers extending from z= 0 to z= -∞ is assumed. This time one must however account for the three layers in the stacking sequence. If (0, 0 ,0), (-1//3, 1/3, 1/3), (-2/3,2/3,2/3) are the coordinates for atoms in the first three layers then multiplication of the first non-zero coordinate by an integer will give coordinates for atoms successively further into the bulk. When the atoms are of the same type this is easily done using the component form of the structure factor, where the summation is again that of a geometric series:

$$\boldsymbol{F_{Bulk}} = \sum_{j=0}^{-\infty} \boldsymbol{f \cdot f_{dwf}}\, \boldsymbol{e^{2\pi i(-\frac{1}{3}h+\frac{1}{3}k+\frac{1}{3}l)j}} = \frac{\boldsymbol{f \cdot f_{dwf}}}{\boldsymbol{1 - e^{2\pi i(\frac{h}{3}-\frac{k}{3}-\frac{l}{3})}}} \qquad (3.26)$$

It is often the case that close to the surface of a crystal the arrangement of atoms is somewhat distorted. Typically, this is either through relaxation, reconstruction, or an increase in disorder. Relaxation involves the distance between layers at the surface either expanding or contracting away from the layer below. Reconstruction involves a change in periodicity so that surface layers are no longer in registry with the bulk. An increased disorder can be the result of missing atoms, bucking of surface atoms or an increase in the vibrational displacement of surface atoms. In order to calculate the impact of these, on the form of the CTR, the structure factor is calculated separately. The structure factor for the top 3 surface layers of a (1 1 1) FCC crystal is then given by:

$$\boldsymbol{F_{surf}} = \sum_{j=1}^{j=3} \boldsymbol{f \cdot f_{dwf(j)} \theta_j e^{2\pi i\left(-\frac{1}{3}h+\frac{1}{3}k+[\frac{1}{3}+\epsilon_j]l\right)j}} \qquad (3.27)$$

This is just a continuation of eq. 3.26 above z=0. Where θ_j is the coverage of the j^{th} layer, ε_j is an offset from the bulk z position to account for expansion, and $f_{dwf(j)}$ is the surface Debye-Waller factor of each layer. The surface Debye-Waller factor is typically modelled

as the bulk Debye-Waller multiplied by an additional out of plane component along the surface normal, i.e.

$$f_{dwf(j)} = e^{-\frac{1}{2}(q<u>)^2} e^{-\frac{1}{2}(q_z u_j)^2} \tag{3.28}$$

If the surface is reconstructed it should be modelled separately, although for the specular rod this does not matter. A reconstructed layer is equivalent to a monolayer of atoms and where the in-plane Bragg condition is met there will be a rod of scattering spanning the out-of-plane direction – this may or may not be superimposed on top of a CTR depending on the periodicity. Figure 3.8 shows the (1 0 L) CTR for a (1 1 1) FCC crystal, indicated are the effects of coverage, relaxation and roughness of the topmost surface layer coverage of the topmost atomic layer and an increase in the roughness of this layer cause the intensity between the Bragg peaks to fall off more sharply whereas relaxation causes an asymmetry around the Bragg peaks. Roughness (modelled through the DWF) can be distinguished from a change in coverage since the intensity between all the Bragg peaks will be affected equally with coverage whereas the effect is more pronounced at higher q with roughness. At this stage the intensity along a CTR is given by:

$$I_{CTR} = |A_i \frac{r_0}{R_0} N_1^2 N_2^2 (F_{bulk} + F_{surf})|^2 \tag{3.29}$$

There are numerous schemes to modify this equation to account for more pronounced roughness, one of the simplest was proposed by Robinson [6] and assumes an exponential distribution of heights. Initially there is a fully occupied layer, then a layer occupied by a fraction β of sites, to one with β^2 sites occupied and so on. This modifies the intensity as in equation 3.30.

$$I = \frac{(1-\beta)^2}{1 + \beta^2 - 2\beta cos(q \cdot a_3)} |A_i \frac{r_0}{R_0} N_1^2 N_2^2 (F_{bulk} + F_{surf})|^2 \tag{3.30}$$

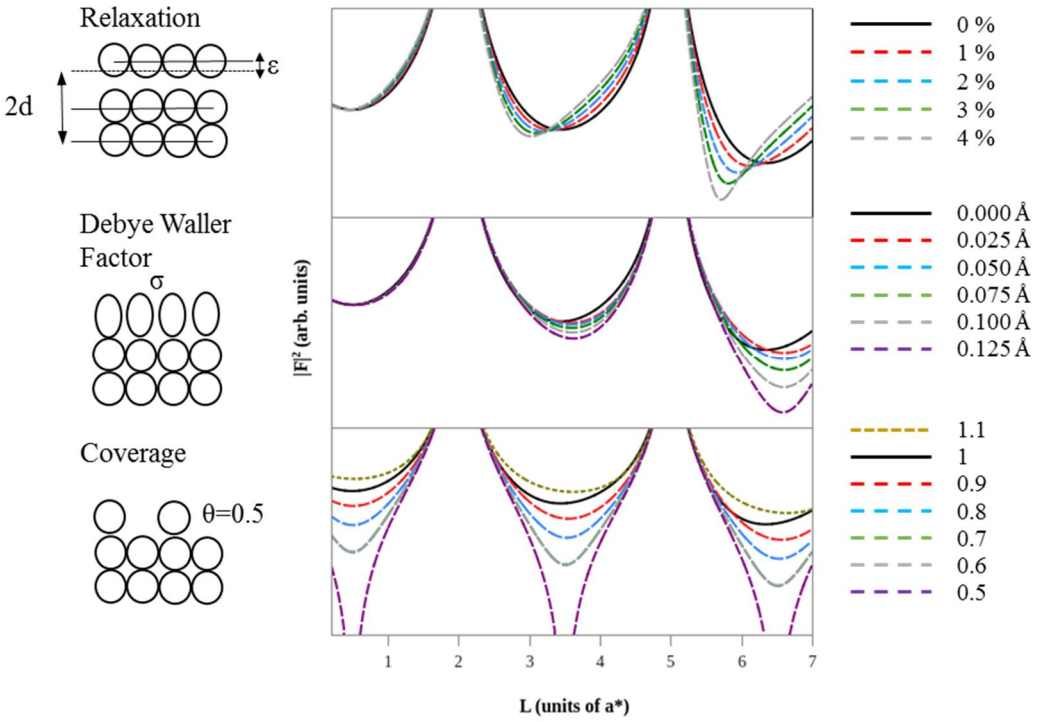

Figure 3.8. Demonstration of how various structural parameters for the crystal surface discussed in the text can modify the form of a CTR. The cartoons on the left hand side indicate what each of the effects physically mean. The various lines show what a (1 0 L) CTR for a Pt (111) crystal would look like if the value of the parameter depicted in the cartoon was changed to that shown in the legend. Relaxation is given in units of percentage expansion from the bulk lattice spacing, the Debye-Waller factor is in root-mean squared displacement in Å, and the coverage is fractional coverage.

The final thing to discuss is the contribution the scattering from an electrolyte has on the intensity profile of a CTR. If an electrolyte is completely randomly ordered, then the only contribution will be from absorption/random scattering of X-rays passing through the liquid. The experiments presented in later chapters were performed using a thin-layer arrangement, this is depicted in Figure 3.9 where there is a film of height h above the

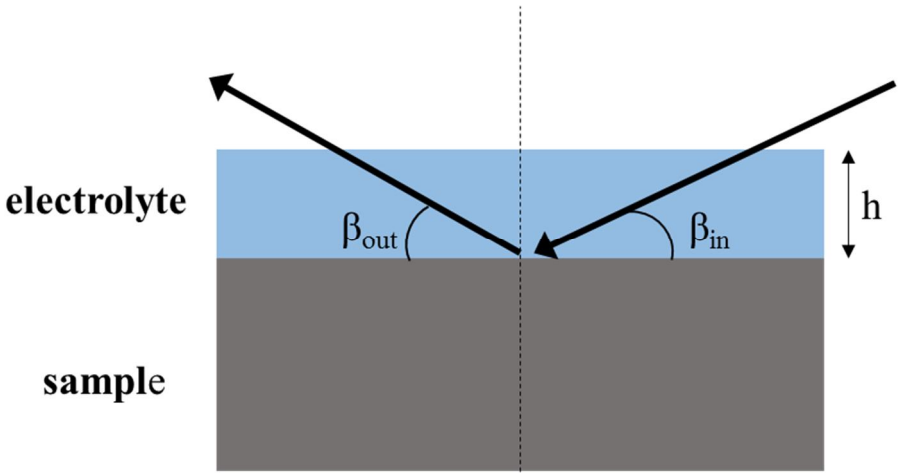

Figure 3.9. Transmission of X-rays through a thin film of thickness h the path length and consequently adsorption of the X-ray beam will depend on the incoming and outgoing angles, as well as the thickness of the electrolyte film

sample, and the path length travelled by the X-rays will depend on the incident angle β_{in}. Similarly, for the outgoing beam the path length will depend on an exit angle β_{out}, which depending on the scattering geometry this may equal β_{in}. If the linear adsorption coefficient of the film is μ then one can multiply the intensity by a factor T to account for adsorption:

$$T = e^{-\frac{\mu h}{sin(\beta_{in})}} e^{-\frac{\mu h}{sin(\beta_{out})}} = t^{\frac{1}{sin(\beta_{in})}+\frac{1}{sin(\beta_{out})}} \quad (3.31)$$

Where the height of the film and adsorption coefficient have been grouped in one transmission parameter, t, when t=1 there is no adsorption and when t=0 the beam is completely adsorbed.

On the other hand, any ordering in the electrolyte can modify the form of the CTRs and needs to be explicitly included in the structure factor. Only when electrolyte species are strongly adsorbed would one expect to see in plane ordering. More often the case (considered here) are planes of concentrated electron density parallel to the crystal

surface. In electrochemical systems such vertical ordering is expected (see discussion in Chapter 2 on double layers) but some ordering might indeed be expected where any smooth hard wall meets a liquid [37–39]. A structure that is only ordered perpendicular to the surface plane will only affect the specular CTR (00L) as this has no in-plane momentum transfer. Measurement of the specular CTR is also known as extended reflectively and is direct probe of electron density along the surface normal. To account for this, an additional structure factor needs to be added to equation 3.30.

The simplest case is a single atomic layer above the surface at height H_{ad}, this is called an adlayer and has a structure factor given in equation 3.32.

$$\boldsymbol{F_{adlayer} = \theta_{ad} f_{adlayer} e^{-\frac{1}{2}<qu_{ad}>^2} e^{2\pi i(H_{ad} l)}} \qquad (3.32)$$

Where θ_{ad} is the fractional coverage of the layer to the metal surface, $f_{adlayer}$ the scattering factor for the atoms in the layer, the $\boldsymbol{e^{-\frac{1}{2}<qu_{ad}>^2}}$ term accounts for disorder and $\boldsymbol{e^{2\pi i(H_{ad} l)}}$ is the structure factor where the k=0 and l=0, since this is for the specular CTR only. The height is also in terms of the bulk unit cell. Figure 3.10 (a) shows how various coverages of a layer of carbon atoms at 3 Å from a Pt surface affect the specular CTR. It is apparent that, despite the considerable difference in Pt and C scattering cross sections, even adlayers with small coverages can have a significant impact on the CTR. Figure 3.10 also shows how the CTR is sensitive to the distance of such layers from the crystal. A change in layer height affects the specular CTR differently to roughness and coverage because it affects the path difference of the interfering waves. Over a certain range the function will vary as expected but then it will dramatically change, this can be an advantage in deciding between different models.

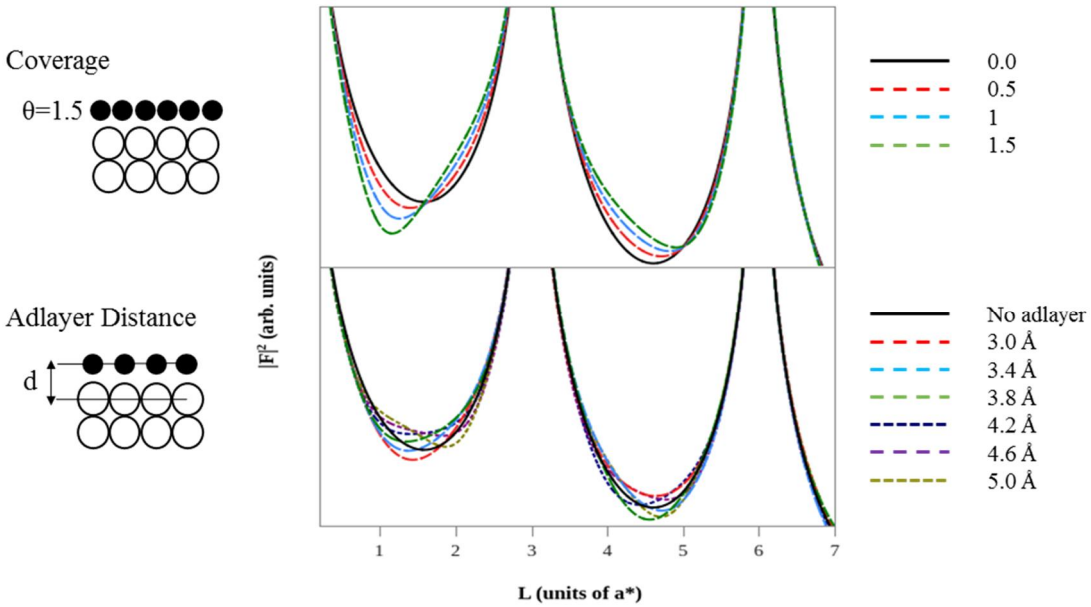

Fig 3.10. Demonstration on how various structural parameters for an adsorbed layer of adatoms can modify the form of a specular CTR. The cartoon on the left hand side illustrates the physical meaning of the parameters varied. The various coloured lines show how the form a CTR from the perfect the termination of a bulk Pt (111) crystal is modified by changes in an adlayer. The adlayer has coverage θ=1, distance 3.0 Å and rms roughness 0.2 Å unless indicated otherwise.

The discontinuity where the electron density in the electrolyte transitions towards the bulk electrolyte density will also affect the specular CTR. In Figure 3.12, two ways of modelling liquid structure at an interface are illustrated as vertical electron density plots. The most basic model shown in blue is that of an error function, a smooth varying function that plateaus at the bulk liquid density. The structure factor of this function is:

$$\boldsymbol{F = if(A_{uc}\rho)\frac{e^{-\frac{1}{2}(Q\sigma_0)^2}}{Q}e^{2\pi i(lH)}} \tag{3.33}$$

Where f is the scattering factor of the liquid, ρ (= 0.033 Å for water) is the density of bulk liquid, σ_o is the width of the error function and H is the height above the surface (in unit cell coordinates).

A more advanced approach is to assume that the liquid has layers of electron density that are successively broadened away from the surface, where the width of the j^{th} layer is:

$$\boldsymbol{\sigma_j = \sqrt{\sigma_0^2 + j\sigma_{bar}^2}} \tag{3.34}$$

The structure factor is then:

$$\boldsymbol{F = df(A_{uc}\rho)\left(\frac{e^{-\frac{1}{2}(Q\sigma_0)^2}}{1 - e^{-\frac{1}{2}(Q\sigma_{bar})^2}e^{iQd}}\right)e^{2\pi i(lH)}} \tag{3.35}$$

In this equation d is the spacing between successive layers, σ_{bar} the broadening term from equation 3.34 and the rest is as for the error function in equation 3.33. In the limit as σ_{bar} tends to 0 the structure factor of an error function is recovered.

Figure 3.13 (a) shows how the form of a CTR is affected by these liquid components and Figure 3.13 (b) shows the contribution each model makes to the structure factor. The error function alters the CTR at low q but then falls off quickly, whereas the layered liquid model has a quasi-Bragg peak due to the layering. The layered model has been found to work well for water at charged mineral interfaces [40] but it may not be appropriate for electrochemical interfaces with adsorbed species or a significant diffuse region. Detailed discussion of these two models and their relative merits can be found in ref [41]. This chapter is concluded with the final equation for the intensity of a CTR which is summarised as equation 3.36.

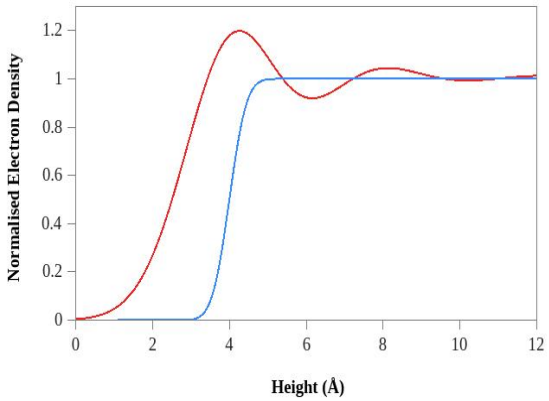

Figure 3.12. Graph showing the difference between a liquid above a surface modelled with an error function (blue), and a liquid modelled with layers that broaden the further away from the surface one gets. The metal surface is not shown, but located at a height of 0. The Error function has width σ_o= 0.5 Å and is situated H = 4 Å from the surface. The layer model has parameters σ_o = 0.7 Å, σ_{bar} = 0.5 Å , d = 3.2 Å, and H = 4 Å.

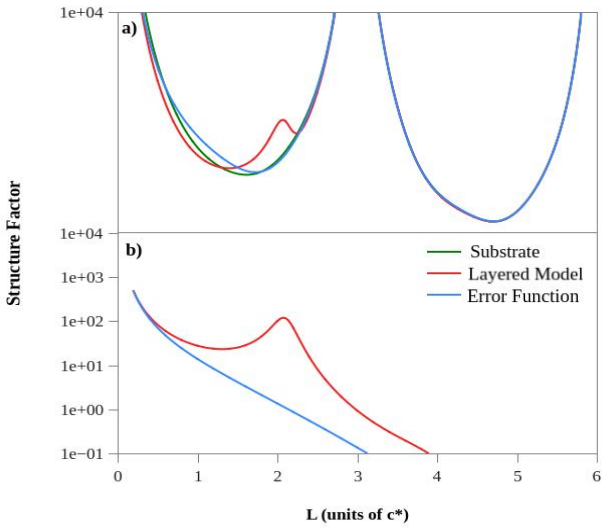

Figure 3.13. Comparison of the effect a layered liquid model and an error function has on the structure factor for the model given in Figure 3.12. a) Calculated specular CTR for an ideal termination of a Pt (111) surface (green line) compared to the CTR including the layered model discussed in the text (red line) and an error function (blue line). (b) The magnitude of the structure factor for the layered model or the error function that is added to the CTR.

$$\boldsymbol{I = TR(q)S|\,(F_{bulk} + F_{surf} + F_{ad} + F_{liquid})|^2} \tag{3.36}$$

Where the roughness factor has been recast as R(q), some of the constants have been folded into S and additional structure factors for adlayers and any liquid structure have been included. The complete expansion for a CTR for a (111) FCC crystal with three surface layers, one adlayer and an error function describing the liquid side of the interface is then finally:

$$\begin{aligned} \boldsymbol{I = t^{\frac{1}{sin(\beta_{in})}+\frac{1}{sin(\beta_{out})}} R(q) S} & \left| \frac{\boldsymbol{f_{bulk} \cdot e^{-\frac{1}{2}(q<u>)^2}}}{\boldsymbol{1 - e^{2\pi i(\frac{h}{3}-\frac{k}{3}-\frac{l}{3})}}} \right. \\ & \boldsymbol{+ \sum_{j=1}^{j=3} f_{surf} e^{-\frac{1}{2}(q<u>)^2} e^{-\frac{1}{2}(q_z u_j)^2} \theta_j e^{2\pi i\left(-\frac{1}{3}h+\frac{1}{3}k+\left[\frac{1}{3}+\epsilon_j\right]l\right)j}} \\ & \boldsymbol{+ \theta_{ad} f_{adlayer} e^{-\frac{1}{2}<qu_{ad}>^2} e^{2\pi i(H_{ad}l)}} \\ & \left. \boldsymbol{+ if_{liquid}(A_{uc}\rho)\frac{e^{-\frac{1}{2}(q\sigma_0)^2}}{q} e^{2\pi i(lH_{err})}} \right|^2 \end{aligned} \tag{3.37}$$

A python program that calculates this intensity is listed in appendix 1.

4 EXPERIMENTAL TECHNIQUES

Work at synchrotrons can be complex and fairly involved, add electrochemistry into the mix and one needs to be very careful about how experiments are designed and conducted. Post experiment, there are large quantities of data that need to be processed and analysed so that meaningful and hopefully interesting conclusions can be reached. This chapter will describe the procedure and experimental equipment necessary to make *in-situ* investigations of single crystal electrochemical interfaces using surface X-ray diffraction. There are essentially two parts, everything leading up, and including, the physical process of actually making the measurement and then how to process and analyse the data.

4.1 Sample Preparation

The central theme throughout this work is that small changes in a metal electrode can impact upon the electrochemical behaviour of a system. Therefore, it is vitally important that a reliable and reproducible procedure for sample preparation is used. The crystals were 3 mm high discs with a central grove for easy mounting, with a diameter of 10 mm. For this work single metal crystals that had been grown, oriented (to less than

0.2 ° accuracy) and polished were purchased (Matek/SPL). Initial preparation was done in an ultra-high vacuum (UHV) system.

Once in UHV, the single crystal samples were prepared by a series of 'sputter and anneal' cycles. The sputter cycles remove impurities from the sample's surface, and are done by Ar ion (Ar+) bombardment. Annealing is where the sample is heated (below the surface melting temperature) so that long range order in the surface layers can recover. The heating can be done either by passing a current through a filament that is in thermal contact with the sample or by using an e-beam heater for higher temperatures. An e-beam heater works by accelerating high energy electrons into a grounded sample, heating it through electron bombardment. Between the 'sputter and anneal' cycles the quality of the surface was assessed with both low energy electron diffraction (LEED) and X-ray photoemission spectroscopy (XPS). LEED is a surface sensitive diffraction technique that works by firing a beam of electrons at the surface and collecting the scattered electrons on a photo-fluorescent screen. The screen will show a diffraction pattern caused by the interference of electrons. The surface sensitivity is a result of the strongly interacting nature of the electrons which do not penetrate far into the sample. Sharp spots on a LEED pattern indicate a well ordered surface. Surfaces such as Au (111), reconstruct and if there are sharp satellite spots due to the reconstruction then this is good sign of a well ordered surface. XPS works by measuring the kinetic energy of electrons that are ejected from a sample when it is irradiated by an X-ray beam. The kinetic energy of the electrons (E_k) can be converted to binding energy (E_b) through the relationship

$$\boldsymbol{E_b = E_p - (E_k + \phi)} \qquad (4.1)$$

Where E_p is the photon energy (which is known in advance) and φ is the work function of the electron analyser. In a plot of binding energy against the number of counts there

will be several peaks. These will correspond to the atomic (or molecular) energy levels of the sample being investigated. In the preparation of samples for electrochemistry XPS can be used to check that the sample is what it's supposed to be and that there are no surface contaminants.

It is somewhat impractical to 'UHV prepare' a sample before every measurement is made. Instead there are other techniques that are known to give a reproducible surface [42]. The choice of technique inherently depends on the particular sample. In the work described in the following chapters the principle techniques were 'flame annealing' and induction heating. For gold, flame annealing with a butane torch is known to produce large flat terraces and a reconstruction that survives transfer into an electrochemical cell [43]. The procedure is to heat up the gold crystal to a bright red surface but not so much as to cause any melting, this is avoided by constantly moving the flame on and off the sample. The sample should then be allowed to cool in an inert atmosphere (typically nitrogen or argon) and then covered by a drop of ultra-pure water. Quenching the sample by putting the water on too soon is known to lead to a poor surface, and the thermal shock will gradually damage the bulk of the crystal. In the electrochemical environment the adsorption of anions is thought to induce lifting of the reconstruction, therefore the emersion potential should be negative (the exact potential depends on the electrolyte). Inductive heating (or RF annealing) heats the sample through induction by generating a high-frequency magnetic field that produces eddy currents, the resistance to these currents causes the sample to heat. Typically, the sample is in a sealed reductive atmosphere such as Ar/H_2 (5% H2).

4.2 Electrochemistry

The standard three electrode cell has already been described in Chapter 2, however in order make *in-situ* X-ray measurements the design needs to be significantly modified. Figure 4.1 shows a schematic of what is known as the X-ray thin-layer cell which is similar that described in references [44,45]. The cell is constructed out of Kel-F due to its inertness and machinability, the fittings are made out of similar inert materials such as Teflon or PEEK. The counter electrode is normally a polycrystalline wire, made out of the same material as the working electrode. The choice of reference electrode depends on the stability of a particular reference in the system being investigated, but for most aqueous systems Ag/AgCl reference electrodes (Fisher Scientific, 66-EE009 "No leak" Ag/AgCl Reference electrode cat #: 13463578) seem to function well. A single crystal working electrode sits in a collet that tightens around the crystal as it is screwed down. Contact to the working electrode is made with a polycrystalline wire that is coiled up in a spring and passed through the base of the collet. In and out electrolyte tubing allows the electrolyte to be added/removed from the cell, this is controlled by opening taps to either an electrolyte reservoir (in) or a syringe (out). Above the working electrode sits a polypropylene film that is transparent to X-rays and secured with an o-ring (preferably made from some inert material). The film can be inflated/deflated by controlling the amount of electrolyte in the cell. An outer Kapton hood then surrounds the whole cell and has an overpressure of inert gas such as Nitrogen or Argon.

Initially the cell, fittings, glassware, and tubing are all soaked overnight in a 50:50 mixture of concentrated H_2SO_4 and HNO_3, following this they are rinsed several times in ultrapure water (Milli-Q), with a resistivity of around 18.2 MΩ·cm that has undergone several filtering and deionizing steps. The parts are then boiled in ultrapure water and again rinsed several times. Any polycrystalline wires are cleaned and

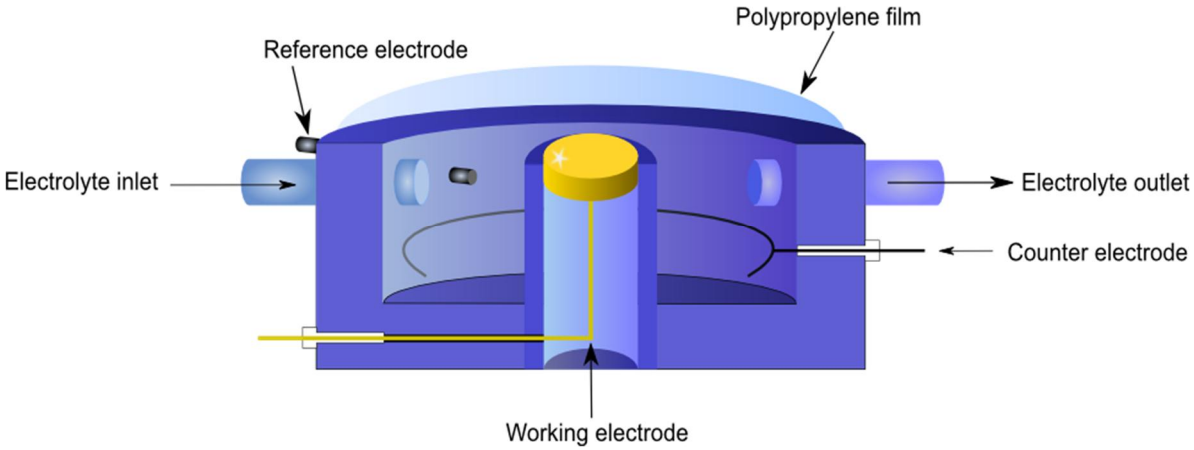

Figure 4.1. (a) Illustration showing the thin-layer *in situ* electrochemical cell, a 'kapton hood' is also place around the cell.

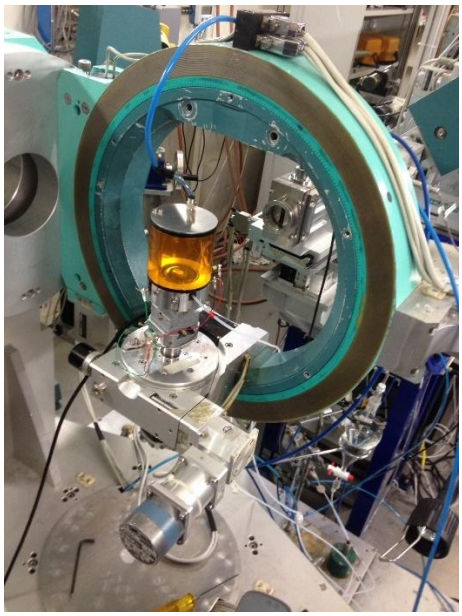

Figure 4.1 (b) Photograph of the thin-layer cell (depicted in Figure 4.1 (a)) on a diffractometer, also shown is the Kapton hood that sits around the cell to control the atmosphere around the electrochemical cell.

(depending on the material) dipped in acid and rinsed in ultrapure water, after which they are flame annealed and again rinsed in ultrapure water. The polypropylene film is rinsed several times in ultrapure water, then boiled, and again rinsed. The working electrode is prepared as in the previous section and then covered with a drop of ultrapure water and transferred into the collet. Once the collet has been secured the cell is topped up with electrolyte and the polypropylene film secured. At this stage fresh deaerated electrolyte is pulled through the cell and any trapped air is also removed. The hood is then fastened and the whole ensemble taken to the beamline and placed on a diffractometer. Voltammetry should be done with the film inflated to reduce any effects of the thin-layer arrangement which can limit diffusion. For the X-ray measurements the thin-film should be deflated (the thickness is then around 10 μm) to reduce adsorption of the X-ray beam.

4.3 Synchrotrons and Beamlines

The scattering along a crystal truncation rod is ~10^5 times less than that from Bragg peaks. Coupled with the need to penetrate a liquid layer (and to a lesser extent the polypropylene film) an extremely high photon flux is required. Laboratory based rotating anode sources are improving, but fluxes high enough for *in-situ* SXRD experiments are still not widely available. Instead a much better source of X-rays is a synchrotron, synchrotrons also have the advantage of having a tuneable energy output.

The acceleration of relativistic charged particles on a curved path through a magnetic field causes the emission of synchrotron radiation. Initially the use of synchrotron radiation began as a parasitic one; scientists realised that what the particle physicists viewed as ‘wasteful energy’ could be put to good use[46]. These were known as the 1st generation synchrotrons. X-rays from synchrotron radiation proved so useful that 2nd generation dedicated facilities were constructed. The major advance in these

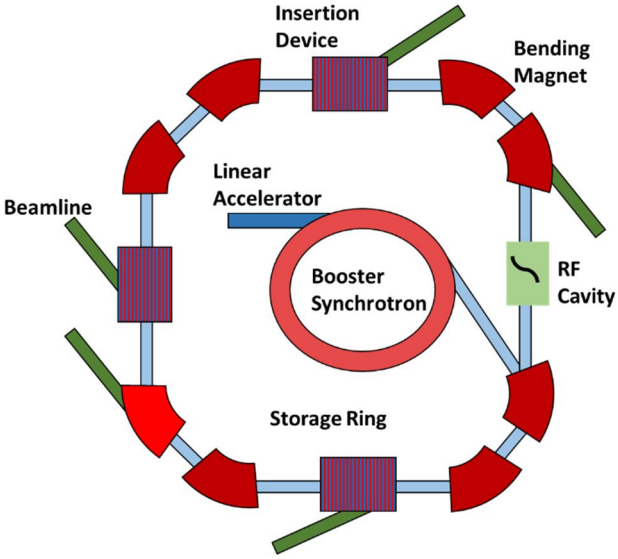

Figure 4.2. Simplified schematic of a 3rd Generation Synchrotron Red curved sections represent bending magnets, and straight striped sections represent an insertion device. The outer ring is known as the storage ring.

facilities was the introduction of an electron storage ring. Previously the synchrotron beams were subject to constant current changes due to the injection and acceleration of electrons, a storage ring allowed this to be smoothed and be stable over a period of many hours. 3rd generation synchrotrons were the next step, by including long straight sections in the storage ring a low emittance, better coherence and greater brightness could be achieved. Figure 4.2 shows the arrangement of a typical 3rd generation light source. An electron beam is initially produced in much the same way as a television cathode ray tube, it is then accelerated in a linear accelerator (LINAC), after which it is passed around a booster synchrotron to reach the required energy. The electrons then enter the storage ring. The storage ring is made up of several straight sections and large electromagnets called bending magnets are used to curve the electron beam between straight sections. As the electron beam passes through the various components in

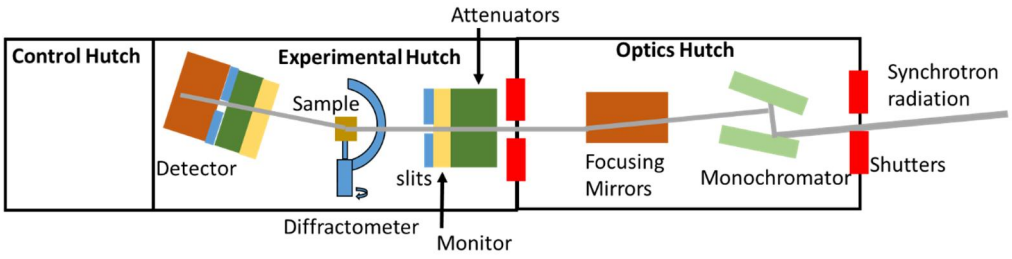

Figure 4.3. Illustration of a typical synchrotron beamline layout. There are 3 hutches, one which contains the user and computers to control operation (control hutch), an experimental hutch housing the sample and detector, and an optical hutch to prepare the X-ray beam. In the illustration the X-ray bean is shown in grey.

the storage ring it will lose energy, radio frequency (RF) cavities boost the electrons to stop this becoming significant. Situated around the storage ring are several beamlines. These can either be at a bending magnet where synchrotron radiation is already produced, or adjacent to a straight section where a separate device is needed to cause the electron beam to move, and generate X-rays. Such a device is known as an insertion device, there are two main types: undulators and wigglers. A wiggler is a series of a magnets like a bending magnet that periodically deflect (wiggles) the electron beam and causes in emission of synchrotron radiation. The intensity from a wiggler is much higher than that from a bending magnet because the contribution of all the magnets add up. An undulator on the other hand has a periodic arrangement of magnets that cause the radiation generated to add up constructively, providing a further enhancement in brightness. The generated fan of synchrotron X-rays then enters a ‘beamline’, the layout of a typical diffraction beamline is shown in Figure 4.3. Generally, there are three ‘hutches’: an optics hutch, an experimental hutch, and a control hutch (from where the beamline is operated). The synchrotron radiation is first monochromatised by a pair of monochromating crystals

(typically silicon) after which it is focused by focusing lenses and mirrors. The now focused and monochromatic beam enters the experimental hutch. Usually a series of attenuators are used to reduce the intensity of the beam to avoid damage to the sample and detector. It is then standard for some form of beam monitor such as an ion chamber to monitor the intensity of the beam, which can be used to normalise the data later on. Adjustable slits are then used to define the beam before it reaches the sample. For diffraction the sample will sit on a diffractometer allowing its movement in the beam. After the diffracted beam leaves the sample it is then measured by a detector, there may also be further attenuators, monitors, and slits on the detector arm. Detectors can either be point detectors such as a scintillation/photomultiplier tube combination or 2D arrays such as charged couple devices (CCD). Single-count solid state 2D detectors like the PILATUS range (developed at the Swiss Light Source) are also becoming increasingly popular.

4.4 Diffractometers

There are many types of diffractometers available for surface diffraction. Some common diffractometers are: 4-circle[47], 2+2 circle[48], z-axis[49], 2+3 circle[50], and 6-circle[51]. Theoretically only three degrees of freedom are needed to orient a sample to meet the Bragg condition, however in practice extra degrees of freedom are needed to keep certain angles constant (such as the angle of incidence) or to access regions of reciprocal space that would be otherwise blocked by the experimental apparatus. The measurements presented in Chapter 5 were made on a 6-circle diffractometer running in 4-circle mode at the UK CRG beamline, XMaS, at the ESRF (France). The measurements

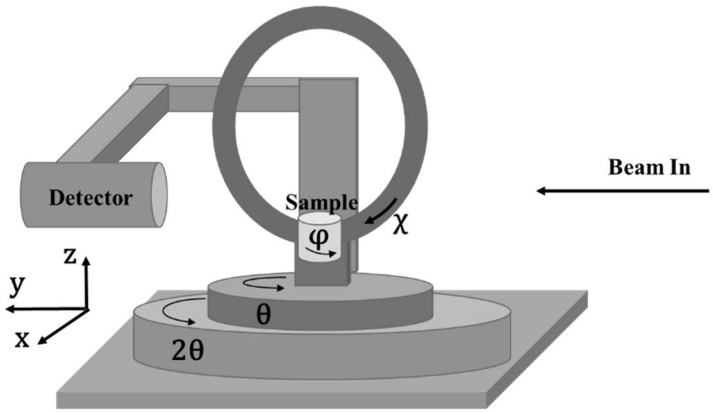

Figure 4.4 (a) Illustration of a 4 Circle diffractometer used to orient samples to meet various diffraction conditions. Laboratory frame of reference and sense of rotations are indicated. For a full description see reference [47].

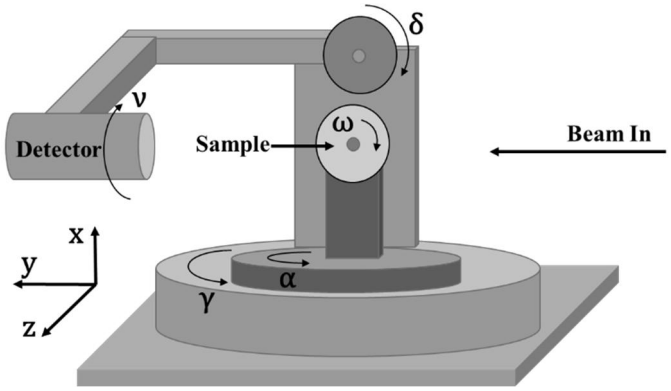

Figure 4.4 (b) Illustration of a 2+3 Circle diffractometer in vertical mode. Laboratory frame of reference and sense of rotations are indicated. A full description can be found if reference [50].

in Chapter 6 were made on a 2+3 circle diffractometer at the i07 beamline at the Diamond Light Source (UK). In Chapter 7 the results presented were also made on a 4-circle diffractometer at the Advance Photon Source and the Stanford Light Source (US). In Figure 4.4 (a) a schematic of a 4-circle diffractometer is shown with the various angles indicated. Similarly Figure 4.4 (b) illustrates a 2+3 circle diffractometer and its various angles. Today diffractometers are computer controlled, a user can merely enter a reciprocal space coordinate and the computer will convert this into the corresponding diffractometer angles for that sample and wavelength. This is calculated using an orientation matrix, known as the UB matrix, which for a four-circle diffractometer is described in ref. [47]. This orientation matrix gives the sample orientation with respect to the diffractometer angles (i.e. 2θ, θ, ψ, χ for 4-circle), it can then be used to calculate the angles required for a certain scattering vector Q. The U matrix, is a rotation matrix that rotates the sample's frame of reference (FOR) into the diffractometers FOR. B transforms a reciprocal space coordinate (h,k,l) into a real-space coordinate in the sample's FOR. In order to first calculate a UB matrix the diffractometer angles for two or more reciprocal space positions (normally Bragg peaks) are required. The procedure is now described for a four-circle diffractometer.

First one must ensure that the beam passes through the diffractometer's centre of rotation. This is done by placing a pin in the sample goniometer and focusing an optical telescope on the head of the pin. The φ and χ circles are each rotated 180 ° and the goniometer adjusted until the pin does not move (i.e. it is in the centre). Burn paper is then placed in the path of the beam, after which the diffractometer is translated so that the shadow of the pin is in the centre of the burn mark. Next it is a good idea to make sure the χ, 2θ, and θ motors are correctly zeroed (φ is arbitrary).

With all the angles at zero the sample can now be mounted on the goniometer. To ensure the sample is as flat as possible a laser beam is reflected from the sample onto the wall. The goniometer sample tilts are then adjusted so that the reflected laser beam does not move with rotation of the φ circle. The height of the sample is then adjusted by scanning the sample vertically across the X-ray beam and setting it to where the intensity is cut in half.

Next two Bragg peaks must be located so that a UB matrix can be calculated. Initially it can be useful to find a specular peak as there will be no φ dependence therefore θ and χ can be optimised without worrying about φ; this makes it easier to then go and find a non-specular position. Optimisation is an iterative procedure where the diffractometer is rotated while measuring the intensity, the diffractometer is moved to the maximum peak intensity and then the next angle rotated and optimised. This is repeated until an overall maximum (or compromise) is reached. After a specular position is located the computer software can give an improved calculation of where an off-specular Bragg positon can be found, for all rotations except φ. So initially the user must rotate the φ circle to locate the Bragg peak. After a Bragg peak has been found it can be optimised and entered into the computer for calculation of the UB matrix, this should be repeated for another reflection. One must also be careful when labelling Bragg peaks that the sense of rotation of φ is correct, i.e. does φ rotate in the correct direction from one reflection to another, or should the reflection be relabelled as a symmetry equivalent.

4.5 Scans and Data Extraction

In order to measure crystal truncation rods, or fractional order rods (due to reconstruction) several types of diffractometer scans are possible:

4.5.1 Rocking Scans

Initially the sample and detector are positioned at a reciprocal space position along a rod, i.e. the Bragg condition is met in two of the 3 directions. The detector is then fixed and the sample is rotated, repeating this along the rod enables measurement of a CTR profile through the integrated area. The width of a rocking scan is a convolution of the instrumental resolution and an intrinsic width of the crystal. The intrinsic width is the result of defects such as sample mosaicity and dislocations. If the sample has a significant mosaic spread the Bragg condition will be met for a range of angles resulting in a broader peak. The crystal should be rocked far enough to allow a good determination of the background signal. Figure 4.5 shows a rocking scan with a Lorentzian lineshape fitted to it (the correct lineshape needs to be selected for the data) with an additional straight line background. Every data point has an associated counting error (√n) which is combined with the counting error on the monitor. The area under the peak (integrated intensity) is directly proportional to the structure factor. There are a number of ways to calculate integrated area; typically, it is done by fitting a lineshape such a Lorentzian, as in Figure 4.5 (b), and analytically calculating the area. If a Lorentzian function is defined as:

$$\boldsymbol{L(x) = \frac{hw^2}{w^2 + 4(x-c)^2}} \qquad (4.2)$$

Where h is the height, w the full width half maximum (FWHM) and c the peak centre then the area under the peak will simply be ½πhw. The error on the integrated intensity can then be calculated with a proper propagation of errors, taking into account the confidence intervals or uncertainties of the fit parameters h,w, and c. Another approach is to numerically integrate the area under the peak (using a numerical procedure like the

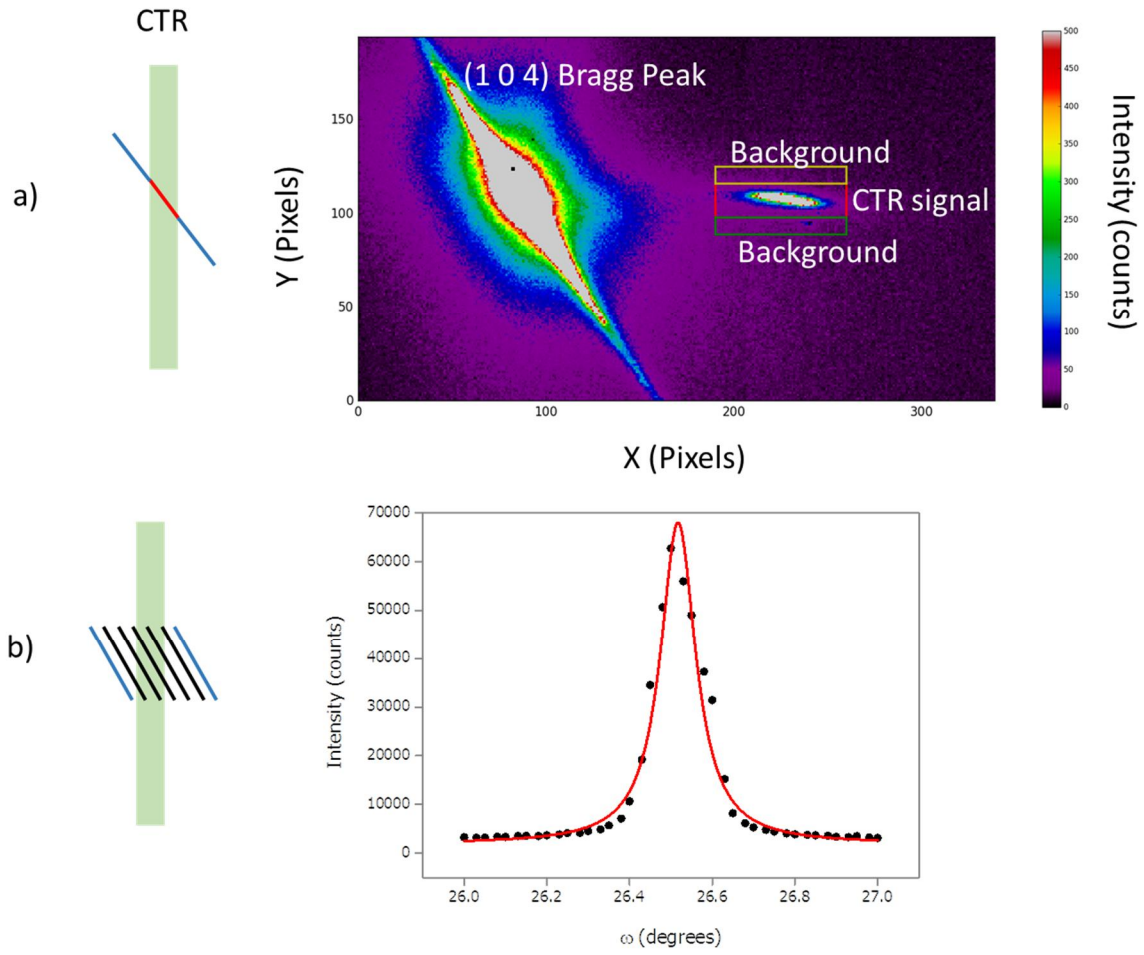

Figure 4.5. Illustration showing the difference between a 2D stationary scan and a rocking scan (see reference [52] for more information). Both measurements are made on the same system at (1 0 3.7), a position close to the (1 0 4) Bragg peak.

(a) 2D detector image measured through the (1 0 L) CTR. The structure factor is proportional to the sum of the intensity in the 'CTR signal' ROI minus the sum of the intensity in the two background regions. The (1 0 4) Bragg peak can also clearly been seen.

(b) Rocking scan for which the sample is rotated around an angle, ω, therefore scanning the detector resolution function over the CTR. The structure factor is proportional to area under the peak. The error on each point is √n.

well-known Simpson's rule); this approach gives a more accurate determination of the area under a non-standard peak but a meaningful calculation of errors is difficult. The counting error on integrated intensities is typically around 1-3 %. However, there is a systematic error, determined from comparing symmetry equivalent reflections, which is more like 5 % – 10 %, and this must also be included.

4.5.2 Stationary Scans

Instead of an angular rocking scan an area detector can be used to integrate the entire width of the CTR in one go. This approach offers the advantages of decreased collection time, better background detection and increased counting statistics [52]. It is also easier to identify unwanted contributions to the signal and spot any peak asymmetry. In Figure 4.5 (a) an image from a Piliatus 100K area detector is shown.

The simplest way to extract the CTR intensity is to choose a 'region of interest' (ROI) containing the signal and sum the counts in each pixel. A representative background region is then chosen and subtracted from the signal. One of the main draw backs of this scanning mode is that if a sample has a significant mosaicity the integrated intensity will not reflect this, unlike a rocking scan. Another issue is in the increased complexity of data analysis, even using ROIs involves a significant increase in analysis time. The use of ROIs may not be the most accurate method of extracting intensities, fitting something like a 2D Lorentzian may be more appropriate. Technically each pixel on the detector also has a different reciprocal space coordinate that should be accounted for.

4.5.3 Reciprocal Space Scan

In a direct reciprocal space scan, the diffractometer scans along a plane (normally at a fixed Q_z value) in reciprocal space. This allows structures with a different periodicity (such as a reconstruction) to be investigated. This is scan type used extensively in the following chapter.

4.6 Data Analysis

4.6.1 Correction Factors

Measured integrated intensities are affected by several factors related to the beam and the sample, these will depend on the diffractometer angles. The correction factors for the 2+3 diffraction geometry are given below:

The Lorentz factor

This factor accounts for the fact that the intensity in a rocking scan is integrated in angular space not reciprocal space. For a 4-circle diffractometer it is simply:

$$L = \frac{1}{\sin 2\theta} \tag{4.3}$$

For a 2+3 circle diffractometer L is given by:

$$L = \frac{1}{\sin \delta \cos \gamma} \tag{4.4}$$

The Polarisation Factor

This factor accounts any change in intensity caused by beam polarisation. As a synchrotron is typically horizontally polarised, experiments are typically performed with Q in the vertical plane leading to P = 1. For a horizontal geometry P = cos ($2\boldsymbol{\theta}$)**.** The 2+3 geometry can scan the detector in both planes, the polarisation factor is then:

$$\boldsymbol{P = p_h P_{hor} + (1 - p_h) P_{ver}} \quad \textit{where:}$$

$$\boldsymbol{P_{hor} = 1 - (cos\,\delta\, sin\,\gamma)^2} \tag{4.5}$$

$$\boldsymbol{P_{ver} = p_h P_{hor} + (1 - p_h) P_{ver}}$$

Rod Interception

Rod interception accounts for the angle that the detector makes with the rod. The area of interception of a plane cutting a rod at 90 ° will be that of a circle, for any other angle it will be that of an ellipse. The correction factor for both geometries will be:

$$\boldsymbol{R = cos\,\beta_{out}} \tag{4.6}$$

Active Area Correction

This correction accounts for the overlap of the beam footprint and the detector footprint on the sample, it depends on beam defining slits, detector slits and sample geometry and is best calculated numerically as in ref [53]. The active sample area ignoring the footprint and sample size for a 2+3 diffractometer is:

$$A = \frac{\cos \beta_{out}}{\sin \delta} \tag{4.7}$$

The integrated intensities are converted to structure factors through division by these factors.

4.6.2 Non-linear Least Squares Fitting

Once structure factors have been obtained, the model described in Chapter 3 is fit to the data using a non-linear least squares algorithm. The parameters defining the model are varied to minimise a $\chi 2$ value given by:

$$\chi^2 = \sum \frac{(M - T)^2}{\sigma^2} \tag{4.8}$$

Where M are the measured values and T the theoretical ones, σ^2 is the variance of the data. Division by the number of degrees of freedom (number of values – number of parameters – 1) yields the reduced $\chi 2$ measure.

5 ELECTROCATALYSIS AND THE AU (111) RECONSTRUCTION

5.1 Introduction

Gold catalysis has received considerable attention in the last few decades since the discovery by Haruta and co-workers of the enhanced catalytic activity towards the oxidation of carbon monoxide of gold nanoparticles on oxide supports[54–56]. Recently, this has been emphasised in electrocatalysis, where the promoting effect of adsorbed carbon monoxide on the oxidation of alcohols by gold catalysts has been examined. Rodriguez, Koper and co-workers have described the enhanced catalytic properties in a series of papers[10,57–61]; this is unexpected since CO is normally considered a poison in catalysis. It has been suggested that the presence of adsorbed CO can lead to OH adsorption at negative potentials in alkaline solution and this is the origin of the extraordinary electrocatalytic activity; in which the onset of methanol oxidation occurs at a significantly lower potential[10]. The key effect is highlighted by cyclic voltammetry (CV) measured after saturation of the solution with CO and subsequent purging of CO from the electrolyte. In this case, cycling the potential over a restricted range (so that the

adsorbed CO is not oxidatively stripped from the Au surface) shows the appearance of a sharp reversible peak around 0.4 V (vs. RHE), not observed in the absence of pre-adsorbed CO. It has been suggested that the sharpness of the CV peak indicates a structural transition [10,57]. Interestingly this voltammetric feature is only observed on hexagonally close-packed surfaces, i.e. the single crystal Au (111) surface, which at negative potentials in alkaline electrolyte is reconstructed into the (p x √3) phase (the stripe domain phase where p=22 under UHV conditions) and the Au (001) surface, which at negative potentials in alkaline electrolyte forms a 'hex' reconstruction [62–64]. Previous work has already demonstrated that unlike in acidic media, in alkaline solution CO extends the potential range over which the reconstruction is stable [64]. In this chapter SXRD is used to gain detailed structural information of the Au (111) reconstruction both with and without the presence of adsorbed CO. These measurements were made in both a baseline KOH solution and solutions containing methanol and ethanol. By combining SXRD measurements of the scattering from the surface Au monolayer (reconstructed at all potentials into a (p x √3) phase) with dynamic potential dependant measurements of X-ray scattering the effect of different reactants on the surface structure of the gold electrode can be explored. In the presence of CO and methanol there seems to be a partial lifting of the surface reconstruction, resulting in a more disordered and potentially reactive electrode surface. In contrast, ethanol seems to protect the surface reconstruction.

5.2 Experimental details

The experimental procedure was as described in chapter 4 and other studies such as refs. [65,66]. The reference electrode used in the X-ray cell was a leak-less Ag/AgCl (Fisher Scientific, 66-EE009 "No leak" Ag/AgCl Reference electrode cat #: 13463578) but all potentials are quoted versus RHE for comparison with previous CV studies. Prior to each

experiment, the potential was cycled for ~30 minutes in the electrolyte solution over the range 0 V – 1 V (at 50 mV/sec) and then held at 0.12 V. This was to ensure reproducible surface preparation ('surface conditioning') in each case. X-ray measurements were performed on beamline BM28 (XMaS), the UK-CRG beamline at the ESRF, Grenoble using focused incident X-rays of energy 11 keV. During the experiment the outer chamber of the X-ray cell was continuously purged with nitrogen to protect the surfaces from oxygen. For CO adsorption, the electrolyte was saturated with CO and the CO-saturated electrolyte pulled through the electrochemical cell and with the potential held at 0.12 V. The X-ray Voltammetry (XRV) data presented is background subtracted by fitting a Lorentzian peak with a linear background to a rocking scan and subtracting the background at the peak centre from each point. The electrolytes investigated were: a 0.1 M KOH 'baseline' solution, and solutions containing 2.5 M methanol and 0.1 M ethanol. Semi-conductor grade (99.9 % trace metal basis, Sigma-Aldrich) and ultra-pure water (MilliQ™ 18.2 Ω M cm^{-1}) was used for the base electrolyte. The methanol was UHPLC grade (Ultra-CHROMASOLV™, Sigma-Aldrich) and the ethanol was absolute HPLC grade (CHROMASOLV™, Sigma-Aldrich).

5.3 Results

5.3.1 Cyclic Voltammetry

In alkaline solution the voltammogram of Au (111), Figure 5.1 (a), has a large 'double layer' region from 0 V to ~ 1.0 V, around 1.1 V there is small peak attributed to the lifting of the Au (111) - (22 x √3) reconstruction. Further positive is a large peak due to oxide formation. However, when CO has been 'pre-adsorbed' onto the Au surface, that

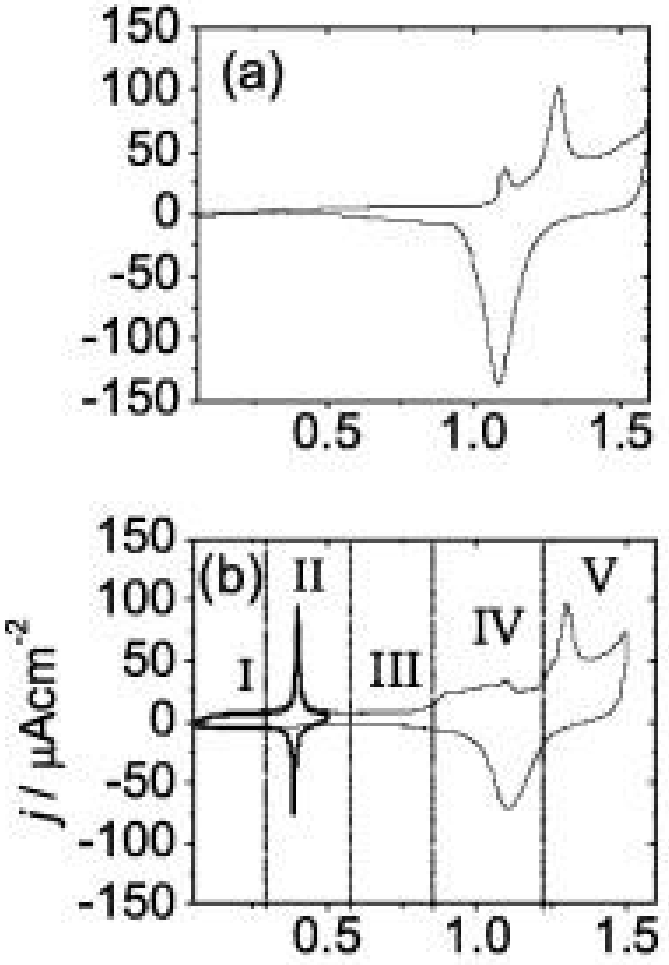

Figure 5.1. Voltammetric profiles at 50 mV s−1 of the Au(1 1 1) electrode in 0.1 M NaOH (a) in absence of CO, (b) in presence of chemisorbed CO. Reproduced from reference [57] with permission from Elsevier.

is the solution is saturated and then purged with the potential held negative (e.g. 0.1 V) there is reversible peak around 0.4 V, shown in Figure 5.1 (b). It has been suggested that the sharpness of this peak indicates a structural transition[57]. In the case of methanol being present in the solution with CO there is a small increase in current just positive of the peak at 0.4 V indicating that onset of methanol oxidation [10]. In contrast, in the absence of CO, oxidation of methanol does not occur until ~1.2 V.

5.3.2 The effect of CO in alkaline electrolyte

In the UHV environment the clean, low-index surfaces of Au have been shown to reconstruct under certain conditions of sample temperature and surface preparation[67]. These reconstructions all survive transfer into electrolyte and the nature of the electrode surface structure (reconstructed or unreconstructed) can then be controlled by the application of an electrical potential across the electrode/electrolyte interface[67–70]. The reconstructed Au (111) surface is often called a 'stripped' phase as the surface stacking distorts from an ABC to an ABA stacking sequence in the centre of the unit cell leading to stripes that can be seen with techniques such as STM. This distortion increases surface density, corresponding to a uniaxial compression where p+1 surface atoms sit in place of p, a compression of (p+1)/p -1 = 1/p (~4.5 % for p=22). This is illustrated in Figure 5.2.

In reciprocal space this (p x $\sqrt{3}$) reconstruction gives rise to a well-defined diffraction pattern which, in the surface plane of reciprocal space, is characterised by a hexagon of additional diffraction spots around the scattering that occurs for the bulk Au (111) crystal [68]. This is schematically illustrated in Figure 5.3 which shows a map of the scattering that occurs in reciprocal space around (0, 1, 0.3), close to a so-called 'anti-Bragg position' on the (0, 1, L) crystal truncation rod (CTR). Figure 5.4 shows the scattered intensity measured along the [1, 1, 0] direction through the (0, 1, 0.3) reciprocal lattice position (the scan direction q_r, indicated in Figure 5.3) at two potentials. The potentials (0.2 V and 0.5 V) were selected to be before and after the sharp cyclic voltammetric feature seen in presence of CO, which is discussed above. The upper

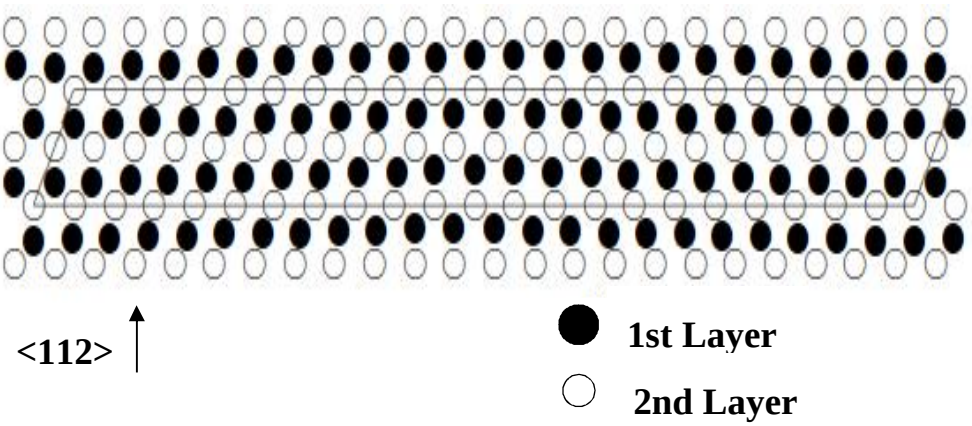

Figure 5.2. Illustration showing the Au (111) -√3 x 22 surface reconstruction.(reproduced from [68] with permission from The American Association for the Advancement of Science)

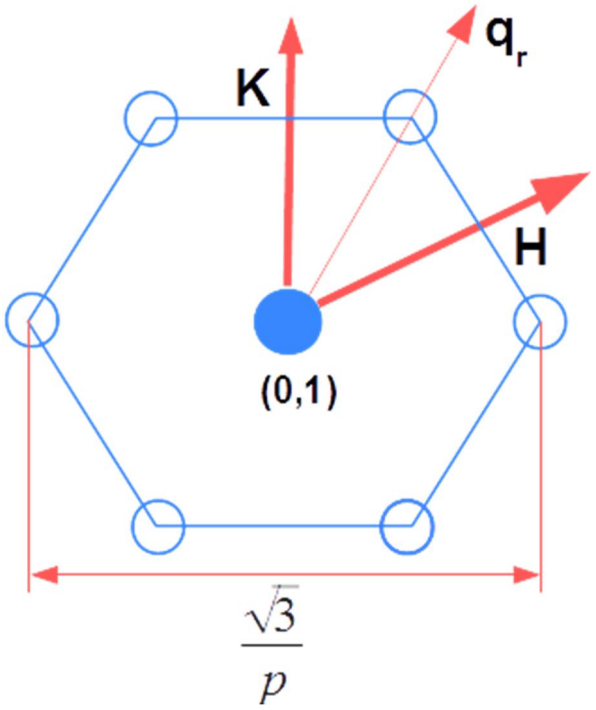

Figure 5.3. Reciprocal space map of the reconstructed Au (111) surface. A schematic of the scattering in the surface plane of reciprocal space around the (0, 1 0.3) CTR (solid symbol) indicated are the peaks that arise due to the (p x √3) reconstruction (open symbols) and the direction (q_r) of scans made in Figure 5.3.

potential limit is also sufficiently negative to the potential at which the reconstruction begins to lift. In each scan shown, two clear peaks can be seen, one at H, K ~ 0, corresponding to the scattering from the (0, 1, L) CTR and a peak at H, K ~ 0.02 which arises due to scattering from the reconstructed surface layer. Figure 5.4 (a) is measured prior to the adsorption of CO whereas Figure 5.4 (b) was measured after CO had been irreversibly adsorbed on the electrode's surface. The peak position is directly related to the periodicity of the reconstruction and can vary as a function of the applied electrode potential [71]. By fitting a double Lorentzian line shape to the data shown in Figure 5.4 both values of stripe separation, p, and the correlation length, ζ, can be obtained. The Lorentzian line shape is derived from a 1D real space atomic model in which ζ decays exponentially with a length $\zeta=a/(2\pi\sigma)$, where σ is the full width half maximum (FWHM) of the peak in units of H. This correlation length is a measure of the distance over which atoms in the reconstructed surface layer are positionally correlated. In these units p, is given by $p=1/(2\Delta H)$, where ΔH is the separation from the CTR position (at H ~ 0), to the position of the peak due to the reconstruction, projected along the H reciprocal space direction[68]. That is, p is the stripe separation in terms of the lattice distance a, where the real space distance is then L = pa. It should be noted that the line shape can be affected by substrate mosaic effects which have a Gaussian component and, additionally, can have an asymmetry caused by a distribution of domains with a range of p values. These effects are not included in the Lorentzian model however the essential structural information can be extracted from the analysis.

In Figure 5.4 (a) there is a small shift in the position of the peak due to the reconstruction, around h ~ 0.02, between the two potentials. This shift in peak position corresponds to a change in stripe separation of 0.54 ± 0.07 a (i.e. 1.6 ± 0.2 Å) which represents a change in uniaxial compression along the <100> direction from 4.35 % to

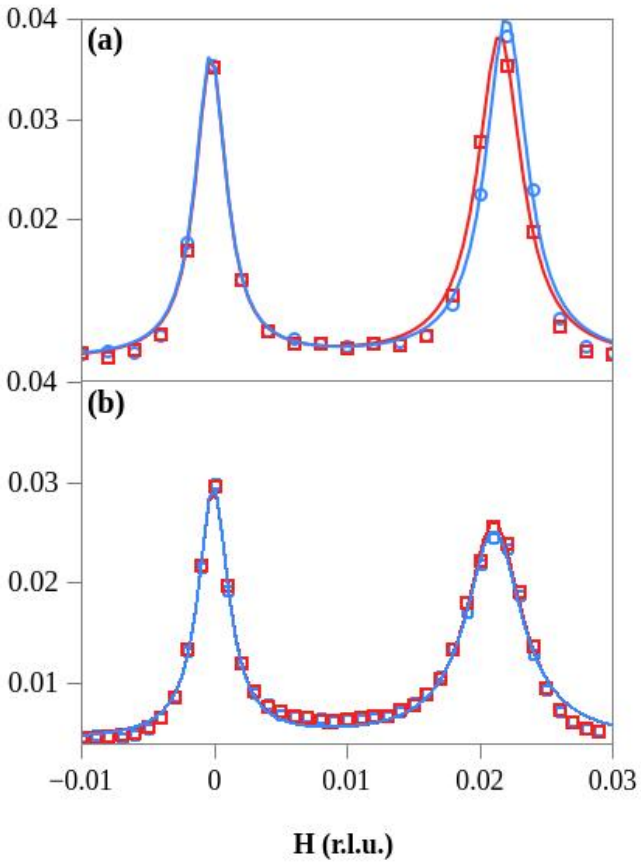

Figure 5.4: In plane X-ray diffraction from the reconstructed Au (111) surface**.** Measured along the [1,1,0] direction (indicated by q_r in Figure 5.3). The blue symbols show measurements at 0.2 V whereas the red ones indicate measurements made at 0. 5 V. (a) was measured in the absence of CO. (b) was measured after CO had been adsorbed on the Au surface and the electrolyte subsequently purged.

4.45 %. In Figure 5.4 (b), after the pre-adsorption of CO, there is no significant change in stripe separation where p = 23.66 ± 0.05 (i.e. 4.22 % compression) at both potentials. There is also a reduction in the relative intensity of the peak due to the surface reconstruction, compared to that due to the CTR, when CO is pre-absorbed. Given that it has been shown that the scattering from the surface reconstruction arises from a single

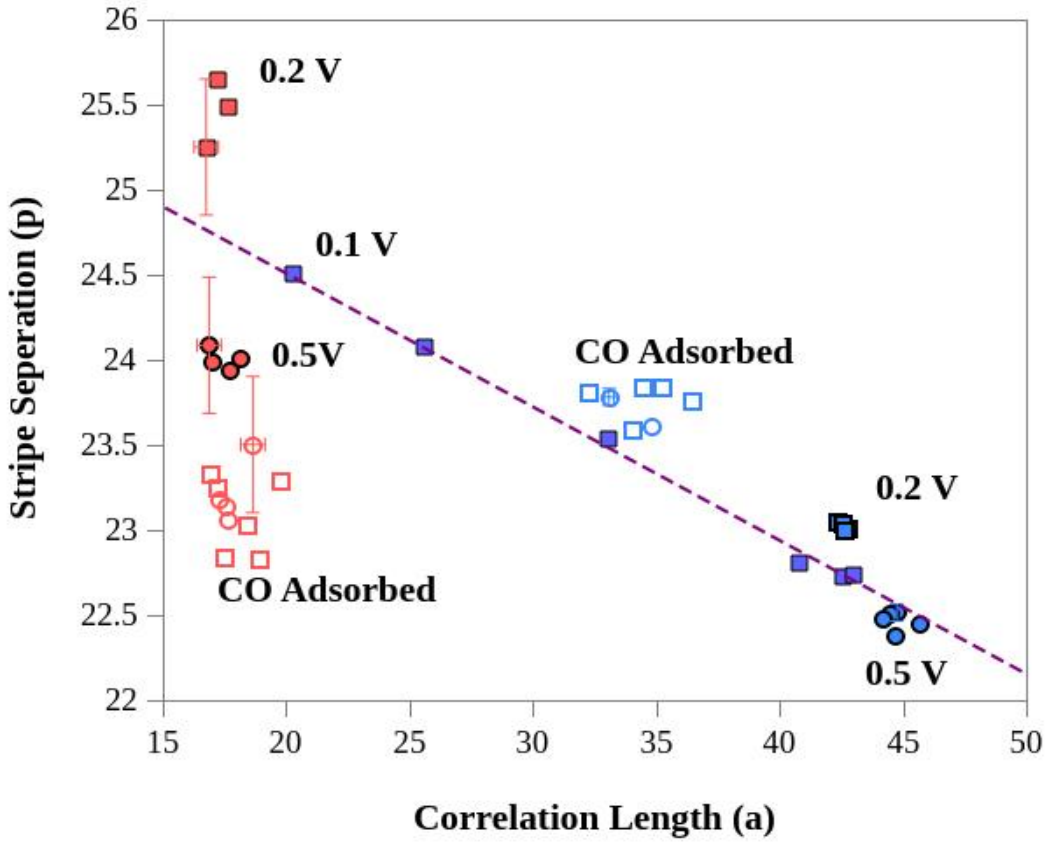

Figure 5.5. The relationship between coherence length and stripe separation. Red and blue symbols show the results of measurements obtained from two Au (111) samples. Solid symbols represent measurements taken in the absence of CO and open symbols with CO irreversibly adsorbed on the surface. The purple symbols represent measurements made at 0.1 V between electrochemical conditioning for the sample shown by blue symbols. The dashed line indicates the general trend during conditioning cycles. The measurements shown with square symbols are taken at the negative potential limit (0.2 V) and those with circles at the positive limit (0.5 V). Error bars are shown for a few data points to, the y error on the blue and purple symbols is approximately equal to the height of the symbols.

atomic Au layer [71] this decrease in intensity can only be attributed to an increase in disorder or a reduction in coverage of the surface reconstruction. The measurements presented were made on a Au (111) surface that had been cycled until no increase in the scattered intensity due to the reconstruction was observed. In this 'groomed' surface state the reconstruction is known to have maximum compression and correlation length [68]. In Figure 5.5 the correspondence between stripe separation and correlation length is explored. The data was measured for the sample also used in Figure 4.4 (blue), the same sample during electrochemical 'grooming' (purple), and an additional sample where the surface was known to be less ordered. It seems that despite similar preparation procedures the exact stripe separation and correlation length depends upon the nature of the sample being investigated. Initial electrochemical cycling improves the correlation length (domain size) of the reconstruction but there is a sample dependant limit on the maximum correlation length that can be achieved. The effect of electrochemical cycling upon correlation length is shown by the dotted line, where the order the measurements were made is from left to right, i.e. there is a clear linear correlation between domain size and stripe separation. Both samples (data shown with solid red and blue symbols) show a clear change in stripe separation with potential, this represents a shift in peak position on [H, K] scans such as in Figure 5.4. However, upon CO adsorption there is a dramatic shift in stripe separation; in the samples measured this is not always followed by the equivalent change in correlation length, in line with the above linear trend. If the sample indicated by red markers were to follow the linear trend between correlation length and stripe separation, then after the adsorption of CO the domain size would increase beyond that which was achievable with electrochemical cycling, this is not the case, instead, there is a decoupling of the two parameters. For the sample indicated by blue symbols one would expect a decrease in domain size, which is what happens. With CO adsorbed there is also

no longer any clear potential dependence in the stripe separation, the reconstruction appears to be ‘pinned’.

Complementary information on the potential dependence of the surface structure can also be obtained by measuring the scattered X-ray intensity as a function of applied electrode potential, a measurement known as 'X-ray voltammetry' (XRV)[72]. Figure 5.6 shows the potential dependence of the scattered intensity from the Au (111) surface at (a) (0.019, 1.019, 0.3), (b) (0 0 1.52), and (c) (0 0 2.7), Figures (d) to (f) show the same measurements made after the pre-adsorption of CO. Each cycle shown starts at 0.22 V and then increases to 0.55 V at 5 mV/s (solid symbols), the potential then decreases back to 0.22 V at the same rate (empty symbols). In Figures 5.6 (a) and 5.6 (d) the scattering corresponds to that from the ($\sqrt{3}$ x p) reconstruction peak (positioned at the centre of the peak due to the reconstruction at 0.22 V). Since the position of the peak can vary as a function of potential the measured intensity at this position does not directly correspond to the peak intensity, however clear differences between Figures 5.6 (a) and 5.6 (d) can be observed.

First is that any change in intensity (in this case corresponding to a shift in peak position) is suppressed in the presence of pre-adsorbed CO. Second the overall intensity in the presence of CO is reduced, this implies that CO partially lifts the Au (111) reconstruction. Figures 5.6 (b) and 5.6 (e) show the scattered intensity at (0 0 1.52) versus applied potential, this is an 'anti-Bragg' position and provides information on both the gold surface layers and adsorbed anion species. Both without and with pre-adsorbed CO there is a small increase in scattering with potential. As there is no reduction in intensity at this position with potential the transition at 0.4 V, seen in Figure 5.6 (a), must occur entirely in the plane of the reconstructed surface layer. Furthermore, the XRV in Figures

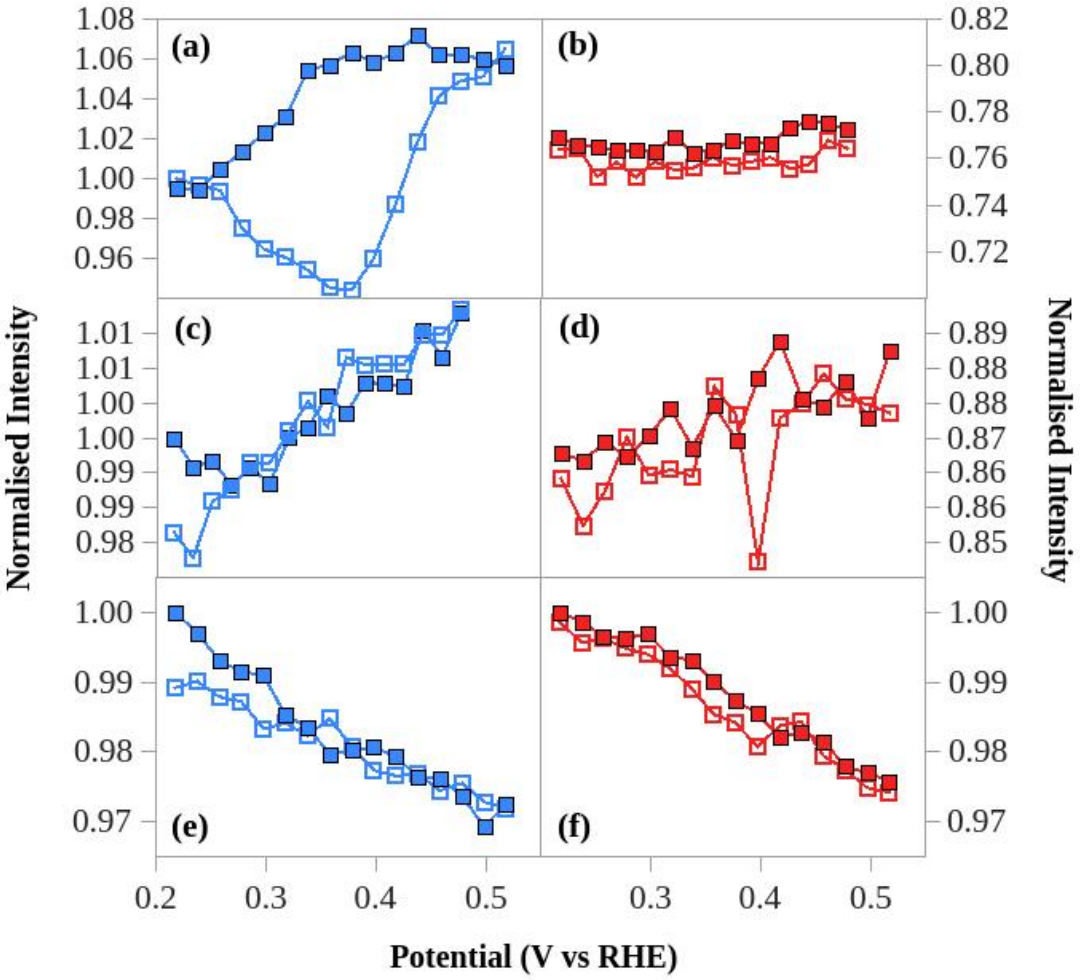

Figure 5.6**:** X-ray voltammetry monitoring changes in the gold surface**.** (a) scans measured on the peak due to the reconstructed surface at (0.019, 1.019, 0.3) without (blue) and with the presence of adsorbed CO (red). (b) measured at (0, 0 ,1.52) a specular anti-Bragg position, sensitive to changes in electron density of the electrochemical interface, again with and without CO. The intensity is background subtracted using either a rocking or reciprocal space scan and normalised for each position to the first point the absence of CO.

5.6 (c) and 5.6 (f) measured at (0 0 2.7) only shows a gradual change that is similar both with and without the presence of pre-adsorbed CO. The scattering measured at the (0 0 2.7) reciprocal space position is relatively unaffected by adsorbates but very sensitive to the distance between the top two gold layers, the dynamics of which does not appear affected by the presence of CO. The observation of an overall reduction in scattered intensity at (0.019, 1.019, 0.3) and (0 0 1.52) indicates an increase in disorder of the reconstructed surface gold layer with CO adsorption. A reduction in the coverage of the reconstructed layer can be ruled out since a similar reduction in scattering is not seen on the non-specular CTR in Figure 5.4 (b).

At positive potentials the reconstruction begins to lift and the dynamics are affected by the presence of CO [64]. In Figure 5.7 the XRV shown in Figures 5.6 (a) and 5.6 (d) are extended to the potential where the reconstruction begins to lift, which is characterised by a reduction of intensity at the (0.019, 1.019, 0.3) reciprocal space position. The reconstruction in its fully 'groomed state' (i.e. after the intensity stops increasing with electrochemical cycling) is the least stable. There is a dip in measured intensity around 0.4 V and the reconstruction also begins to lift at a much lower potential (~ 0.7 V). This is in contrast to the reconstruction that has not been fully formed through electrochemical cycling. For this 'partially groomed' reconstruction where overall intensity was ~ 60 % of the fully formed reconstruction intensity there is no change around 0.4 V and the reconstruction only starts to lift at much higher potentials. However, the onset of lifting is consistent when one views this reconstruction as already partially lifted, then the reconstruction only begins to lift where the fully 'groomed' reconstruction would also have ~60 % intensity (this is shown by the grey dashed line). CO on the other hand appears to both partially lift the reconstruction (the overall intensity is lower) but

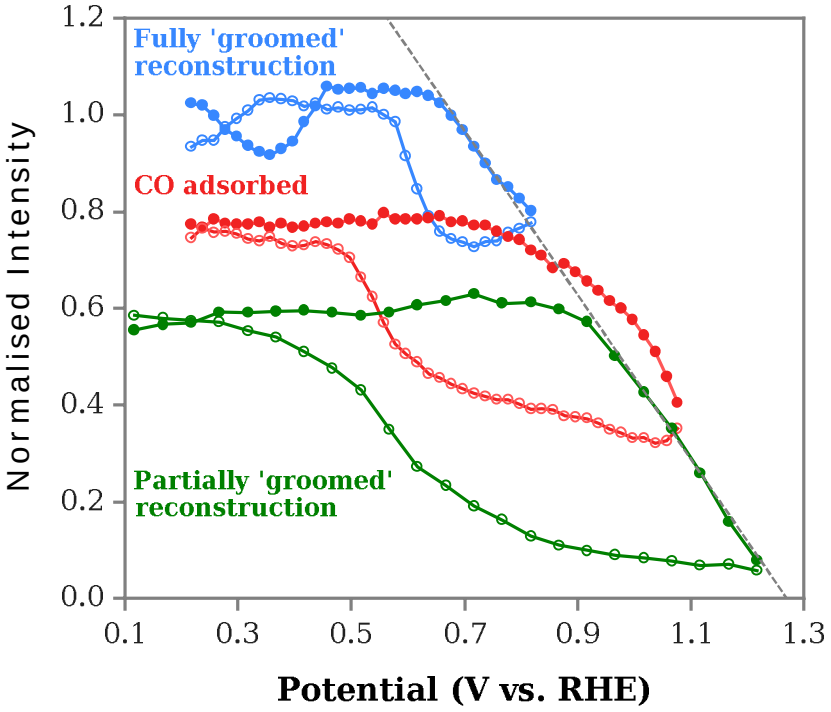

Figure 5.7. Lifting of the Au (111) reconstruction. The scattering was measured at the reciprocal space peak around (0.019, 1.019, 0.3) positioned using the peak of an in-plane reciprocal space scan at 0.2 V. The ‘groomed’ state is that after which no improvement in the scattered intensity from the reconstruction is observed with electrochemical cycling. The scan rate was 2 m/Vs.

also extend the potential at which further lifting occurs past that expected with just KOH (indicated by the dashed grey line).

5.3.3 Methanol and Ethanol

The effect of methanol and ethanol on the reconstruction was also investigated, however the thin-layer arrangement of the cell limits diffusion making such measurements difficult. In Figure 5.8 reciprocal space scans (such as those in Figure 5.4)

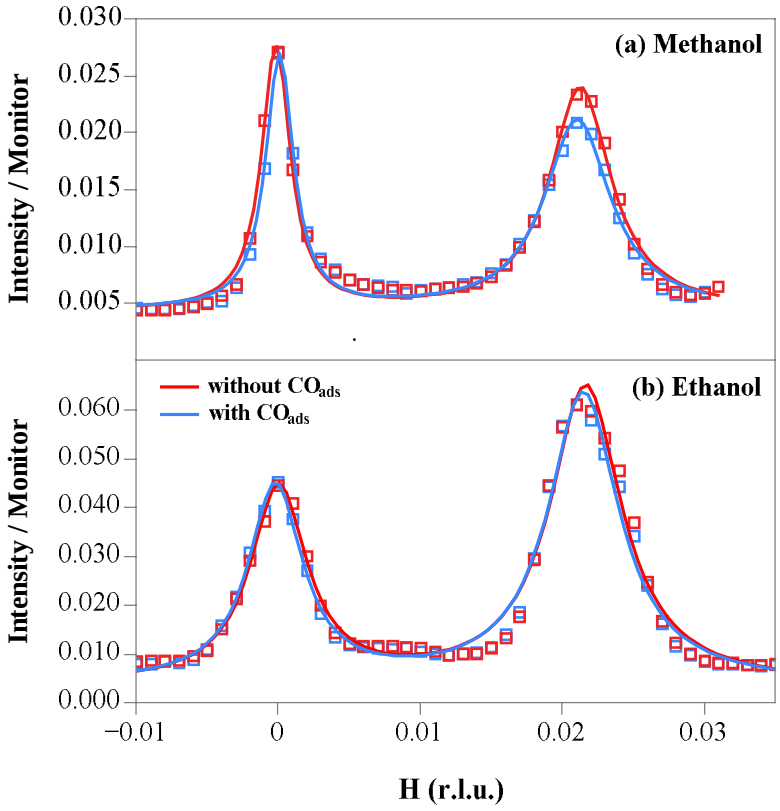

Figure 5.8. In plane X-ray diffraction from the reconstructed Au (111) surface. (a) 0.1 M KOH with 2.5 M methanol measured at 0.25 before the adsorption of CO (blue) and after the cell was saturated with CO (red). (b) 0.1 M KOH with 0.1 M ethanol measured at 0.25 V before the adoption of CO (blue) and again after CO adsorption (red).

are presented for two different electrolytes, one containing 2.5 M ethanol and another containing 0.1 M ethanol. The observed intensity from the reconstruction relative to that from the CTR is reduced in the case of methanol but increased with ethanol. This suggests that methanol itself partially lifts the surface reconstruction whereas ethanol does not. When CO is pre-adsorbed on the surface with methanol there is a small increase in intensity from the reconstruction (Figure 5.8 a), suggesting the CO slightly improves the ordering of the reconstruction. However, with ethanol is present (Figure 5.8 b) there is only a negligible increase in the reconstruction peak.

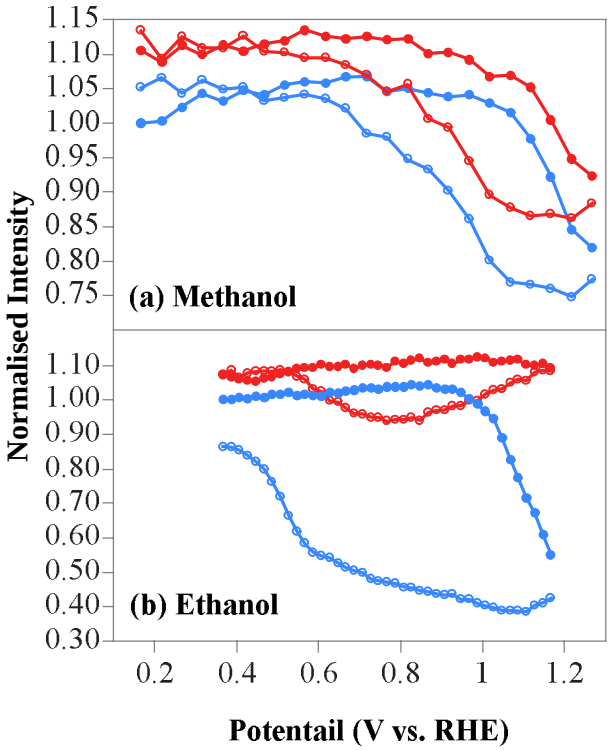

Figure 5.9. Lifting of the reconstruction with methanol or ethanol. The scattering was measured at the reciprocal space peak around (0.019, 1.019, 0.3) positioned using the peak of an in-plane reciprocal space scan at 0.2 V. (a) Measured in electrolyte containing 2.5 M methanol (b) Measured in electrolyte containing 0.1 M ethanol. Blue symbols were measured in the absence of CO whereas red ones were measured after the solution had been saturated with CO. The scan rate was 2 mV/s.

In Figure 5.9 XRV at measured at the peak around the (0.019, 1.019, 0.3) reciprocal space position is shown, as above the intensity at this position is sensitive to the order of the reconstructed surface layer, as well as its coverage. In Figure 5.8 (a) the potential at which the reconstruction begins to lift is around 1.1 V which is much further positive than that either with just KOH or when is CO present, in fact the reconstruction seems to be present well into the oxidation of methanol. When CO is present in the solution the scattering from the reconstruction is increased (in agreement with Figure 5.8 a) but also it lifts at an

even higher potential. So while the presence of methanol modifies the reconstruction it is further modified by the addition of CO. Unfortunately, due to the thin-layer arrangement systematic scans at different potentials around 0.4 V were difficult.

The measured scattering around (0.019, 1.019, 0.3) as the potential was swept positive, with 0.1 M KOH + 0.1 M Ethanol, is shown in Figure 5.9 (b). The measurement indicates that the reconstruction does not begin to lift until the potential reaches around 1 V which coincides with the onset of ethanol oxidation [73]. Subsequent cycles were limited by the thin-layer arrangement, where the reactants can be exhausted, and then seemed to lift closer to that that seen with just 0.1 M KOH, suggesting no significant modification to the electrode surface. In the presence of CO, Figure 5.9 (b) shows no evidence of any lifting over the entire potential range. It seems with ethanol and CO the reconstruction is protected well into the oxidation of ethanol with no evidence of lifting at all.

5.4 Discussion

In UHV gold is mostly inert to CO however high pressure STM studies of CO adsorption have indicated there is a thermally activated reaction between Au and CO that involves a significant displacement of Au atoms where on-top adsorption of CO is accompanied by step edge roughening [74]. Elevated pressure SXRD has demonstrated that CO causes a partial lifting of the surface reconstruction, where the ratio of fcc to fcp sites doubles after exposure to CO[75], the terrace size is reduced, and the herringbone arrangement effectively removed. In the electrocatalysis of alcohols these structural changes caused by CO have largely been ignored despite clear suggestions of a structural influence in the ability of CO to enhance the electro-oxidation of certain alcohols [10]. Indeed there is a growing body of knowledge e.g. [76–78] showing how surface dislocations and strain can

enhance catalytic activity in metals such as gold. The d-band orbitals for a perfect gold surface are fully occupied; whereas a surface with kinks and dislocations has active sites with partially filled d orbitals, similar to platinum, and is therefore able to catalyse reactions involving free-radical species such as OH· [79]. In fact the early onset of methanol oxidation in alkaline media has already been demonstrated for rough gold [80], gold nanoparticles [81] and Au (210) surfaces with defects [82], all in the absence of CO. A recent report has demonstrated how the adsorption of CO on Cu (111) catalytically activates the surface through the formation of Cu nanoclusters[83], it was also suggested that a similar effect may occur on other soft metals such as Au and Ag.

In this chapter it has been shown how CO induces a structural change that is consistent with the partial lifting of the Au (111) surface reconstruction in alkaline solution. It has been shown methanol leads to a similar reduction in the scattered intensity from the reconstructed surface as that from CO. Since the early onset of methanol oxidation only occurs when CO is adsorbed on the surface it seems reasonable to suggest that any modification of the Au (111) surface by methanol may differ from that by CO, if indeed this structural change is related to the enhanced catalytic activity. *In-situ* STM studies of Au (111) in aqueous solutions containing methanol are not available but it would be interesting to see how the presence of CO affects the surface structure in such measurements. With ethanol, a molecule whose oxidation is not promoted by CO adsorption in alkaline solution, there is no evidence of a reduction in scattering from the reconstruction either with or without the presence of CO. Ethanol seems to protect the gold surface. This could be the result of the ethanol oxidation consuming both OH and CO species in a Langmuir-Hinshelwood type reaction [84].i.e.

$$CO_{ad} + OH_{ad} \rightarrow CO_2 + H^+ + e^- \qquad (5.1)$$

Another interesting phenomenon shown in this chapter is that in the baseline KOH electrolyte, CO prevents a change in lateral compression of the reconstruction around the same potential where a voltammetric peak has been observed in other reports [57]. This feature has been ascribed to CO inducing OH adsorption where nearest neighbour OH and CO enhance each other's bonding. If in the absence of CO it is energetically favourable for the compression of the reconstruction to change around this potential, then what happens when CO causes a 'pinning' of the reconstruction? It is plausible that this could result in a transfer of charge to adsorbed species. This CO induced modification to the compression of the Au (111) surface in KOH, this would also correspond to a change in surface strain. DFT calculations of strained Pt surfaces and Pt nanoparticles have indicated that the reactivity of Pt nanoparticles can be replicated with strained (111) surfaces [85]. All this has the potential to impact upon gold's performance as an electrocatalyst and warrants further theoretical investigation.

5.5 Conclusions

CO induces structural changes in the Au (111) surface reconstruction in alkaline electrolyte. There is both a partial lifting and a change in the lateral compression of the reconstructed metal layer upon CO adsorption. It has been shown how the presence of CO and various alcohols also alter the dynamics of the lifting of the reconstruction. These results indicate that the surface reconstruction needs to be considered in detail if gold catalysis is ever to be fully understood and offer alternate way to explain the unexpected catalytic activity of Au (111). The results re-enforce the need for large scale theoretical modelling capable of accounting for the entire reconstructed unit cell as well as the impact of step-edges, kinks and dislocations. The importance of detailed structural information of electrode interfaces, such as that obtained from SXRD, is also apparent.

6 NON-AQUEOUS ACETONITRILE ON PT (111) ELECTRODES

6.1 Introduction

The controlled formation of reduced oxygen species in aqueous electrolytes has been extensively studied across many biological and energy storage systems [13,86–88]. In looking beyond lithium intercalation technology and moving towards lithium conversion devices including alkali metal oxygen (M-O_2) and alkali metal sulphur (M-S) systems, an understanding of non-aqueous electrolyte/metal interfaces is crucial to battery research [13,89]. Non-aqueous electrolytes have a much wider polarisable potential range than their aqueous counterparts, allowing the utilisation of otherwise inaccessible redox couples, such as the formation of superoxide from dioxygen (O_2). Such systems are governed by interfacial electrode processes which are dependent on electrode surface morphology and electrolyte composition [12,90–96]. The contamination of platinum (Pt) cathodes in proton exchange membrane fuel cells by acetonitrile (MeCN) is an active area of research due to the inhibiting effect of MeCN on the oxygen reduction reaction (ORR) in aqueous media [97,98]. Pt is an advantageous

electrode material to study because it exhibits high catalytic activity towards the ORR in both aqueous and non-aqueous media [99,100]. MeCN has been used extensively as a non-aqueous solvent to investigate superoxide formation, due to its ease of preparation as a high purity and low water content solvent (< 4 ppm H_2O) [88,101–103]. However, it has been reported that on roughened Pt, MeCN dissociates leaving a cyanide and methyl group [104,105]. While there have been a few studies investigating the Pt(111)/MeCN electrode interface [106–109] very little is known about the interfacial region at the molecular scale, especially in the absence of water. Baldelli *et al*. [107] used sum frequency generation to infer that in the absence of water the MeCN molecule undergoes a potential dependent reorientation, which was also observed with surface enhanced Raman spectroscopy upon gold [102]. The work of Baledelli *et al*. [107] suggested that the methyl-group pointed towards the electrode surface at potentials negative of the potential of zero charge (*pzc*) and the nitrile group towards the electrode at potentials positive of the *pzc*; they found that small amounts of water enhanced this effect. The presence of water greater than 0.05 mole fraction (50,000 ppm) was found to disrupt any reorientation of MeCN. In the presence of excess water, MeCN is also thought to be reactively chemisorbed on Pt, where it is found to undergo, almost fully reversible, reduction and oxidation with little or no desorption [108]. In contrast such a process is not thought to occur in the absence of excess water, as the first step is assumed to be proton mediated [107,109]. MeCN is also found to co-adsorb with H, blocking some of the available sites for H_{upd}, and even displacing pre-adsorbed hydrogen [110].

Surface X-ray diffraction (SXRD) is one of the few techniques able to simultaneously provide structural information for both the electrode and the electrolyte sides of the electrochemical interface. Its use however is yet to be fully extended to the investigation of non-aqueous electrochemical systems. SXRD also offers an advantage

over *ex situ* techniques, such as low electron energy-diffraction, in that molecular adsorbates can be investigated without the same level of damage that is caused by a beam of charged particles. The few non-aqueous electrolyte systems that have been previously investigated are all ionic liquids [111–114]. In those experiments the sample environments were often hermetically sealed tubes that required the X-rays to pass through large volumes of liquid and, in addition, allowed only a restricted angular access for the incident and scattered X-ray beams with only X-ray reflectivity being measured. Other SXRD experiments with ionic liquids [115,116] have used a droplet cell arrangement [117] which offers very little protection from atmospheric water. In this this chapter an experimental setup that overcomes many of these limitations is described. *In situ* SXRD measurements are presented that probe the Pt(111)/dry MeCN interfacial structure, both in the absence and presence of dissolved O_2. Dynamic voltage-dependant measurements, so-called X-ray voltammetry (XRV), and static crystal truncation rod (CTR) data are shown. The results demonstrate a link between surface relaxation and applied potential that is independent of adsorption processes. Fits to CTR data and XRV measurements are consistent with the idea of the MeCN molecule undergoing a potential-dependant reorientation, but also suggest that this is disrupted by the presence of O_2. It is suggested this may be because the adsorbed MeCN molecule has dissociated at the electrode surface.

6.2 Experimental details

MeCN (MeCN) (≥ 99.9 %, Aldrich) was dried over freshly activated molecular sieves (4 Å) reducing water content to a value of ≤ 5 ppm water and deaerated using high purity argon (≥ 99.999%). This was determined using a coulometric Karl Fischer titrator (Mettler-Toledo).Tetrabutylammonium perchlorate ($TBAClO_4$) (≥ 99.0 %, Aldrich) was

dried under vacuum at 120 ºC for 16 hours before use. The electrolyte used was MeCN + 0.1 M $TBAClO_4$. High purity O_2 (≥ 99.999%), further dried with a water trap and desiccant drying tube, was used to oxygenate the electrolyte, this produced a final water content of < 20 ppm. Ag wire was used as quasi-reference electrode and referenced against an internal ferrocene standard. All potentials presented are quoted against the standard hydrogen electrode (SHE), where the ferrocene redox couple is found at +0.624 V [118]. Dry electrolytes and the Karl Fischer titrator were stored in an inert atmosphere glovebox with less than 0.1 ppm O_2 and H_2O. A Pt(111) 10 mm diameter disc electrode with a miscut < 0.1° was prepared by inductive RF heating at 1050 °C in a 3 % H_2–Ar gas mixture under constant flow for 10 minutes. The electrode was subsequently cooled to room temperature in the same atmosphere, in a sealed quartz tube. The sealed tube was placed in the glovebox through an evacuated antechamber. The cell, fittings and Pt wire counter electrode were cleaned by soaking for 24 hours in a 50:50 mixture of concentrated HNO_3 + H_2SO_4 and then rinsed and boiled in Mill-Q water (18.2 MΩ). Any oxide was removed from the Ag wire quasi-reference electrode using emery paper before cleaning. The polypropylene films were rinsed and boiled in Mill-Q water. The cell was then assembled in air and placed along with the separated polypropylene films and outer hood in the glovebox antechamber for 16 hours. The antechamber was evacuated and heated to 70 °C. The cell was rinsed with fresh electrolyte before use. Immediately after removal from the quartz tube the Pt(111) single crystal was covered with a drop of the electrolyte solution and transferred into the electrochemical cell at open circuit potential. The cell was then filled with electrolyte to just above the crystal and a polypropylene film secured over the top. Using a syringe any gas bubbles were removed and the film inflated with electrolyte to a thickness of a few millimetres. Following assembly an airtight outer hood was secured over the cell and the whole ensemble was placed in a sealed glass jar and

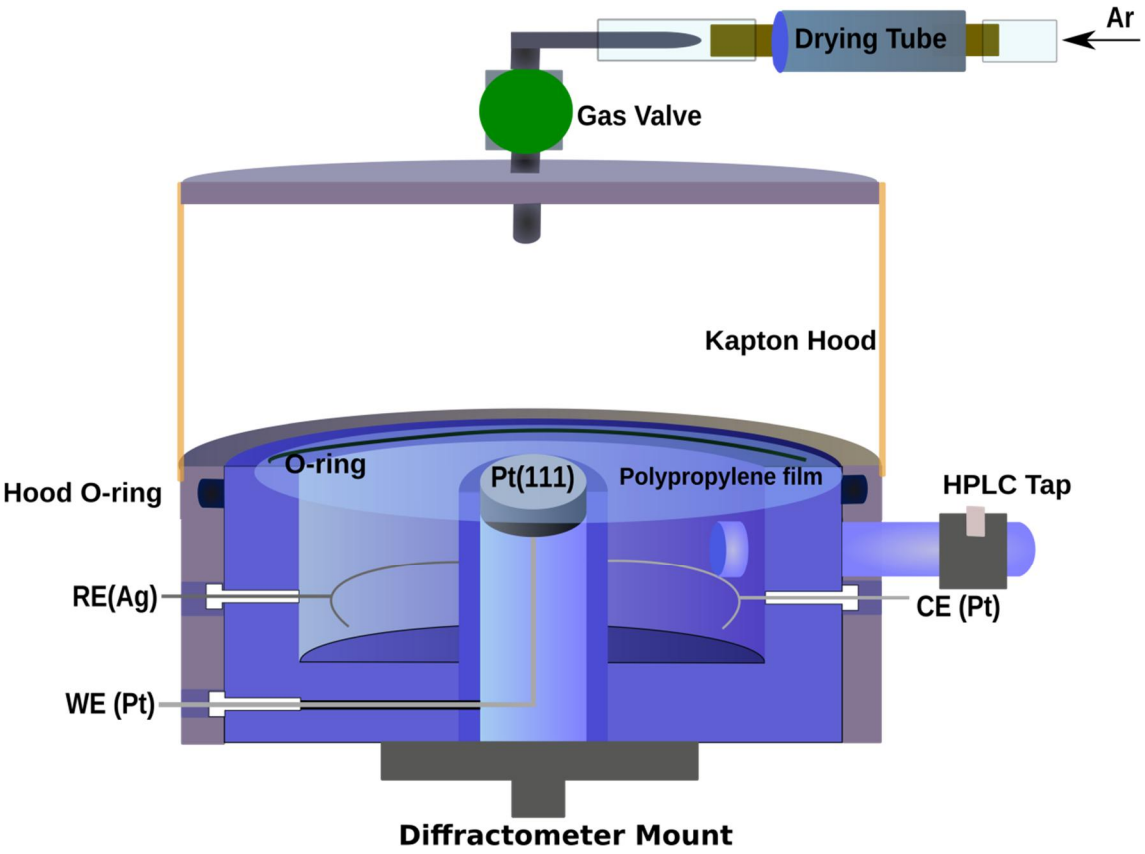

Figure 6.1: Schematic of the non-aqueous surface diffraction cell. The cell consisted of an inner Kel-F™ cell that was tapered towards the top to allow an effective seal to be me made with an outer hood when pushed up against an O-ring. The outer hood had a large cylindrical Kapton™ window that was bonded to the metal parts of the outer hood using an airtight epoxy resin. The reference, counter electrode, and the connection for the working electrode were polycrystalline wires, fed through airtight HPLC fittings. An inert HPLC tap connected to a glass syringe was used to remove gas bubbles and top up the electrolyte during assembly. At the top of the outer hood was a Swagelok™ tap connected a drying tube and an Ar gas line in order to provide a small overpressure.

transferred to the synchrotron beamline. Immediately after removal from the jar a desiccant drying tube was connected between the cell and an argon (≥ 99.9%) gas line to provide a small overpressure to the outer hood. Figure 1 shows a schematic of the experimental setup that was mounted on the diffractometer. The X-ray measurements were performed on the I07 beamline at the Diamond Light Source, UK, using a wavelength of 0.689 Å (18 keV). A 2+3 circle diffractometer with a PILATUS 100k (Dectris) detector was used to record the X-ray measurements. The Pt(111) surface was indexed using a hexagonal unit cell such that the surface normal lies along the $(0, 0, L)_{hex}$ direction and the $(H, 0, 0)_{hex}$ and $(0, K, 0)_{hex}$ vectors are subtended by 60° in the perpendicular (surface) plane. The units for H, K and L are $a^*=b^*=4\pi/\sqrt{3}a_{NN}$ and $c^*=2\pi/\sqrt{6}a_{NN}$, where a_{NN} is the nearest-neighbour distance in the crystal (a_{NN} = 2.775 Å). The detector slits were defined by selecting a region of interest which was a multiple of the pixel height/width (172 μm). Beam defining slits were 0.5 mm x 0.5 mm and the beam size at the sample was estimated to be 200 μm x 300 μm (vertical x horizontal).

6.2.1 Some remarks about stability

As previously discussed one of the most challenging aspects of making *in-situ* measurements of non-aqueous electrochemical systems is keeping the electrolyte dry. Initial coulometric titrations were used to check to water content of the solvent inside the glovebox but on the diffractometer cyclic voltammetry (CV) was the only way to assess the system's stability. Figs. 2(a) and 2(b) show CVs measured *in situ* for both systems. As the electrode is fully immersed in electrolyte the voltammograms contain

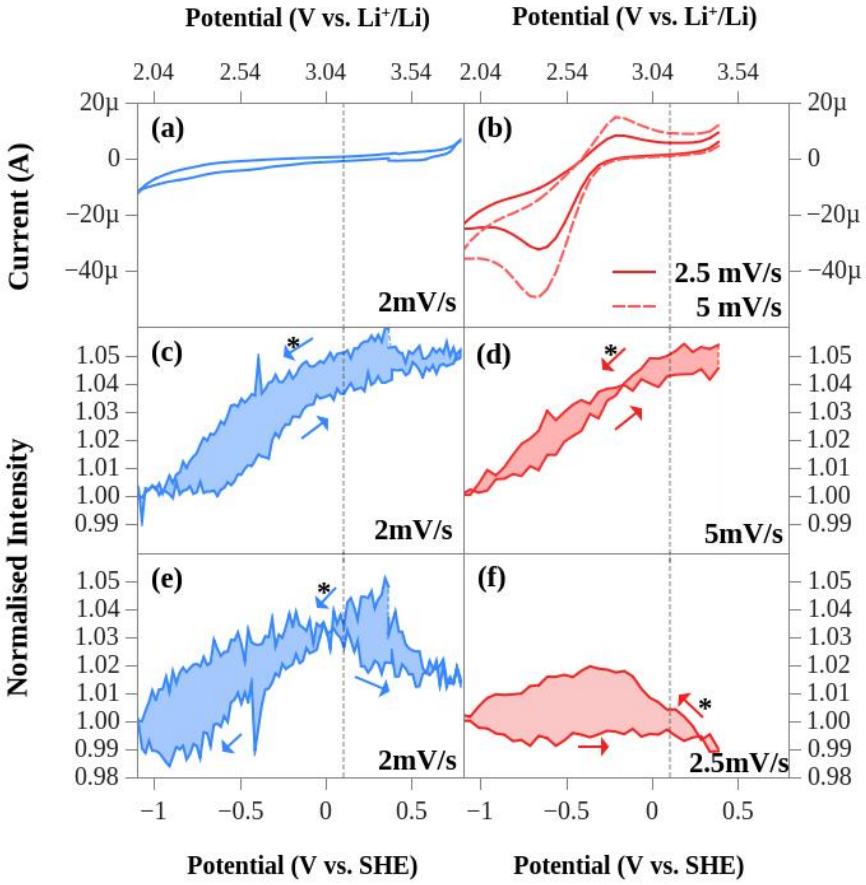

Figure 6.2: X-ray voltammetry (XRV) measurements. The left-hand side shown in blue corresponds to data measured in MeCN + 0.1 M $TBAClO_4$ whereas the right-hand side (red) corresponds to data measured in O_2-saturated MeCN + 0.1 M $TBAClO_4$. **(a)** and **(b)** are cyclic voltammograms measured at the same time as the X-ray measurements and include some contribution from the polycrystalline back and sides of the crystal. **(c)** and **(d)** show the XRV measured at (0, 1, 0.52) as a function of potential. **(e)** and **(f)** show the XRV measured at (0, 0, 1.52), an anti-Bragg position on the specular CTR. Sweep rates are indicated.

contributions from the polycrystalline back and sides of the crystal, the contacting Pt wire, and the (111) face under investigation. An absence of excess water can be inferred since additional features that can be seen in the presence of small amounts of water are not observed [109]. The potential range can also be extended much more negative than the potential where hydrogen evolution would occur and there were no changes with time in the voltammograms throughout the entire length of the experiment. Figure 6.2 (b) shows features (around -0.5 V) thought to be associated with the one electron reduction and oxidation of molecular oxygen, that is:

$$O_2 + e^- \rightleftharpoons O_2^- \qquad (6.1)$$

There are also no features to indicate the presence of water in Figure 2(b). The redox couple does however confirm success in pre-saturating the solution with O_2. With oxygen present the potential was kept below 0.4 V, to reduce the risk of oxidising the surface. The XRV in Figures 2(c) – 2(f) were repeatable and show that the behaviour of the system is fully reversible; the electrode for example is not roughening. The XRV measurements are discussed in more detail later on in the discussion on ordering in the electrolyte.

6.2.2 The Pt (111) electrode

It has long been known that well-ordered Pt(111)-(1 x 1) surfaces remain intact in aqueous solutions [119–121]. SXRD has also been used to show that there is a potential dependant relaxation of the top layer of atoms [72,122]. In order to gain detailed atomic-scale information on the surface structure of the electrode, crystal truncation rods (CTRs) along the specular (0, 0, L) and non-specular (1, 0, L) directions were measured at 0.4 V and 1.1 V. Specular and non-specular CTRs were modelled simultaneously. Specular

CTRs are also affected by vertical ordering in the electrolyte which will be discussed in the following section.

In contrast non-specular CTRs are only affected by structures commensurate to the Pt (111) electrode. Figs. 3(a) and 3(b) show the (1, 0, L) CTRs with and without the presence of oxygen. The solid line shows the fit to the data using a model with parameters: expansion (ε_i), root-mean-squared (rms) roughness (σ_i) and commensurate coverage (η_i). The coverage (θ) of each Pt layer was fixed at 1. The atomic form factor used to model Pt atoms included corrections for dispersion. Each data point was individually background subtracted by selecting appropriate regions of interest. Some data points are not included because the signal could not be separated from strong background features.

The bottom panels in Figure 3 show the ratio between the CTRs at 0.4 V and 1.1 V. Dividing the data highlights any changes between the two potentials and removes systematic errors, since this type of error will not change. The solid line is the ratio of the two models used to fit the CTR data. The CTRs were modelled independently and a good fit to the ratio of the data indicates any differences between the CTRs are well modelled. The parameters that gave the best fit are summarised in table 1. The possibility of commensurate ordering in the electrolyte was also considered but no evidence of any super structure during the experiment was found. UHV experiments have indicated both a 2x2 ordered phase and a disordered phase with a higher coverage are possible [123]. The phase present in our experiment is likely to be a disordered one due to the high coverage values that fits to specular data gave. The models that gave best fits to the data indicate that the electrode remains well ordered across the entire potential range studied, there is only a small change in the surface rms roughness.

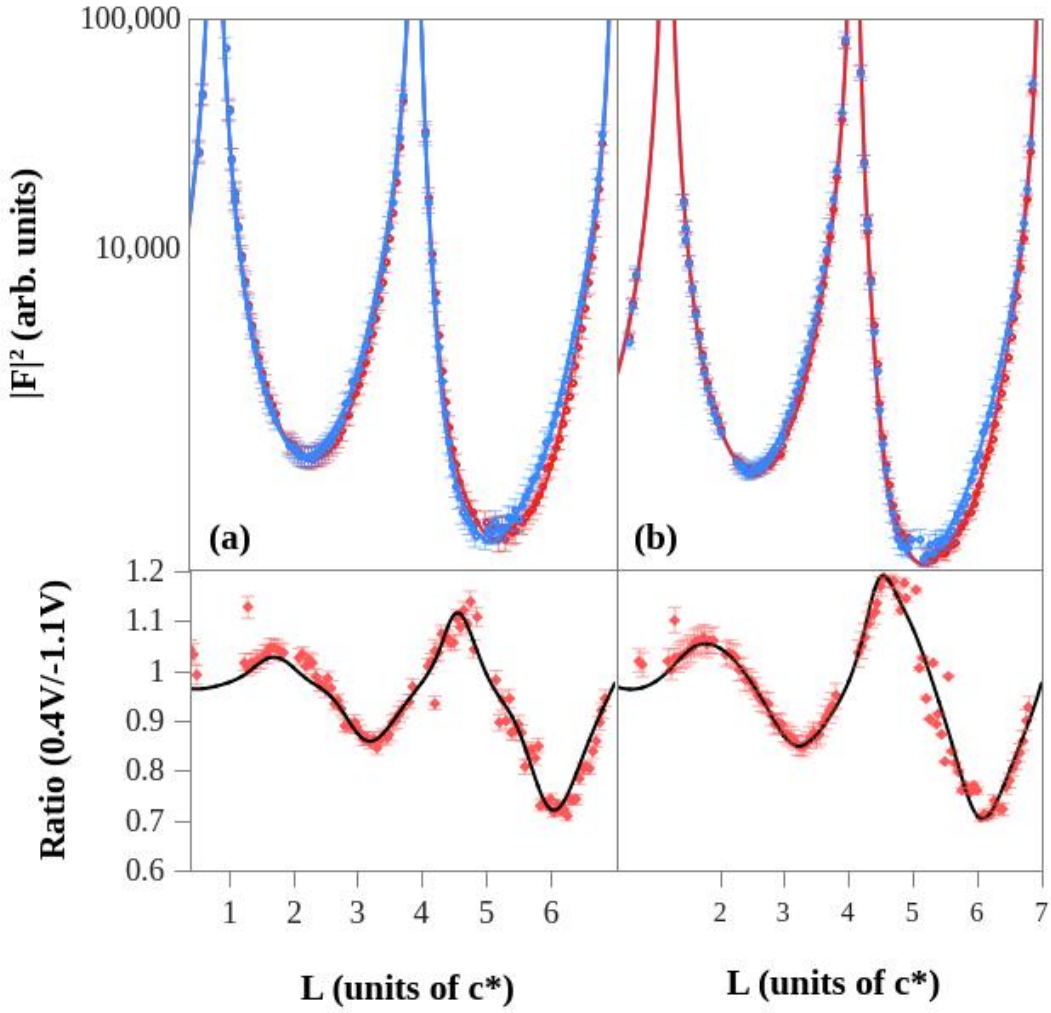

Figure 6.3. Fits to non-specular crystal truncation rods. Measured data is shown as circles with error bars and in the top panels corresponds to the background subtracted intensity after division by the monitor and various corrections for the diffraction geometry. A 6 % systematic error is assumed. Red symbols correspond to the intensities measured at 0.4 V whereas blue symbols represent the data measured at -1.1 V. The solid lines indicate our best fit to the data, where the parameters are given in table 1. The bottom panels show the data measured at the negative potential normalised to the data measured at the positive potential. **(a)** Data measured in the absence of oxygen. **(b)** Data measure with an oxygen saturated solution.

For the CTRs measured with oxygen, the model giving the best fit includes a small amount of in-plane disorder. The most significant change between the different fits is in the expansion (i.e. relaxation) of the topmost Pt layer. Conventionally it is thought that the forming of new metal-adsorbate bonds weakens the internal metal-metal bonds and cause relaxation. However, this is not always the case and charge transfer between the adsorbate and metal must be considered. Electronegative adsorbates will withdraw electrons from the metal and the ions will be less screened from each other so there is increased repulsion leading to expansion [124]. In contrast charge injection by electropositive adsorbates should increase screening and lead to a contraction. This picture is incomplete, the orbital character of electrons, anti-bonding effects, adsorbate polarity, and donor/acceptor contributions from both the metal and adsorbate need to be considered [125]. Full quantum chemical computations are required to be able to fully predict surface relaxation.

Observations of surface relaxation can however still provide useful insight, with a view to later verification through more detailed calculations. The intensity measured at (1 0 3.7) on the non-specular CTR is linearly proportional to surface expansion (see Figure. 3.8) and not affected by small changes in coverage or roughness. This allows intensity to be converted to expansion using two CTRs measured at each potential. Figure 4.2 shows XRV measured at (1 0 3.7) as a function of expansion. XRV not shown but measured at (1 0 4.3) was found to be the mirror image of that at (1 0 3.7). Interestingly expansions between 2 % and 3 % have been previously reported in aqueous media around 0 V (vs. RHE) and attributed to the adsorption of hydrogen [72,122]. In neither of the two systems measured do we see any such dramatic change around 0V, which is expected since the electrolyte is aprotic.

	Parameter	0.4V	-1.1V	0.4V	-1.1V
Metal Layers	ε_{34} (Å)	0.008(1)	0.006(1)	0.0086(7)	0.0082(8)
	ε_{23}(Å)	0.023(1)	0.024(1)	0.0227(9)	0.0248(9)
	ε_{12}(Å)	0.079(1)	0.095(2)	0.066(1)	0.086(1)
	σ_2(Å)	0.059(3)	0.036(6)	0.065(3)	0.047(4)
	σ_1(Å)	0.113(3)	0.103(3)	0.103(3)	0.095(3)
	η_1	1	1	0.955(6)	0.951(6)
Layer 1	θ	0.6(1)	0.90(9)	0.72(9)	0.90(9)
	d(Å)	2.4(1)	2.6(1)	2.77(7)	2.71(5)
	σ (Å)	0.15	0.15	0.15	0.15
Layer 2	θ	1.04(8)	0.75(8)	0.02(7)	0.14(8)
	d(Å)	3.23(4)	3.41(7)	4(2)	4.0(3)
	σ (Å)	0.15	0.15	0.15	0.15
Layer 3	θ			0.22(9)	0.25(9)
	d(Å)			4.9(2)	4.9(2)
	σ (Å)			0.15	0.15
Error Function	d(Å)	4.7(2)	5.0(2)	5.8(2)	5.8(2)
	σ (Å)	0.5	0.5	0.5	0.5
	χ^2_{red}	1.30	1.34	1.28	1.35
	R-factor	0.055	0.058	0.049	0.053

Table 6.1. Parameters giving best fits to the data. The parameters obtained in a least-squares fit to the experimental data measured along crystal truncation rods is presented. The left hand side (blue background) show the parameters giving the best fit to the data measured in the absence of oxygen. The parameters on the right hand side (red background) correspond to the parameters giving the best fit to the data measured when the electrolyte was saturated with oxygen. Numbers in italics correspond to parameters that were fixed during the fitting procedure. Errors are estimated from the diagonals of the covariance matrix.

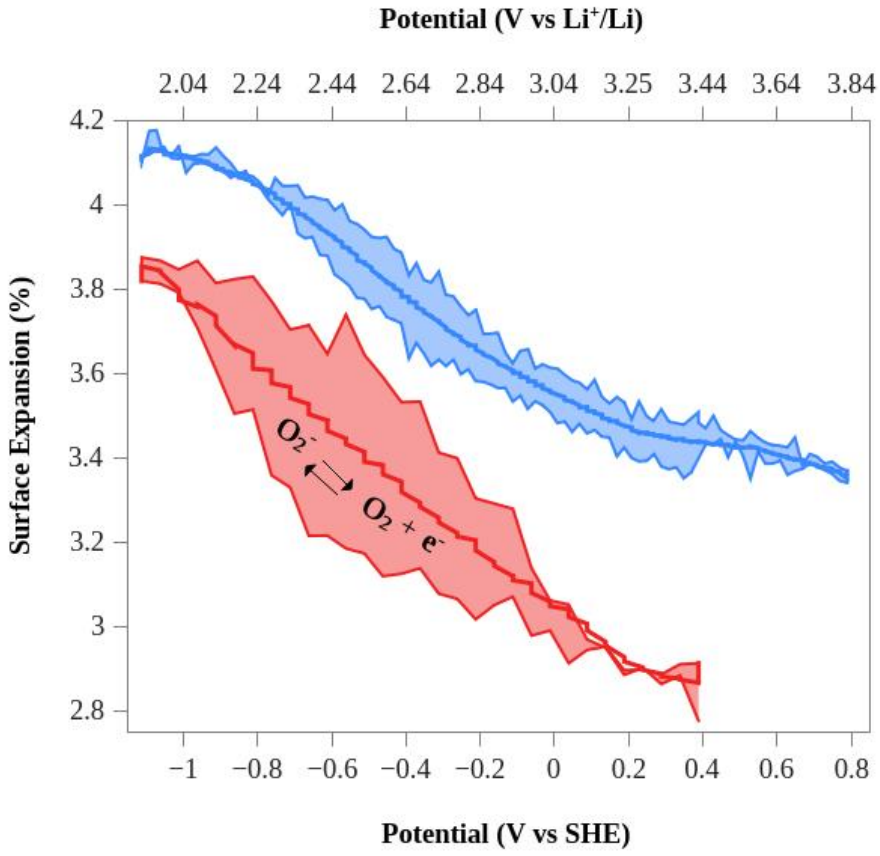

Figure 6.4. X-ray voltammetry showing surface expansion. The data was measured at the reciprocal space position (1 0 3.7) and then converted to surface expansion using parameters obtained from the fits of crystal truncation rods shown in Figure 6.3. The blue line corresponds to the expansion calculated from data measured in the absence of oxygen whereas the red line corresponds to data measured in the presence of oxygen. The shaded area is given as an indication of the amount of hysteresis. The solid central lines are a moving average of the nearest 20 data points (from both scan directions) and indicate the overall trend.

There has however been some controversy in attributing the cause of this expansion in aqueous solutions to either adsorption or the electric field. That such an expansion does not happen in aprotic electrolytes suggests hydrogen is in some way responsible for this change in aqueous media. With oxygen, the surface is less expanded across the entire

potential range, since oxygen is electronegative this is somewhat unexpected. Although perhaps not surprising, considering the above discussion and the possibility of adsorbate-adsorbate interactions. It may be less related to the adsorption of oxygen and more the dissociation of MeCN. The phenomena of relaxation is investigated in more detail in Chapter 7.

6.2.3 Electrolyte structure

Specular CTRs (also known as extended reflectivity) are only sensitive to ordering in the direction perpendicular to the surface and therefore are a measure of vertical electron density. The model used to fit the CTR data and to account for adsorbates and scattering from the bulk electrolyte is described in chapter 3 and illustrated in Figure 6.5(a). The atomic form factor for carbon was used for all adlayers in the model as nitrogen, carbon and oxygen all have similar atomic numbers. The rms roughness for each adlayer was fixed slightly above that of Pt at 0.15 Å. In order to account for scattering from the bulk electrolyte the model included an error function with width 0.5 Å and a maximum electron density equal to the bulk density of MeCN, placed at a height determined by the best fit to the data. Figure 6.5(b) shows how a vertical electron density profile relates to the various components of this model. Figure. 6.6 shows fits to the specular data for both systems measured. As with the non-specular CTRs the bottom panels show the ratio between the two potentials. Solid lines indicate the lines of best fit whose parameters are listed in table 1. The complexity of the model chosen (i.e. the number of adlayers included) was chosen based on whether there was any significant

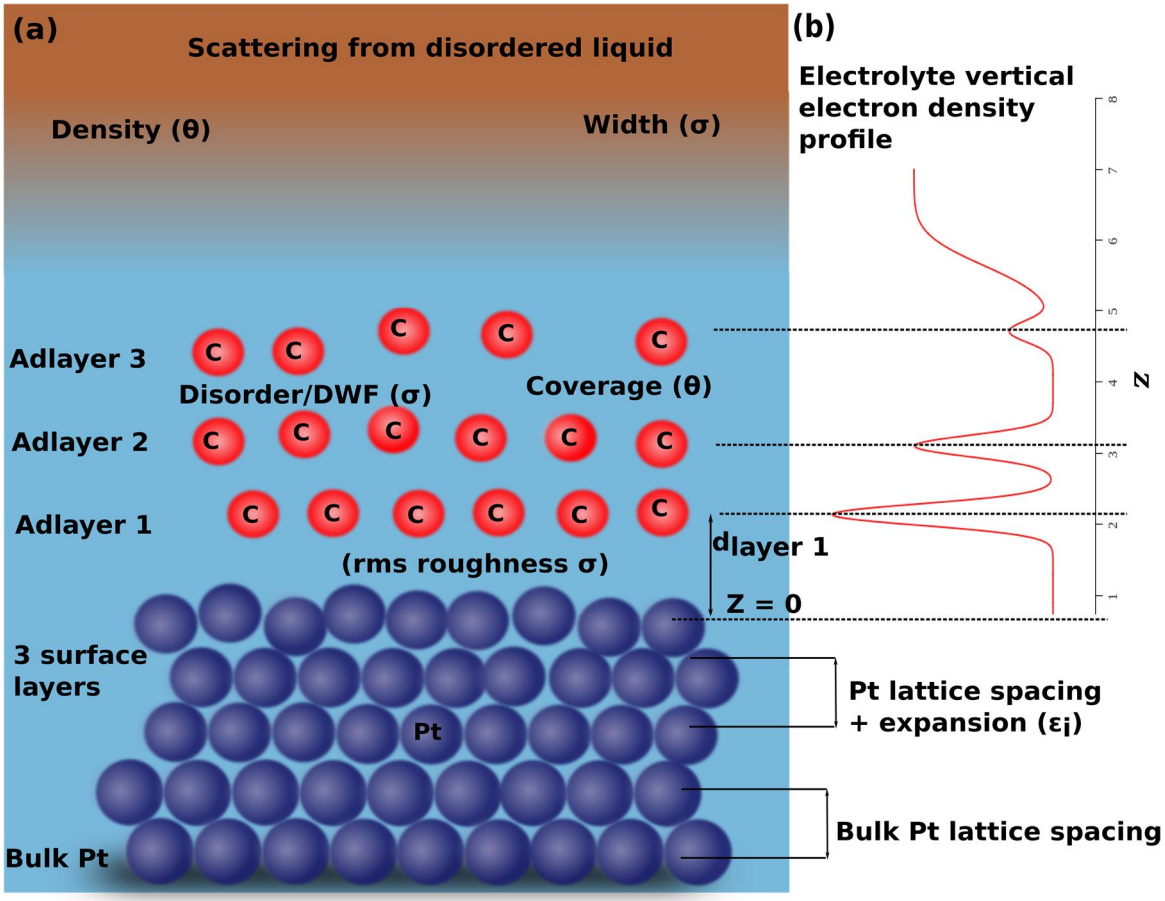

Figure 6.5. Illustration of the model used to fit the data. (a) This illustration indicates how the model comprises of the metal bulk and surface layers. Above the metal the model includes a number of adlayers, modelled with the form factor for carbon, and then an error function to account for scattering from the bulk electrolyte. (b) The graph shows how a vertical electron density map corresponds to various components in the model.

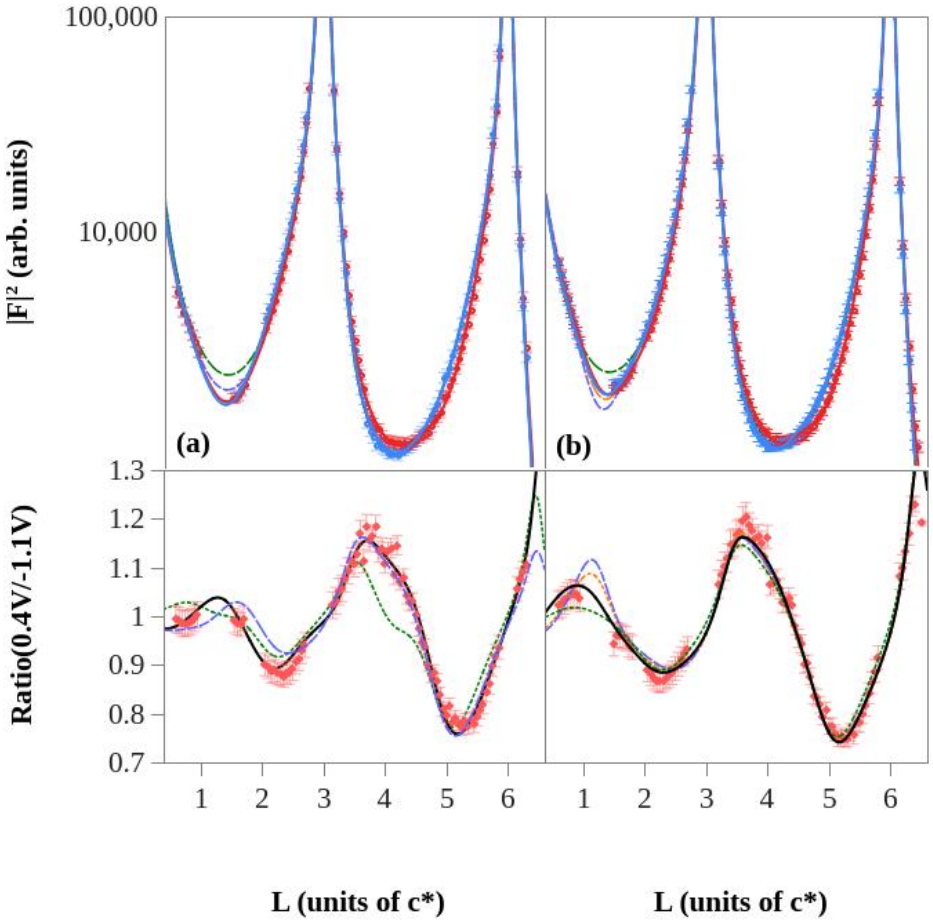

Figure 6.6. Fits to specular crystal truncation rods. **(a)** Best fit without oxygen. (**b)** Best fit with oxygen. In the top panels the blue symbols correspond to data measured at -1.1 V whereas those in red correspond to data measured at 0.4 V. The best fits to these dataare indicated with the solid red and blue lines. Error bars include an assumed 6 % systematic. The dashed lines show how an electrolyte model with less parameters impacted upon the fit for the data measured at -1.1 V. The green dashed lines indicates the best-fit when the electrolyte was not taken into consideration. The purple dashed lines when only one carbon layer and an error function where included. The orange dashed line indicates the best fit achieved when two carbon layers where included in the model. The bottom panels show the ratio of the data measured at 0.4 V with the data measured at -1.1 V.

reduction in the weighted mean squared deviation (reduced χ^2) between the data and the model. The dashed lines on the ratio plots indicate how well models with less parameters were able to account for differences in the CTRs at the two potentials measured. Figure 6.7 shows the laterally averaged vertical electron density profiles for each system at both potentials. The profiles include resolution broadening where electron density is plotted to simulate the finite experimental resolution where the electron density is plotted as a Gaussian function with an effective vibrational amplitude corresponding to the vibrational amplitude of the atom (σ) and a resolution determined width added in quadrature i.e. $u_{eff} = \sqrt{(u_{res}^2 + \sigma^2)}$ Where $u_{res} = 1.1/Q_{max,}$ and Q_{max} is the maximum momentum transfer in the measurement. The choice of u_{max} is discussed in [126] and is motivated by consideration of the Patterson function. The effective electron density is then given by $\rho_{eff}(z)=\tau\theta Z/[(2\pi)^2 u_{eff}]\exp[-0.5\times((z-z_0)/u_{eff})^2]$ where Z is atomic charge, θ the coverage, τ the inverse unit cell area, and z_o the position above the surface.. As the profiles are laterally averaged the possibility of contributions from molecules other than MeCN and O_2 exists. TBA cations however are thought to be only present in the outer diffuse region of the double layer [109] and the perchlorate anions are thought to to solvate MeCN but at more positive potentials than the measured CTRs [106,107].

In the absence of oxygen, Figure 6.7 (a), the best fit was with two layers of electron density. Their relative position to the electrode surface seems to swap with potential. This could be due to a potential induced change in orientation of MeCN at Pt(111) electrodes that has previously been described [107]. This is illustrated in the Figure inset. The XRV in Figure 6.2 (c) shows the variation of intensity with potential at a non-specular anti-Bragg position (0 1 0.52). Although the intensity at this position is a superposition of several Fourier components only atoms with an ordering commensurate

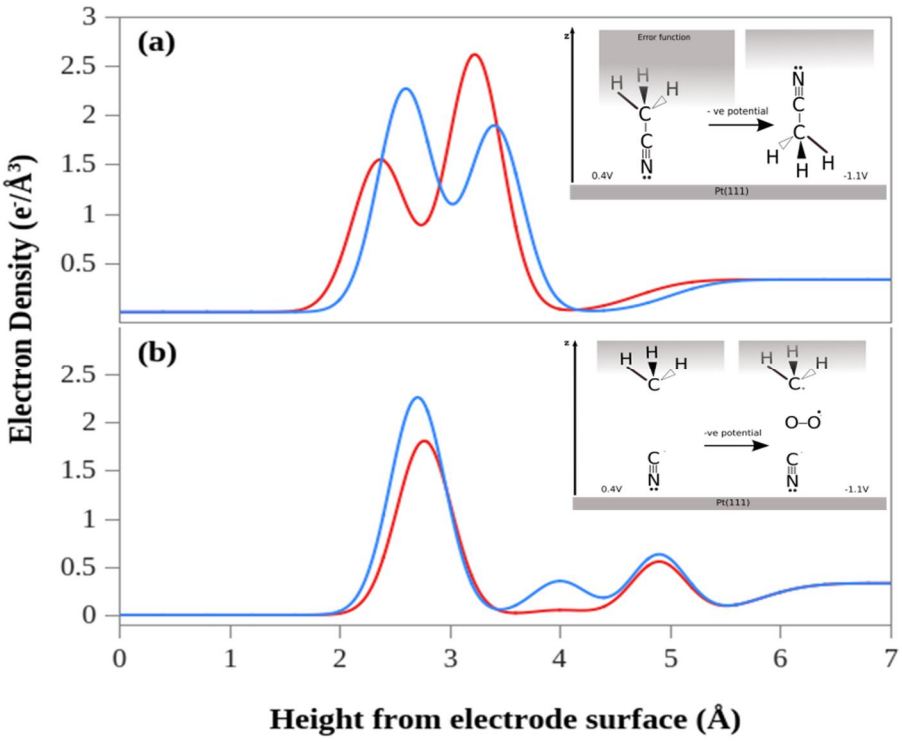

Figure 6.7. Electron density profiles**.** Idealised electron density profile corresponding to the best-fit structure given in table 1. The metal has been neglected to highlight features above the electrode surface. The red lines are calculated from the best-fit to the data measured at 0.4 V whereas the blue lines correspond to the data measured at 1.1 V. **(a)** shows the calculated profile from the data measured in the absence of oxygen whereas **(b)** corresponds to that measured when the solution was pre-saturated with oxygen. The insets are illustrations suggesting how this may relate to the arrangement of molecules at the electrode surface.

to the Pt electrode contribute. In contrast Figure 6.2 (e) shows XRV at (0 0 1.52), a specular position. At ~ 0 V the intensity at (0 0 1.52) decreases whereas it does not at the (0 1 0.52) position. Measurements at these two positions do show an asymmetry in the effect roughness has on intensity but this is not sufficient to account for the observed change. Instead calculations of CTRs show that reducing the spacing between the two adlayers results in a rapid decrease in intensity at (0 0 1.52). In the vertical plane this is exactly what any tilting of a molecule would look like. Furthermore there is an obvious hysteresis and the gradient on the negative sweep is also much steeper around this potential. Interestingly the pzc for acetonitrile/Pt (111) is estimated to be - 0.51 V vs ferrocene using differential capacitance [106]. On the SHE scale this puts the pzc at 0.11 V which is just after the onset of this feature on the measured XRV, this is indicated by the dashed lines on Figure 6.2. Another suggestion has been that MeCN is chemisorbed on its side through a hybridised C= bond at certain potentials [106]. If this were the case one would expect to see a more substantive change in layer spacing between the two potentials than is observed.

In the presence of oxygen our measurements indicate there is a different interfacial structure. The electron density profiles shown in fig 6.7 (b) has two layers which remain almost the same at both potentials. As the distance between these two layers is greater than any molecular bond inside acetonitrile this may be an indication that the molecule has dissociated into a cyanide and methyl group. Indeed this is known to happen on very rough Pt surfaces [104,105], perhaps the presence of oxygen somehow catalyses this reaction at the electrode surface. At the negative potential there is also an additional layer of electron density between these two layers that is probably some oxygen species such as superoxide. The XRV in Figure 6.2 (f) is very different from that in 6.2 (d). It is consistent with an adsorption process, where one would expect the intensity to increase

with adsorption and then with desorption to decrease. This is what happens in 6.2 (f) when the changes in the metal shown in 6.2 (d) are taken into consideration. This is illustrated in the inset of Figure 6.7 (b) but it must be acknowledged that in the presence of oxygen the actual reaction products may be more complicated.

6.3 Conclusions

In this chapter the experimental feasibility of performing *in-situ* surface X-ray diffraction at non-aqueous electrolyte/metal interfaces, measuring both specular and non-specular CTRs has been demonstrated. This is shown by the stability and reproducibility of both CV and XRV measurements as wells as the absence of voltammetric features associated with the presence of water. How measurements of surface relaxation can be related to charge transfer processes at electrode interfaces has been discussed and measurements made at much more negative potentials than were previously possible have been presented. It has been shown that in MeCN, an aprotic solvent, there is only a small gradual change in surface expansion. This is in contrast to many aqueous systems that show a 2-3% relaxation at negative potentials. By combining specular and non-specular CTRs, fits to the data have shown how the electrolyte structure close to the interface can be modelled. The results suggest in the absence of oxygen MeCN changes its orientation, around the pzc, whereas with oxygen MeCN is dissociated at the electrode surface. In the presence of oxygen there is also evidence of an adsorption process, indicating that the reduction of oxygen involves adsorbed surface species. The majority of polar solvents are thought to chemisorb on clean Pt surfaces and these absorbed layers are known to dramatically alter the electrodes performance. Therefore a thorough understanding of non-aqueous interfaces is important in the design of M-O_2 batteries as well as for many other areas where pre-treatment of the electrode maybe used to control solvent adsorption.

7 SURFACE RELAXATION AND ADSORPTION

7.1 Introduction

An understanding of the electronic interaction between adsorbed species and electrode surfaces is a crucial aspect of surface electrochemistry and corrosion science, as well as being important in the development of new catalysts. Some key questions that remain in achieving a fundamental understanding of interfacial phenomena at a molecular level are:

1) What is the structure of water and how does this influence electrocatalytic reactions?
2) What is the nature of bonding between metals and organic species?
3) What is the role of anions in the electrochemical double layer?

Water must play a key role in electrocatalytic reactions, for example, it is known to be chemisorbed at the electrode surface and to undergo a potential dependent reorientation around the potential of zero charge [127–129]. It has been suggested there are 3 species of water [130]: bulk like water, adsorbed water below the potential of zero total charge (pztc), and water that solvates anions above the pztc. In this sense the anions act as a supplier of water molecules. Anions can either enhance the water structure (kosmotropes) or disrupt it (chaotropes). Not surprisingly then anions are important for many reactions such as the oxygen reduction and hydrogen evolution reactions (ORR and HER), both important to fuel cells. The degree of specific adsorption of anions is thought to follow

the trend: $F^- < -ClO_4 < -SO_4 < Cl- < Br- < I-$ [131]. Generally anion adsorption has an adverse effect on the fuel cell reactions and so understanding these processes is important [132]. The blocking of sites, modification of adsorption energies for adjacent species, and the restructuring of the electrode surface are all thought to result from anion adsorption, in some instances. Traditionally $-ClO_4$ anions are not thought to be specifically adsorbed, however recent papers by Watanabe *et al* [133] on polycrystalline electrodes and by Attard [134] on single crystal electrodes controversially suggest otherwise. Acetonitrile (MeCN) is an interesting system in which to study adsorption processes as the electrode is 'modified' and undergoes what is known as reactive chemisorption, where the electrode is expected to have a different reactivity than the bare metal [110], MeCN also blocks sites for the adsorption of H and OH [135].

On the atomic scale, metals tend to minimise their surface energy through two kinds of atomic arrangements, relaxation and reconstruction. Relaxation is a small change in interlayer spacing at the surface, relative to the bulk spacing. In this Chapter relaxation is correlated with electrochemical adsorption processes to attempt to gain additional understanding about their nature.

7.2 Experimental details

The experimental details are as described in Chapter 4. The Pt (111) crystals were prepared via induction heating in an Ar / H_2 (5 %) atmosphere before being allowed to cool and transferred to the electrochemical cell covered by a drop of ultra-pure water. The concentration of MeCN was increased by pulling a higher concentration through the electrochemical cell via electrolyte tubing using a syringe. In this way the time necessary to prepare and realign the crystal was avoided. The Pt (111) surface was indexed using a hexagonal unit cell such that the surface normal lies along the $(0,0,l)_{hex}$ direction and the

$(h,0,0)_{hex}$ and $(0,k,0)_{hex}$ vectors lie subtended 60 ° in the perpendicular plane. The units for H, K and L are $a^*=b^*=4\pi/\sqrt{3}a_{NN}$ and $c^*=2\pi/\sqrt{6}a_{NN}$, where a_{NN} is the nearest-neighbour distance in the crystal (a_{NN} = 2.775 Å).

7.3 Results and discussion

7.3.1 The effect of acetonitrile concentration at the Pt (111) interface

To investigate the effect MeCN concentration has on the Pt/$HClO_4$ interface specular CTRs (extended reflectivity) were measured at a variety of concentrations. Non-specular CTRs were not measured due to experimental time constrains, however information about both the Pt (111) metal and the electrolyte can be obtained from this data. Figure 7.1 (a) shows best fits to the CTRs at 0.0 V whereas Figure 7.1 (b) shows the best fits at 0.85 V. The potentials were chosen to have the largest separation so that the greatest change could be observed, the negative limit (0.0 V) is in the hydrogen under potential deposition region (H_{upd}) whereas the positive limit (0.85 V) is after any anion adsorption. The parameters that gave the best fits are given in Table 7.1. Each data point in Figures 7.1 (a) and (b) has a 5 % assumed systematic error. The model to this data includes both the metal surface and the electrolyte. A single CTR on its own would be insufficient to justify the number of parameters given in table 7.1, even though the introduction of each parameter does bring about a reduction in reduced-χ^2. Instead whether the model had sufficient parameters or not was decided by inspection of the fits to data normalised by another CTR. The normalised data was however not included in any fitting and each of the rods were fit independently. The model selected included

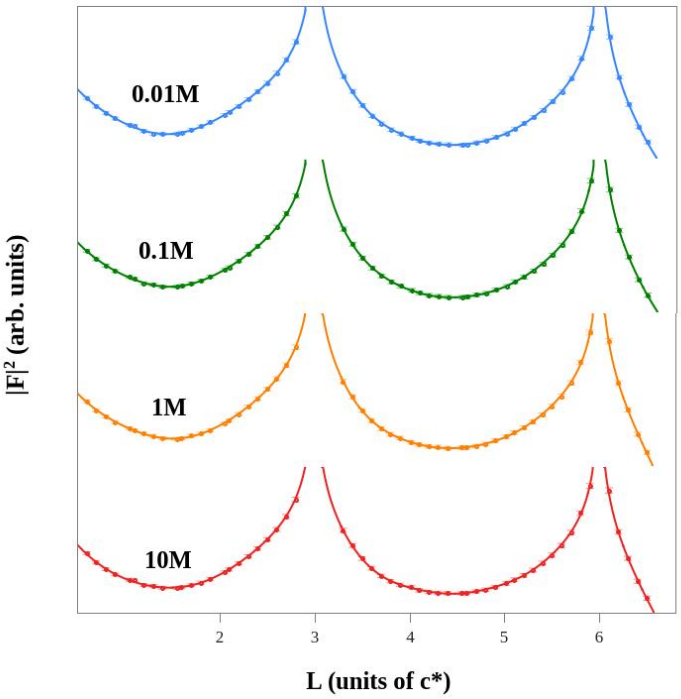

Figure 7.1 (a) Fits to crystal truncation rods measured at 0.85 V for Pt (111) / 0.1 M HClO4 + x M MeCN, where x is the concentration indicated on the figure.

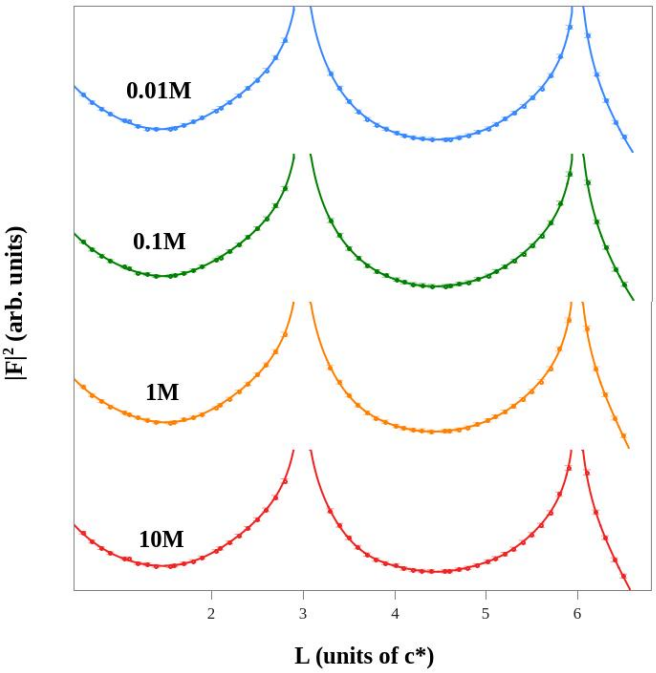

Figure 7.1 (a) Fits to crystal truncation rods measured at 0.85 V for Pt (111) / 0.1 M HClO4 + x M MeCN, where x is the concentration indicated on the figure.

		0.01M	0.1M	1M	50% (~10M)
0.0V	ε_{23} (Å)	0.012 ± 0.001	0.015 ± 0.002	0.017 ± 0.002	0.016±0.003
	ε_{12} (Å)	0.078 ± 0.001	0.082 ± 0.001	0.086 ± 0.002	0.089 ± 0.002
	σ_{Pt1} (Å^{-1})	0.089 ± 0.006	0.110 ± 0.009	0.12 ± 0.01	0.12 ± 0.01
	θo1	1.50 ± 0.05	1.60 ± 0.04	1.64 ± 0.05	1.83 ± 0.06
	d_{o1} (Å)	2.22 ± 0.01	2.15 ± 0.03	2.09 ± 0.03	2.06 ± 0.04
	θ_{o2}	0.53 ± 0.02	0.42 ± 0.04	0.36 ± 0.05	0.3 ± 0.1
	d_{o2} (Å)	3.33 ± 0.05	3.25 ± 0.06	3.23 ± 0.06	3.27 ± 0.08
	d_{err} (Å)	4.1 ± 0.1	3.7 ± 0.1	3.6 ± 0.1	3.2 ± 0.3
	r-χ^2	0.13	0.11	0.11	0.20
0.85V	ε_{23} (Å)	0.011 ± 0.002	0.012 ± 0.002	0.014 ± 0.002	0.013±0.002
	ε_{12} (Å)	0.062 ± 0.002	0.064 ± 0.002	0.073 ± 0.003	0.075 ± 0.003
	σ_{Pt1} (Å^{-1})	0.12 ± 0.01	0.13 ± 0.01	0.14 ± 0.01	0.14 ± 0.01
	θo1	1.30 ± 0.06	1.40 ± 0.06	1.57 ± 0.07	1.75 ± 0.08
	d_{o1} (Å)	2.12 ± 0.04	2.07 ± 0.04	2.01 ± 0.04	2.01 ± 0.04
	θ_{o2}	0.72 ± 0.06	0.63 ± 0.05	0.56 ± 0.06	0.60 ± 0.08
	d_{o2} (Å)	3.28 ± 0.04	3.31 ± 0.05	3.36 ± 0.06	3.38 ± 0.07
	d_{err} (Å)	4.1 ± 0.1	4.1 ± 0.1	4.0 ± 0.2	3.2 ± 0.3
	r-χ^2	0.14	0.18	0.22	0.28

Table 7.1 Parameters obtained from best fits to specular CTRs for different concentrations of MeCN.

expansion for the top two layers of the metal and roughness for the topmost layer; the electrolyte was modelled with two adlayers and an error function – as described in Chapters 3 and 6. The model's validity is supported by its consistency across all the concentrations of MeCN, where almost all the parameters follow a trend with concentration and the changes with potential are also found to be consistent across the different solutions. Figures 7.2 (a) and (b) show the ratio of the CTRs measured with 0.1 M, 1.0 M and 10 M concentrations of MeCN normalised to that measured with 0.01 M MeCN at both potentials. The solid lines show the ratios of the best fits to the CTRs. In Figure 7.3 the ratios of the best fit achieved for several alternate models to the data measured at 0 V are plotted for the 0.01 M / 10 M ratio. Clearly the ratios between the models that have no electrolyte or only one adlayer are in poor agreement with the measured data. The model with two adlayers (but no error function) is much better but consistently fails to model the ratio data at low L. The inclusion of an error function representing the transition to the electron density of the bulk electrolyte improves the fit to every data set and is therefore justified. Changes in the metal interface, both with potential and MeCN concentration, are dominated by expansion. There is a large change between the two potentials with the results indicating that the surface expansion is largest at 0 V. This potential dependant expansion is consistent with previous measurements at Pt (111) interfaces [122] that show an expansion of the surface at negative potentials. There is however a greater relaxation at both potentials than previously reported which increases with MeCN concentration. This suggests that the presence of MeCN close to the Pt (111) surface induces an outward expansion of the topmost Pt layers. Surface relaxation is discussed in more detail later (section 7.3.3). The fits to the data indicate that as the concentration of MeCN increases there is a slight increase in the out-of-plane Debye-Waller factor; this is also slightly larger at more positive potentials.

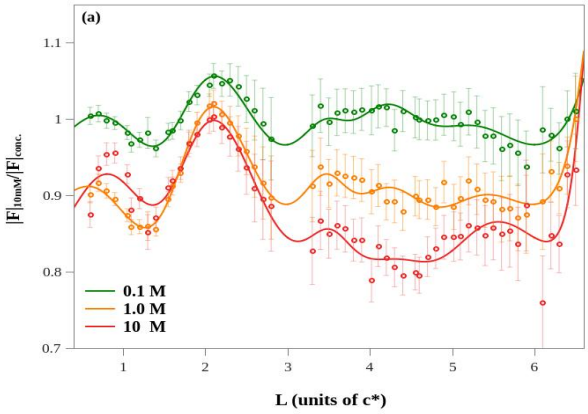

Figure 7.2 (a) Data measured at 0 V normalised to that in 10 mM concentration.

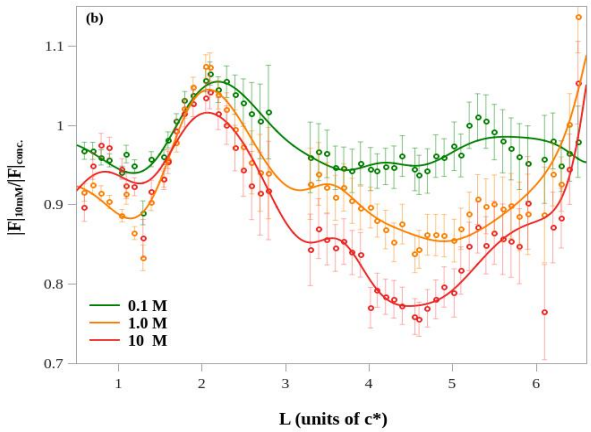

Figure 7.2 (b) Data measured at 0.85 V normalised to that in 10 mM concentration.

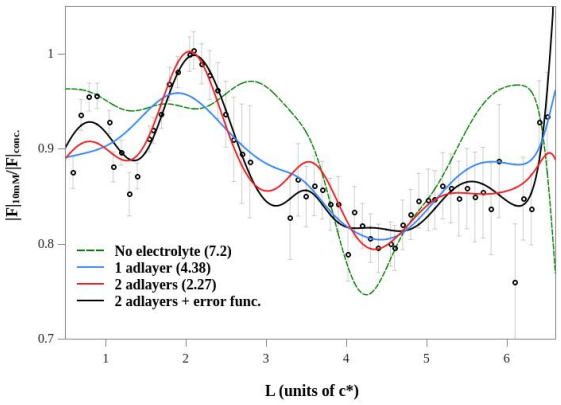

Figure 7.3. Data measured at 0 V in 10 M MeCN normalised to that measured in 10 mM.

The ratios of the best fits achieved with different models to the CTRs are shown.

Idealised vertical electron density plots showing how the concentration of MeCN affects the vertical structure of the electrolyte, close to the Pt (111) surface, are shown in Figures 7.4 (a) and (b) for 0 V and 0.85 V respectively. MeCN is known to chemisorb at Pt (111) electrodes therefore it seems reasonable to suggest that the first adlayer, which increases in coverage with the concentration of MeCN, corresponds to adsorbed MeCN (or at least part of that molecule). The best fits to the data also suggests that the width of the double layer region decreases with MeCN concentration. Both this decrease in double layer width and the increase in coverage of MeCN with MeCN concentration are in agreement with previous voltammetric measurements [136]. It also expected that adsorbed water will contribute to the electron density (and hence scattering) of this layer. The coverage of the second adlayer decreases with MeCN concentration which suggests a significant water/OH contribution. The coverage of the second adlayer is greatest at 0.85 V which is likely due to the presence of perchlorate anions in the Outer Helmholtz Plane (OHP).

These results represent a molecular scale measurement of the electrochemical double layer in the vertical plane; the first adlayer being the Inner Helmholtz Plane (IHP) and the second being the OHP. Caution is however advised as individual species cannot be distinguished and the structure obtained is model dependant. One can never discount the possibility that an alternate model would fit the data better.

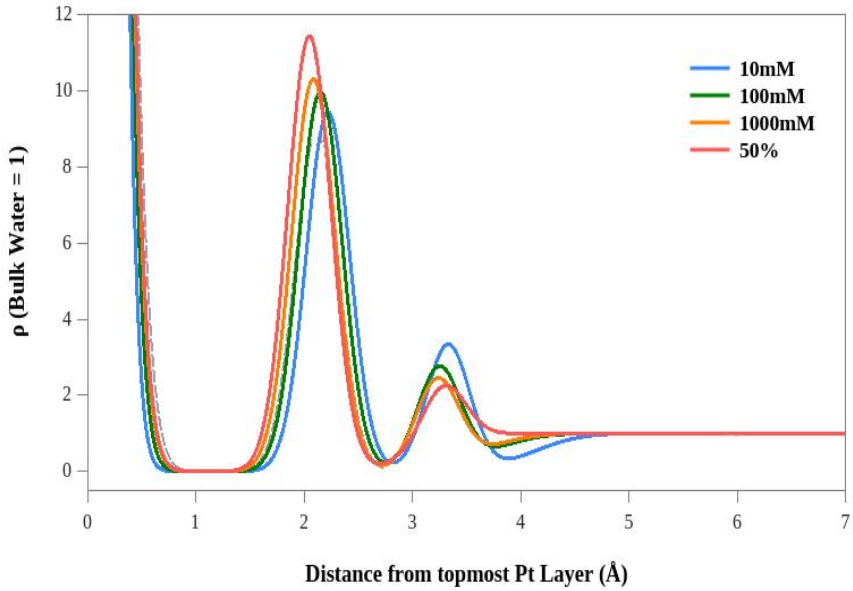

Figure 7.4 (a). Idealised electron density profile created using best fit parameters at 0 V. Normalised to the bulk density of water. Pt surface is at 0 Å.

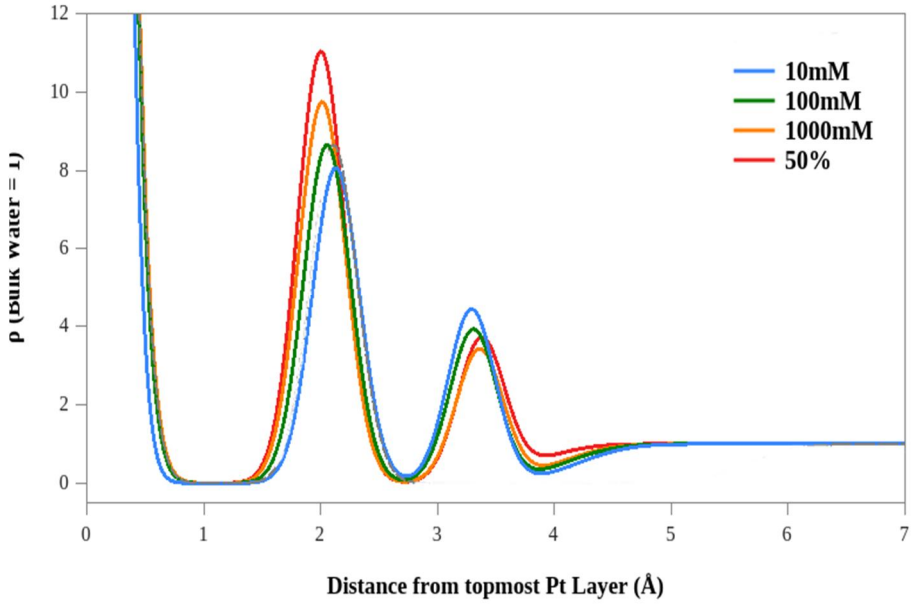

Figure 7.4 (b) Idealised electron density profile created using best fit parameters at 0.85 V. Normalised to the bulk density of water. Pt surface is at 0 Å.

7.3.2 Fits to CTRs with different anions

In this section CTR data for the Pt (111) electrode in 0.1 M concentrations of $HClO_4$, H_2SO4, and KOH are presented. Figures 7.5 – 7.7 show voltammetry from the literature for all three systems. In common, they all have an increased in current around 0 V corresponding to the adsorption of hydrogen. At the positive limit (where shown) above 1 V the current increases due to oxide formation. Both $HClO_4$ and H_2SO4 shown a double set of peaks between these potentials attributed to anion adsorption. Figure 7.8 shows a cyclic voltammogram measured during an *in-situ* SXRD experiment with 0.1 M $HClO_4$ and a Pt (111) working electrode. The back and sides of the crystal, as well as a polycrystalline connecting wire, were exposed to the electrolyte so the measurement is expected to be more like the of polycrystalline Pt. Careful voltammetry of this system can be found in ref [130]. There are essentially three potential regions. Current measured below 0.5 V is due to the adsorption/desorption of hydrogen. A central region where the current is only due to capacitive charging of the double layer; and then currents above ~0.65 V assigned to OH adsorption. OH adsorption leads to two features, a broad feature labelled OH_B and a sharp current peak OH_s [130]. The potential of each of these features varies differently in the presence of chloride ions. OH_B is shifted to lower potentials whereas OHs is shifted to higher potentials (and disappears altogether with higher concentrations). The OHs feature (not seen in Figure 7.8) has been attributed to chloride contamination [137,138] however this remains controversial. It has also been suggested that the feature is due to a change in the interaction between anions and an ice-like water structure based on how small additions of bisulphate and chloride ions affect voltammetric measurements[130].

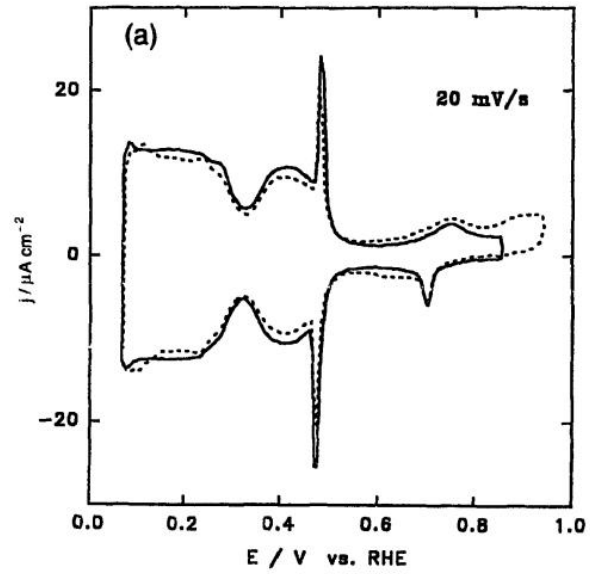

Figure 7.5. Cyclic Voltammetry of the Pt (111)/H_2SO_4 system measured at 20 mV/s. The solid and dotted lines are measurements of different systems to indicate the level of variation between experiments. Reprinted from reference [139] with permission from Elsevier.

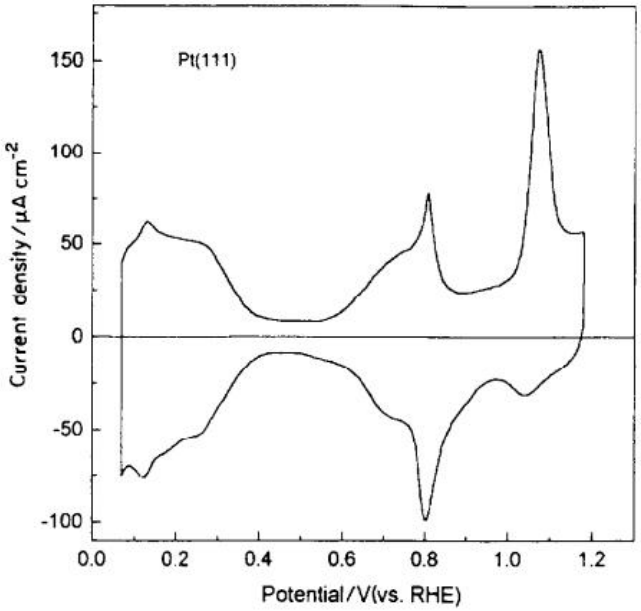

Figure 7.6. Cyclic Voltammetry of the Pt (111)/$HClO_4$ system measured at at 50 mV/s. Reprinted from reference [129] with permission from Elsevier.

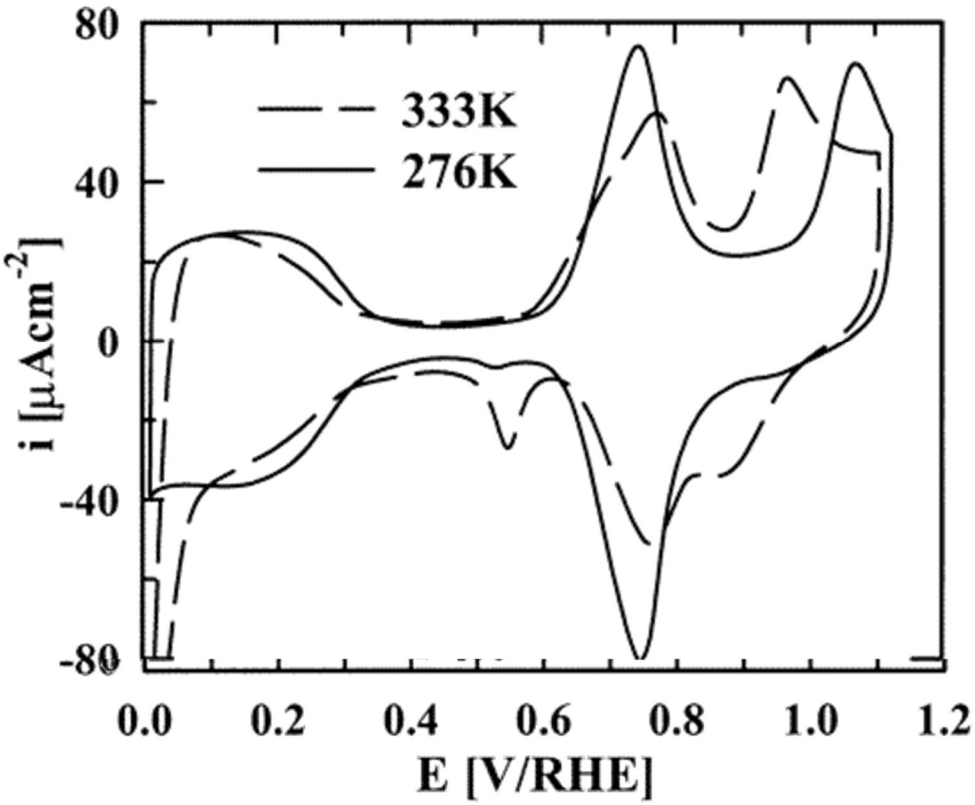

Figure 7.7. Cyclic voltammetry of the Pt (111) / KOH measured at 50 mV/s. Solid line measured at 276 K and the dashed line at 333 K Adapted with permission from [140] The Journal of Physical Chemistry B 2001 105 (48), 12082-12086. Copyright 2001 American Chemical Society.

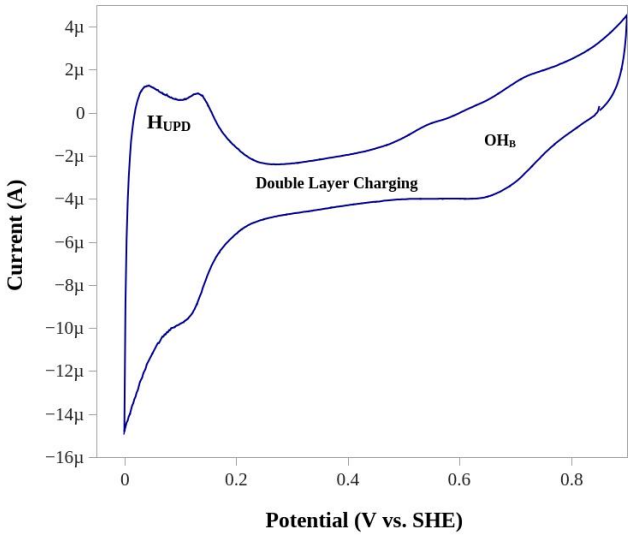

Fig 7.8 Cyclic Voltammetry of Pt / 0.1 M $HClO_4$ measured *in situ* during an SXRD experiment. Label are the regions of hydrogen upd, the double layer region and the supposed onset of OH adsorption. The sweep rate was 5 mV/s.

The OH_B feature is assumed to be the water state equivalent to anion adsorption.

In Figure 7.9 (a) fits to CTRs of the Pt (111) / 0.1 M $HClO_4$ interface are shown. The CTRs were measured at 0.0 V and 0.72 V. A small improvement to the fit was gained by modelling an electrolyte but this was not statistically significant enough to warrant the inclusion of the extra parameters, therefore the fits presented only model the metal electrode. The parameters that gave the best fit are shown in table 7.2. In Figure 7.9 (b) the ratio between the data measured at 0 V and 0.72 V is presented, from which it is clear that the best fits to the CTRs do a reasonable job of modelling any change between the potentials (which is dominated by surface relaxation).

The CTRs measured in H_2SO_4 and KOH electrolytes were only available at 0 V, which means that ratios are not available. However, relaxation seems to dominate changes to CTRs and this does not seem to differ between different fits to the data using different

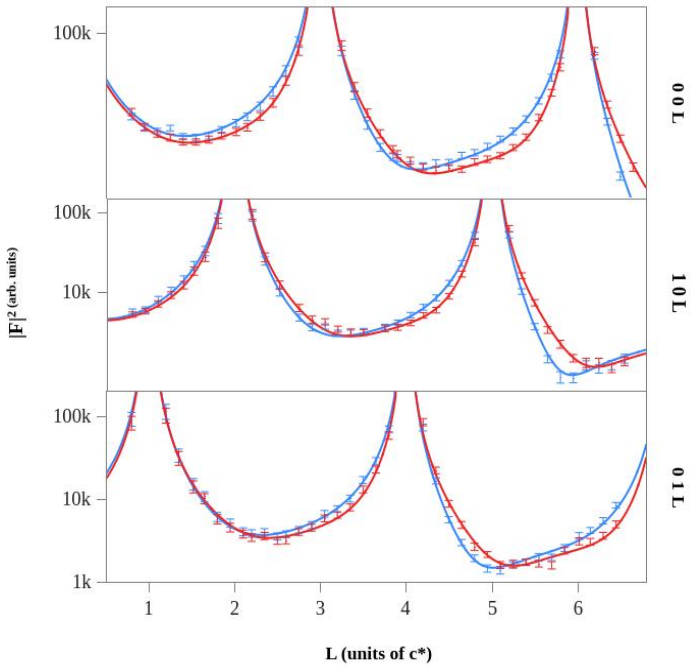

Figure 7.9 (a). Fits to CTRs measured at the Pt (111) / 0.1 M HClO4 interface. 00l, 10L and 01L CTRs were all fit simultaneously. The two potentials measured at 0.0 V and 0.9 V are shown in blue and red respectivelty.

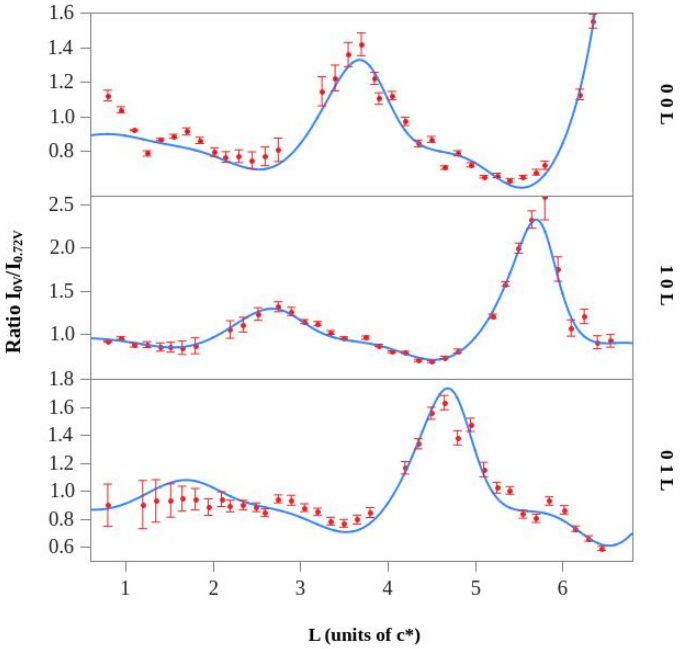

Figure 7.9 (b). Data at 0 V normalised to that at 0.72 V for three different CTRs.

	0.00 V	0.72 V
ε_{12}(Å)	0.058(2)	0.014(1)
σ_2(Å)	0.062(5)	0.044(7)
σ_1(Å)	0.094(5)	0.071(6)
χ^2_{red}	1.17 (1.03)	0.90 (1.00)
R-Factor	0.083	0.074

Table 7.2: Parameters giving best fits to $HClO_4$ data

	KOH (0.0 V)	H_2SO_4 (0.0 V)
ε_{21}(Å)	0.005(1)	0.008(3)
ε_{12}(Å)	0.058(1)	0.061(3)
σ_2(Å)	0.070(5)	0.04(1)
σ_1(Å)	0.100(6)	0.07(1)
χ^2_{red}	0.44	2.15
R-Factor	0.058	0.11

Table 7.3: Parameters giving the best fits to KOH and H_2SO_4 CTR data at 0 V.

Models. Fits to just one CTR are still useful for the exploring surface relaxation. Figure 7.10 shows the best fits to CTRs measured at 0 V for Pt (111) / 0.1 M H_2SO_4 and Figure 7.11 shows the equivalent for Pt (111) / 0.1 KOH. As with the previous data the fits were not improved significantly enough to warrant the inclusion of parameters to describe ordering in the electrolyte. The fit to the specular CTR measured in H_2SO_4 have a comparatively high x^2 value, the inclusion of an electrolyte model did improve the reduced-χ^2 value to around 1.5 but this is not sufficient to justify the increase in model complexity. It is interesting to note that relaxation calculated from the CTRs measured at 0 V in H_2SO_4, KOH and $HClO_4$ electrolytes at 0 V are the same within experimental error, in agreement with previous reports [72,122,141].

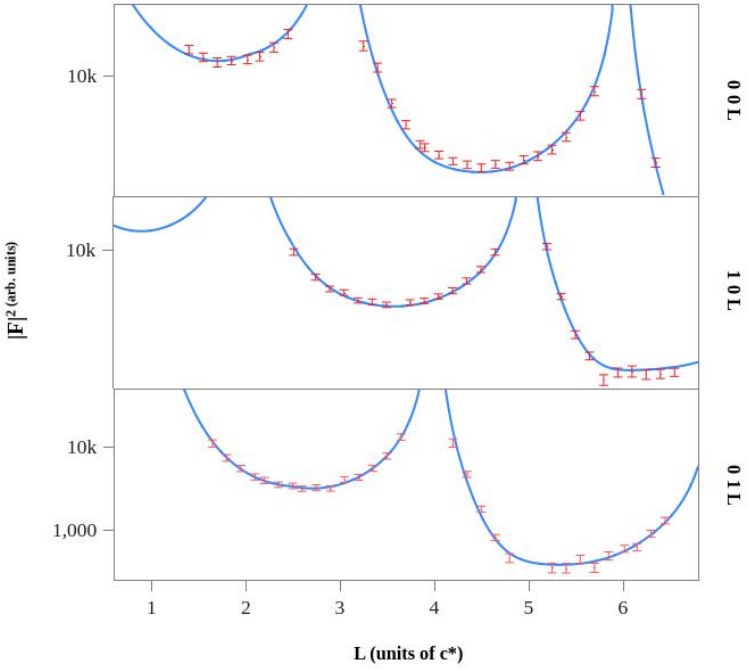

Figure 7.10: Best fits to CTRs measured at the Pt (111) / 0.1 M H_2SO_4 interface. 00l, 10L and 01L CTRs were all fit simultaneously

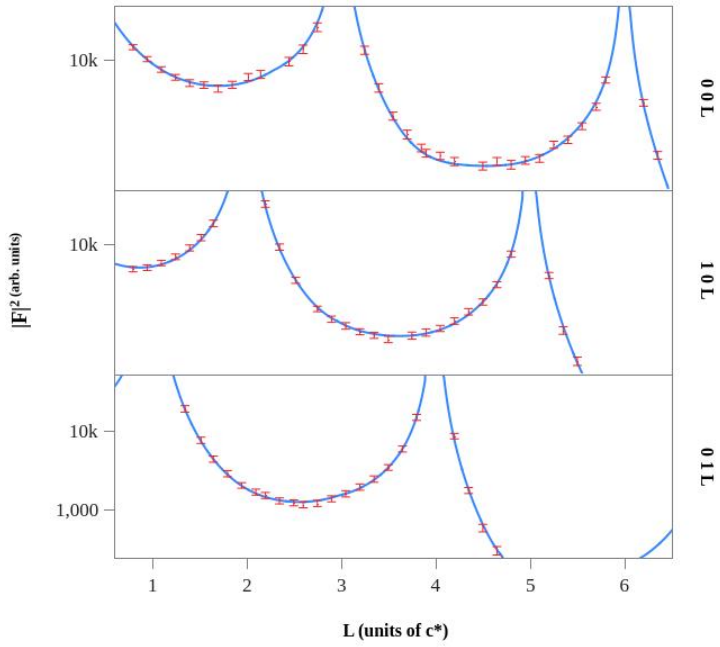

Figure 7.11: Best fits to CTRs measured at the Pt (111) / 0.1 M KOH interface. 00l, 10L and 01L CTRs were all fit simultaneously

7.3.3 Surface Relaxation

The previous two sections have presented fits to CTRs for a variety of electrolytes; the aim now is to put all this together and correlate changes in relaxation to electrochemical phenomena. Firstly, in the previous chapter the relaxation from two CTRs was used to convert measured intensity in X-ray voltammetry at (1 0 3.7) in reciprocal space to surface expansion for the non-aqueous MeCN / Pt (111) interface. The same process has been used for the data presented in this chapter and is shown in Figures 7.12 (a) and 7.12 (b). Where only one CTR was available, the intensity of a second CTR was simulated to enable to enable the linear dependence of intensity at (1 0 3.7) on surface expansion to be calculated. This of course assumes that any changes in roughness are minimal and the intensity around the Bragg peaks varies symmetrically. In Figure 7.12 (a) relaxation of the topmost Pt layer is shown for all the concentrations of MeCN investigated. Also plotted on the same scale is the expansion of Pt (111) in non-aqueous MeCN electrolyte from the previous chapter. The most notable difference between the aqueous and non-aqueous systems is a sharp increase in outward expansion around 0.35 V. This is a potential that has previously been identified as a potential of zero charge [129] and marks the onset of hydrogen adsorption [142]. It is thought that negative of this value water molecules at the electrode are oriented with hydrogen atoms towards the electrode, whereas above it the oxygen atoms point towards the electrode [128,129,143]. The fact that such a dramatic change does not occur in non-aqueous (aprotic) electrolytes supports the notion that expansion of the Pt (111) surface at negative potentials is due to the adsorption of hydrogen species [122,144]. Hydrogen adsorption is only thought to be partially blocked by the presence of acetonitrile [106], but the fact that the magnitude of expansion does not appear to reduce with increasing MeCN concentration suggests this

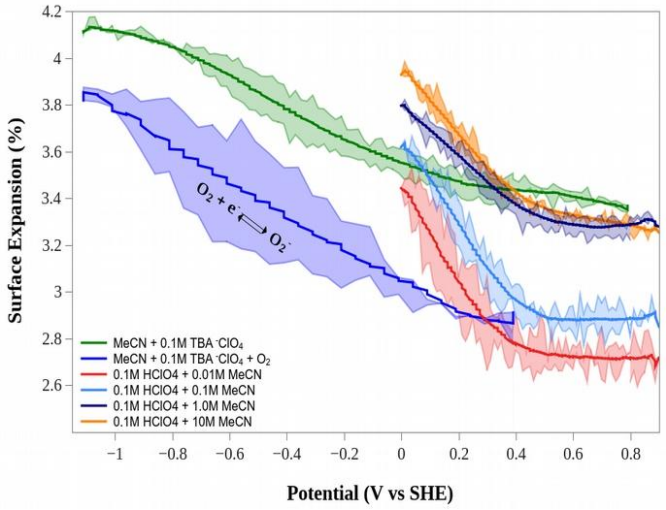

Figure 7.12 (a) X-ray voltammetry measured at (1 0 3.7) showing surface expansion for various MeCN containing electroltytes. Surface expansion is given as % of the bulk spacing using fits to two CTRs at different potentials, where a linear correlation between expansion and intensity at (1 0 3.7) is assumed. This is vaild when changes in surface roughness are small. The potential is given agaisnt SHE as the RHE scale can not be used for non-aqueous electrolytes.

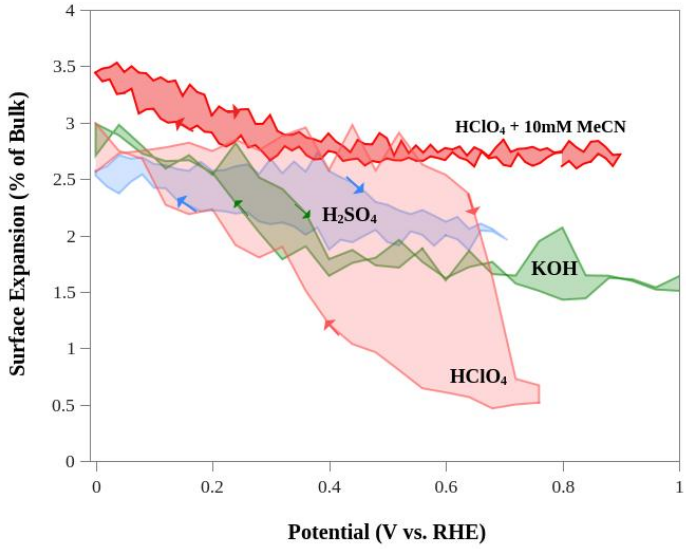

Figure 7.12 (b) X-ray voltammetry showing surface expansion for various electroltytes, the potential is given against RHE so that the potentials can be compared with hydrogren adsorption being at 0 V in each case.

cannot by due to hydrogen adsorption. It is interesting that there appears to be a baseline surface expansion linked to MeCN coverage (~ 3 % with 10 mM). In contrast the Pt (111) surface in the presence of CO remains ~ 4 % expanded up until 0.8 V, the onset of CO oxidation [72]. Wieckowski has proposed that the adsorption of organic molecules at platinum electrodes can be classified intro three groups [145]. Acetonitrile was assumed to be in a group of molecules with delocalised π orbitals that form complexes with the Pt surface, the overlapping of the π orbitals with the Pt d orbitals allows for the displacement of chemisorbed water. The interaction of acetonitrile with Pt however must also involve water species as the reactive chemisoption of MeCN only takes place in the presence of water [110].

Figure 7.9 (b) shows the relaxation of the Pt surface as a function of potential for all of the aqueous electrolytes measured. In KOH relaxation proceeds similarly to that of MeCN, there is a decrease in expansion around 0.4 V, thought to be due to desorption of hydrogen and presence of hydroxyl species at the surface. In contrast the surface remains expanded in both H_2SO_4 and $HClO_4$ until the adsorption of $^{-}SO_4$ and $^{-}ClO_4$ anions at around 0.42 V and 0.65 V. These potentials are in good agreement with the butterfly peaks associated with sulphate adsorption for H_2SO_4 electrolytes and the broad reversible OH_B feature in for perchlorate electrolytes. The fact that the surface remains expanded up until an adsorption processes (of an anion or OH species), even into the double layer region in the case of $HClO_4$, suggests that expansion cannot be just hydrogen adsorption. One possibility is that the relaxation of the surface is an electronic screening effect caused by an ordered water layer, when adsorption happens this is disrupted.

7.4 Summary

In this chapter fits to CTRs measured *in-situ* with a variety of electrolytes have been combined with XRV to study relaxation at the Pt (111) interface. Several interesting questions regarding the relationship between surface relaxation and adsorption have been raised. The data suggests that relaxation of the surface at negative potentials is not due to the adsorption of hydrogen as had been previously thought. It is suggested that the real situation is more complex involving the adsorption of water species. It is expected that the combination of relaxation measurements with theoretical modelling would provide a significant insight into adsorption processes at electrodes. Extended reflectivity measurements of the aqueous MeCN / Pt (111) interface as a function of concentration have also been presented, these provide a molecular scale view of the electrochemical double layer. The covering the electrode with MeCN and hence the blocking of anion adsorption also provides further information about surface relaxation effects.

8 CONCLUSIONS

In this thesis the powerful technique of *in-situ* surface X-ray diffraction has been used to explore several electrochemical systems of technological importance. It has been shown how the adsorption of carbon monoxide can alter the surface structure of gold electrodes in alkaline electrolytes which may ultimately explain why CO promotes methanol oxidation. The surface reconstruction of Au (111) electrodes is seen as being dynamic, responding to both changes in potential and adsorption. The presence of CO seems to 'pin' the reconstruction as well as partially lift it. The results re-enforce the need for large scale theoretical modelling capable of accounting for the entire reconstructed unit cell as well as the impact of step-edges, kinks and dislocations. The technique of SXRD has been extended to the study of non-aqueous solvents, an important feature of many future battery designs. MeCN appears to undergo a potential dependant reorientation in the absence of molecular oxygen but this does not occur when oxygen is present. It is suggested that this is due to the dissociation of MeCN molecules at the electrode surface. This may have implications in the choice of electrolytes used in future energy technologies such as Li-O_2 batteries. The absence of hydrogen and the wider potential window accessible in non-aqueous systems has allowed the relationship between electric field and surface relaxation to be studied. Surface X-ray diffraction has been used explore the effect of concentration at the Pt (111) /$MeCN_{(aq)}$ interface, giving molecular scale information about the double layer's structure. Measurements of surface relaxation in several different electrolytes have been presented and used to explore the

relationship between adsorption and surface relaxation. It is hoped that in the future SXRD measurements of an electrodes surface relaxation will provide fundamental information about the nature of the adsorbate-substrate interactions.

There however remains much to be done in the application of surface X-ray diffraction in studying the electrochemical interface. The implementation of advanced statistical techniques based on Bayesian analysis will allow better selection of models, and perhaps when combined with phase retrieval methods more accurate determination of electrolyte structures. The use of 2d detectors is still in its infancy but it seems their use is set to expand, creating more detailed maps of reciprocal space with better accuracy than before. New sample environments and cell designs will allow ever more realistic systems to be investigated with increasing complexity. New techniques such as high energy surface X-ray diffraction allow whole CTRs to be measured in one go providing greater temporal resolution, which may be improved further with the introduction of 4^{th} generation X-ray free electron lasers. Much remains to be done with resonant techniques, which offer the prospect of chemical sensitivity that can only be achieved currently through spectroscopy techniques such as FTIR and RAMAN. And ultimately results from surface X-ray diffraction will need better integration with other techniques and spectroscopies as well as large scale theoretical modelling.

9 REFERENCES

[1] H.E. Hoster, H.A. Gasteiger, Ex-situ surface preparation and analysis: transfer between UHV and electrochemical Cell, in: Handb. Fuel Cells, John Wiley & Sons, Ltd, 2010.

[2] M. El-Jawad, J.-L. Chemin, B. Gilles, F. Maillard, A portable transfer chamber for electrochemical measurements on electrodes prepared in ultra-high vacuum, Rev. Sci. Instrum. 84 (2013) 64101. doi:10.1063/1.4809936.

[3] P.M. Kolb, D.L. Rath, R. Wille, W.N. Hansen, An ESCA Study on the Electrochemical Double Layer of Emersed Electrodes, Berichte Bunsenges. Für Phys. Chem. 87 (1983) 1108–1113. doi:10.1002/bbpc.19830871206.

[4] E.R. Kötz, H. Neff, K. Müller, A UPS, XPS and work function study of emersed silver, platinum and gold electrodes, J. Electroanal. Chem. Interfacial Electrochem. 215 (1986) 331–344. doi:10.1016/0022-0728(86)87026-7.

[5] S. Trasatti, Surface science and electrochemistry: concepts and problems, Surf. Sci. 335 (1995) 1–9. doi:10.1016/0039-6028(95)00446-7.

[6] I.K. Robinson, D.J. Tweet, Surface X-ray diffraction, Rep. Prog. Phys. 55 (1992) 599–651. doi:10.1088/0034-4885/55/5/002.

[7] P.A. Fenter, X-ray Reflectivity as a Probe of Mineral-Fluid Interfaces: A User Guide, Rev. Mineral. Geochem. 49 (2002) 149–221. doi:10.2138/gsrmg.49.1.149.

[8] R. Feidenhans'l, Surface structure determination by X-ray diffraction, Surf. Sci. Rep. 10 (1989) 105–188. doi:10.1016/0167-5729(89)90002-2.

[9] S.R. Andrews, R.A. Cowley, Scattering of X-rays from crystal surfaces, J. Phys. C Solid State Phys. 18 (1985) 6427–6439. doi:10.1088/0022-3719/18/35/008.

[10] P. Rodriguez, Y. Kwon, M.T.M. Koper, The promoting effect of adsorbed carbon monoxide on the oxidation of alcohols on a gold catalyst, Nat. Chem. 4 (2012) 177–182. doi:10.1038/nchem.1221.

[11] C.O. Laoire, S. Mukerjee, K.M. Abraham, E.J. Plichta, M.A. Hendrickson, Influence of Nonaqueous Solvents on the Electrochemistry of Oxygen in the Rechargeable Lithium−Air Battery, J. Phys. Chem. C. 114 (2010) 9178–9186. doi:10.1021/jp102019y.

[12] C.O. Laoire, S. Mukerjee, K.M. Abraham, E.J. Plichta, M.A. Hendrickson, Elucidating the Mechanism of Oxygen Reduction for Lithium-Air Battery Applications, J. Phys. Chem. C. 113 (2009) 20127–20134. doi:10.1021/jp908090s.

[13] P.G. Bruce, S.A. Freunberger, L.J. Hardwick, J.-M. Tarascon, Li-O2 and Li-S batteries with high energy storage, Nat. Mater. 11 (2012) 19–29. doi:10.1038/nmat3191.

[14] G. Girishkumar, B. McCloskey, A.C. Luntz, S. Swanson, W. Wilcke, Lithium−Air Battery: Promise and Challenges, J. Phys. Chem. Lett. 1 (2010) 2193–2203. doi:10.1021/jz1005384.

[15] R. Younesi, P. Norby, T. Vegge, A New Look at the Stability of Dimethyl Sulfoxide and Acetonitrile in Li-O2 Batteries, ECS Electrochem. Lett. 3 (2014) A15–A18. doi:10.1149/2.001403eel.

[16] N.M. Marković, P.N. Ross Jr., Surface science studies of model fuel cell electrocatalysts, Surf. Sci. Rep. 45 (2002) 117–229. doi:10.1016/S0167-5729(01)00022-X.

[17] J.O. Bockris, S.U.M. Khan, Surface Electrochemistry, Springer US, Boston, MA, 1993.

[18] R.G. Compton, G.H.W. Sanders, Electrode Potentials, 1 edition, Oxford University Press, Oxford ; New York, 1996.

[19] A.C. Fisher, Electrode Dynamics, 1 edition, Oxford University Press, Oxford ; New York, 1996.

[20] E. Gileadi, Physical Electrochemistry, 1 edition, Wiley-VCH, Weinheim, 2011.

[21] A.J. Bard, L.R. Faulkner, Electrochemical Methods: Fundamentals and Applications, 2 edition, Wiley, New York, 2000.

[22] R.J.D. Miller, G.L. McLendon, A.J. Nozik, W. Schmickler, F. Willig, Surface Electron Transfer Processes, 1 edition, Wiley-VCH, 1995.

[23] G. Gouy, Sur la constitution de la charge electrique a la surface d'un electrolyte, J Phys Fr. 9 (1910).

[24] O. Stern, The theory of the electrolytic double-layer, Z. Fuer Elektrochem. Angew. Phys. Chem. 30 (1924).

[25] D.C. Grahame, The Electrical Double Layer and the Theory of Electrocapillarity., Chem. Rev. 41 (1947) 441–501. doi:10.1021/cr60130a002.

[26] J.O. Bockris, M. a. V. Devanathan, K. Muller, On the Structure of Charged Interfaces, Proc. R. Soc. Lond. Math. Phys. Eng. Sci. 274 (1963) 55–79. doi:10.1098/rspa.1963.0114.

[27] J.P. Badiali, M.L. Rosinberg, J. Goodisman, Effect of solvent on properties of the liquid metal surface, J. Electroanal. Chem. Interfacial Electrochem. 130 (1981) 31–45. doi:10.1016/S0022-0728(81)80374-9.

[28] W. Schmickler, A jellium-dipole model for the double layer, J. Electroanal. Chem. Interfacial Electrochem. 150 (1983) 19–24. doi:10.1016/S0022-0728(83)80185-5.

[29] J.P. Badiali, M.L. Rosinberg, F. Vericat, L. Blum, A microscopic model for the liquid metal-ionic solution interface, J. Electroanal. Chem. Interfacial Electrochem. 158 (1983) 253–267. doi:10.1016/S0022-0728(83)80611-1.

[30] M.P. Marder, Condensed Matter Physics, 2 edition, Wiley, Hoboken, N.J, 2015.

[31] J. and White, Fundamentals of Optics, 3rd Edition edition, McGraw Hill, 1957.

[32] I.K. Robinson, Crystal truncation rods and surface roughness, Phys. Rev. B. 33 (1986) 3830–3836. doi:10.1103/PhysRevB.33.3830.

[33] W.H. Bragg, W.L. Bragg, The Reflection of X-rays by Crystals, Proc. R. Soc. Math. Phys. Eng. Sci. 88 (1913) 428–438. doi:10.1098/rspa.1913.0040.

[34] B.E. Warren, X-Ray Diffraction, Reprint edition, Dover Publications, New York, 1990.

[35] E. Prince, ed., International Tables for Crystallography: Mathematical, physical and chemical tables, 1st ed., International Union of Crystallography, Chester, England, 2006. http://it.iucr.org/Cb/ (accessed March 9, 2016).

[36] S. Brennan, P.L. Cowan, A suite of programs for calculating x-ray absorption, reflection, and diffraction performance for a variety of materials at arbitrary wavelengths, Rev. Sci. Instrum. 63 (1992) 850–853. doi:10.1063/1.1142625.

[37] F. Spaepen, A structural model for the solid-liquid interface in monatomic systems, Acta Metall. 23 (1975) 729–743. doi:10.1016/0001-6160(75)90056-5.

[38] W.A. Curtin, Density-functional theory of the solid-liquid interface, Phys. Rev. Lett. 59 (1987) 1228–1231. doi:10.1103/PhysRevLett.59.1228.

[39] F.F. Abraham, The interfacial density profile of a Lennard-Jones fluid in contact with a (100) Lennard-Jones wall and its relationship to idealized fluid/wall systems: A Monte Carlo simulation, J. Chem. Phys. 68 (1978) 3713. doi:10.1063/1.436229.

[40] P. Fenter, N.C. Sturchio, Calcite (1 0 4)–water interface structure, revisited, Geochim. Cosmochim. Acta. 97 (2012) 58–69. doi:10.1016/j.gca.2012.08.021.

[41] P. Fenter, N.C. Sturchio, Mineral–water interfacial structures revealed by synchrotron X-ray scattering, Prog. Surf. Sci. 77 (2004) 171–258. doi:10.1016/j.progsurf.2004.12.001.

[42] L.A. Kibler, Preparation and characterization of noble metal single crystal electrode surfaces, Short Course Held 51st 53rd Annu. Mtg ISE. (2003).

[43] D.. Kolb, An atomistic view of electrochemistry, Surf. Sci. 500 (2002) 722–740. doi:10.1016/S0039-6028(01)01583-7.

[44] M.G. Samant, M.F. Toney, G.L. Borges, L. Blum, O.R. Melroy, In-situ grazing incidence X-ray diffraction study of electrochemically deposited Pb monolayers on Ag(111), Surf. Sci. 193 (1988) L29–L36. doi:10.1016/0039-6028(88)90314-7.

[45] M.G. Samant, M.F. Toney, G.L. Borges, L. Blum, O.R. Melroy, Grazing incidence x-ray diffraction of lead monolayers at a silver (111) and gold (111) electrode/electrolyte interface, J. Phys. Chem. 92 (1988) 220–225. doi:10.1021/j100312a047.

[46] D. Vaughan, X-Ray Data Booklet. Center for X-Ray Optics. [Tables], 1985. http://www.osti.gov/servlets/purl/6359890-t6M9J7/ (accessed July 12, 2016).

[47] W.R. Busing, H.A. Levy, Angle calculations for 3- and 4-circle X-ray and neutron diffractometers, Acta Crystallogr. 22 (1967) 457–464. doi:10.1107/S0365110X67000970.

[48] K.W. Evans-Lutterodt, M.T. Tang, Angle Calculations for a `2+2' Surface X-ray Diffractometer, J. Appl. Crystallogr. 28 (1995) 318–326. doi:10.1107/S0021889894011131.

[49] J.M. Bloch, Angle and index calculations for ` z -axis' X-ray diffractometer, J. Appl. Crystallogr. 18 (1985) 33–36. doi:10.1107/S0021889885009724.

[50] E. Vlieg, A (2+3)-Type Surface Diffractometer: Mergence of the z-Axis and (2+2)-Type Geometries, J. Appl. Crystallogr. 31 (1998) 198–203. doi:10.1107/S0021889897009990.

[51] M. Lohmeier, E. Vlieg, Angle calculations for a six-circle surface X-ray diffractometer, J. Appl. Crystallogr. 26 (1993) 706–716. doi:10.1107/S0021889893004868.

[52] P. Fenter, J.G. Catalano, C. Park, Z. Zhang, On the use of CCD area detectors for high-resolution specular X-ray reflectivity, J. Synchrotron Radiat. 13 (2006) 293–303. doi:10.1107/S0909049506018000.

[53] E. Vlieg, Integrated Intensities Using a Six-Circle Surface X-ray Diffractometer, J. Appl. Crystallogr. 30 (1997) 532–543. doi:10.1107/S0021889897002537.

[54] M. Haruta, T. Kobayashi, H. Sano, N. Yamada, Novel Gold Catalysts for the Oxidation of Carbon Monoxide at a Temperature far Below 0 °C, Chem. Lett. 16 (1987) 405–408.

[55] M. Haruta, Catalysis: Gold rush, Nature. 437 (2005) 1098–1099. doi:10.1038/4371098a.

[56] A.S.K. Hashmi, G.J. Hutchings, Gold Catalysis, Angew. Chem. Int. Ed. 45 (2006) 7896–7936. doi:10.1002/anie.200602454.

[57] P. Rodriguez, J.M. Feliu, M.T.M. Koper, Unusual adsorption state of carbon monoxide on single-crystalline gold electrodes in alkaline media, Electrochem. Commun. 11 (2009) 1105–1108. doi:10.1016/j.elecom.2009.03.018.

[58] P. Rodriguez, N. Garcia-Araez, A. Koverga, S. Frank, M.T.M. Koper, CO Electroxidation on Gold in Alkaline Media: A Combined Electrochemical, Spectroscopic, and DFT Study, Langmuir. 26 (2010) 12425–12432. doi:10.1021/la1014048.

[59] P. Rodríguez, A.A. Koverga, M.T.M. Koper, Carbon Monoxide as a Promoter for its own Oxidation on a Gold Electrode, Angew. Chem. Int. Ed. 49 (2010) 1241–1243. doi:10.1002/anie.200905387.

[60] P. Rodriguez, N. Garcia-Araez, M.T.M. Koper, Self-promotion mechanism for CO electrooxidation on gold, Phys. Chem. Chem. Phys. 12 (2010) 9373–9380. doi:10.1039/B926365A.

[61] A.A. Koverga, S. Frank, M.T.M. Koper, Density Functional Theory study of electric field effects on CO and OH adsorption and co-adsorption on gold surfaces, Electrochimica Acta. (n.d.). doi:10.1016/j.electacta.2012.12.061.

[62] D.M. Kolb, Reconstruction phenomena at metal-electrolyte interfaces, Prog. Surf. Sci. 51 (1996) 109–173. doi:10.1016/0079-6816(96)00002-0.

[63] D.M. Kolb, J. Schneider, Surface reconstruction in electrochemistry: Au(100-(5 × 20), Au(111)-(1 × 23) and Au(110)-(1 × 2), Electrochimica Acta. 31 (1986) 929–936. doi:10.1016/0013-4686(86)80005-6.

[64] M.E. Gallagher, B.B. Blizanac, C.A. Lucas, P.N. Ross, N.M. Marković, Structure sensitivity of CO oxidation on gold single crystal surfaces in alkaline solution:

Surface X-ray scattering and rotating disk measurements, Surf. Sci. 582 (2005) 215–226. doi:10.1016/j.susc.2005.03.018.

[65] C.A. Lucas, P. Thompson, Y. Gründer, N.M. Markovic, The structure of the electrochemical double layer: Ag(111) in alkaline electrolyte, Electrochem. Commun. 13 (2011) 1205–1208. doi:10.1016/j.elecom.2011.08.043.

[66] C.A. Lucas, N.M. Markovic, Structure Relationships in Electrochemical Reactions, Encycl. Electrochem. 2 (2003) 295–359.

[67] P.A. Thiel, P.J. Estrup, The Handbook of Surface Imaging and Visualization, CRC Press: Boca Raton, 1995.

[68] J. Wang, A.J. Davenport, H.S. Isaacs, B.M. Ocko, Surface Charge—Induced Ordering of the Au(111) Surface, Science. 255 (1992) 1416–1418. doi:10.1126/science.255.5050.1416.

[69] K.P. Bohnen, D.M. Kolb, Charge- versus adsorbate-induced lifting of the Au(100)-(hex) reconstruction in an electrochemical environment, Surf. Sci. 407 (1998) L629–L632. doi:10.1016/S0039-6028(98)00232-5.

[70] B.M. Ocko, J. Wang, A. Davenport, H. Isaacs, In situ x-ray reflectivity and diffraction studies of the Au(001) reconstruction in an electrochemical cell, Phys. Rev. Lett. 65 (1990) 1466–1469. doi:10.1103/PhysRevLett.65.1466.

[71] J. Wang, B.M. Ocko, A.J. Davenport, H.S. Isaacs, \textit{In situ} x-ray-diffraction and -reflectivity studies of the Au(111)/electrolyte interface: Reconstruction and anion adsorption, Phys. Rev. B. 46 (1992) 10321–10338. doi:10.1103/PhysRevB.46.10321.

[72] C.A. Lucas, N.M. Marković, P.N. Ross, The adsorption and oxidation of carbon monoxide at the Pt(111)/electrolyte interface: atomic structure and surface relaxation, Surf. Sci. 425 (1999) L381–L386. doi:10.1016/S0039-6028(99)00252-6.

[73] S. Beyhan, K. Uosaki, J.M. Feliu, E. Herrero, Electrochemical and in situ FTIR studies of ethanol adsorption and oxidation on gold single crystal electrodes in alkaline media, J. Electroanal. Chem. 707 (2013) 89–94. doi:10.1016/j.jelechem.2013.08.034.

[74] L. Piccolo, D. Loffreda, F.J. Cadete Santos Aires, C. Deranlot, Y. Jugnet, P. Sautet, J.C. Bertolini, The adsorption of CO on Au(1 1 1) at elevated pressures studied by STM, RAIRS and DFT calculations, Surf. Sci. 566–568, Part 2 (2004) 995–1000. doi:10.1016/j.susc.2004.06.042.

[75] K.F. Peters, P. Steadman, H. Isern, J. Alvarez, S. Ferrer, Elevated-pressure chemical reactivity of carbon monoxide over Au(111), Surf. Sci. 467 (2000) 10–22. doi:10.1016/S0039-6028(00)00777-9.

[76] J. Weissmüller, R.N. Viswanath, L.A. Kibler, D.M. Kolb, Impact of surface mechanics on the reactivity of electrodes, Phys. Chem. Chem. Phys. 13 (2011) 2114–2117. doi:10.1039/C0CP01742F.

[77] M. Gsell, P. Jakob, D. Menzel, Effect of Substrate Strain on Adsorption, Science. 280 (1998) 717–720. doi:10.1126/science.280.5364.717.

[78] M. Mavrikakis, B. Hammer, J.K. Nørskov, Effect of Strain on the Reactivity of Metal Surfaces, Phys. Rev. Lett. 81 (1998) 2819–2822. doi:10.1103/PhysRevLett.81.2819.

[79] A.M. Nowicka, U. Hasse, M. Donten, M. Hermes, Z.J. Stojek, F. Scholz, The treatment of Ag, Pd, Au and Pt electrodes with OH• radicals reveals information on the nature of the electrocatalytic centers, J. Solid State Electrochem. 15 (2011) 2141–2147. doi:10.1007/s10008-011-1488-3.

[80] High catalytic activity of chemically activated gold electrodes towards electro-oxidation of methanol, (n.d.). http://www.sciencedirect.com/science/article/pii/S0013468604001732 (accessed March 3, 2016).

[81] J. Hernández, J. Solla-Gullón, E. Herrero, A. Aldaz, J.M. Feliu, Methanol oxidation on gold nanoparticles in alkaline media: Unusual electrocatalytic activity, Electrochimica Acta. 52 (2006) 1662–1669. doi:10.1016/j.electacta.2006.03.091.

[82] Electrooxidation of methanol on polycrystalline and single crystal gold electrodes, (n.d.). http://www.sciencedirect.com/science/article/pii/S0013468603009125 (accessed March 3, 2016).

[83] B. Eren, D. Zherebetskyy, L.L. Patera, C.H. Wu, H. Bluhm, C. Africh, L.-W. Wang, G.A. Somorjai, M. Salmeron, Activation of Cu(111) surface by decomposition into nanoclusters driven by CO adsorption, Science. 351 (2016) 475–478. doi:10.1126/science.aad8868.

[84] G.A. Camara, T. Iwasita, Parallel pathways of ethanol oxidation: The effect of ethanol concentration, J. Electroanal. Chem. 578 (2005) 315–321. doi:10.1016/j.jelechem.2005.01.013.

[85] M. Mamatkulov, J.-S. Filhol, Intrinsic Electrochemical and Strain Effects in Nanoparticles, J. Phys. Chem. C. 117 (2013) 2334–2343. doi:10.1021/jp3099494.

[86] N.M. Marković, T.J. Schmidt, V. Stamenković, P.N. Ross, Oxygen Reduction Reaction on Pt and Pt Bimetallic Surfaces: A Selective Review, Fuel Cells. 1 (2001) 105–116. doi:10.1002/1615-6854(200107)1:2<105::AID-FUCE105>3.0.CO;2-9.

[87] K. Apel, H. Hirt, REACTIVE OXYGEN SPECIES: Metabolism, Oxidative Stress, and Signal Transduction, Annu. Rev. Plant Biol. 55 (2004) 373–399. doi:10.1146/annurev.arplant.55.031903.141701.

[88] D.T. Sawyer, Oxygen Chemistry, Oxford University Press, 1991.

[89] A.C. Luntz, B.D. McCloskey, Nonaqueous Li–Air Batteries: A Status Report, Chem. Rev. 114 (2014) 11721–11750. doi:10.1021/cr500054y.

[90] L. Johnson, C. Li, Z. Liu, Y. Chen, S.A. Freunberger, P.C. Ashok, B.B. Praveen, K. Dholakia, J.-M. Tarascon, P.G. Bruce, The role of LiO2 solubility in O2 reduction in aprotic solvents and its consequences for Li–O2 batteries, Nat. Chem. 6 (2014) 1091–1099. doi:10.1038/nchem.2101.

[91] T. Liu, M. Leskes, W. Yu, A.J. Moore, L. Zhou, P.M. Bayley, G. Kim, C.P. Grey, Cycling Li-O2 batteries via LiOH formation and decomposition, Science. 350 (2015) 530–533. doi:10.1126/science.aac7730.

[92] N.B. Aetukuri, B.D. McCloskey, J.M. García, L.E. Krupp, V. Viswanathan, A.C. Luntz, Solvating additives drive solution-mediated electrochemistry and enhance toroid growth in non-aqueous Li–O2 batteries, Nat. Chem. 7 (2015) 50–56. doi:10.1038/nchem.2132.

[93] M. Safari, B.D. Adams, L.F. Nazar, Kinetics of Oxygen Reduction in Aprotic Li–O2 Cells: A Model-Based Study, J. Phys. Chem. Lett. 5 (2014) 3486–3491. doi:10.1021/jz5018202.

[94] Z. Peng, S.A. Freunberger, L.J. Hardwick, Y. Chen, V. Giordani, F. Bardé, P. Novák, D. Graham, J.-M. Tarascon, P.G. Bruce, Oxygen Reactions in a Non-Aqueous Li+ Electrolyte, Angew. Chem. 123 (2011) 6475–6479. doi:10.1002/ange.201100879.

[95] F. Endres, Ionic Liquids: Solvents for the Electrodeposition of Metals and Semiconductors, ChemPhysChem. 3 (2002) 144–154. doi:10.1002/1439-7641(20020215)3:2<144::AID-CPHC144>3.0.CO;2-#.

[96] D. Gal, G. Hodes, D. Lincot, H.-W. Schock, Electrochemical deposition of zinc oxide films from non-aqueous solution: a new buffer/window process for thin film solar cells, Thin Solid Films. 361–362 (2000) 79–83. doi:10.1016/S0040-6090(99)00772-5.

[97] J. Ge, J. St-Pierre, Y. Zhai, PEMFC cathode catalyst contamination evaluation with a RRDE-Acetonitrile, Electrochimica Acta. 134 (2014) 272–280. doi:10.1016/j.electacta.2014.04.149.

[98] T.V. Reshetenko, J. St-Pierre, Study of acetylene poisoning of Pt cathode on proton exchange membrane fuel cell spatial performance using a segmented cell system, J. Power Sources. 287 (2015) 401–415. doi:10.1016/j.jpowsour.2015.04.073.

[99] Y.-C. Lu, H.A. Gasteiger, Y. Shao-Horn, Catalytic Activity Trends of Oxygen Reduction Reaction for Nonaqueous Li-Air Batteries, J. Am. Chem. Soc. 133 (2011) 19048–19051. doi:10.1021/ja208608s.

[100] V. Viswanathan, H.A. Hansen, J. Rossmeisl, J.K. Nørskov, Universality in Oxygen Reduction Electrocatalysis on Metal Surfaces, ACS Catal. 2 (2012) 1654–1660. doi:10.1021/cs300227s.

[101] V.S. Bryantsev, J. Uddin, V. Giordani, W. Walker, D. Addison, G.V. Chase, The Identification of Stable Solvents for Nonaqueous Rechargeable Li-Air Batteries, J. Electrochem. Soc. 160 (2013) A160–A171. doi:10.1149/2.027302jes.

[102] I.M. Aldous, L.J. Hardwick, Influence of Tetraalkylammonium Cation Chain Length on Gold and Glassy Carbon Electrode Interfaces for Alkali Metal–Oxygen Batteries, J. Phys. Chem. Lett. 5 (2014) 3924–3930. doi:10.1021/jz501850u.

[103] Z. Peng, S.A. Freunberger, L.J. Hardwick, Y. Chen, V. Giordani, F. Bardé, P. Novák, D. Graham, J.-M. Tarascon, P.G. Bruce, Oxygen Reactions in a Non-Aqueous Li+ Electrolyte, Angew. Chem. Int. Ed. 50 (2011) 6351–6355. doi:10.1002/anie.201100879.

[104] P. Cao, Y. Sun, R. Gu, Investigations of chemisorption and reaction at non-aqueous electrochemical interfaces by in situ surface-enhanced Raman spectroscopy, J. Raman Spectrosc. 36 (2005) 725–735. doi:10.1002/jrs.1341.

[105] P. Cao, Y. Sun, On the Occurrence of Competitive Adsorption at the Platinum−Acetonitrile Interface by Using Surface-Enhanced Raman Spectroscopy, J. Phys. Chem. B. 107 (2003) 5818–5824. doi:10.1021/jp027834j.

[106] N.S. Marinković, M. Hecht, J.S. Loring, W.R. Fawcett, A sniftirs study of the diffuse double layer at single crystal platinum electrodes in acetonitrile, Electrochimica Acta. 41 (1996) 641–651. doi:10.1016/0013-4686(95)00352-5.

[107] S. Baldelli, G. Mailhot, P. Ross, Y.-R. Shen, G.A. Somorjai, Potential Dependent Orientation of Acetonitrile on Platinum (111) Electrode Surface Studied by Sum Frequency Generation, J. Phys. Chem. B. 105 (2001) 654–662. doi:10.1021/jp002546d.

[108] S. Morin, B.E. Conway, Surface structure dependence of reactive chemisorption of acetonitrile on single-crystal Pt surfaces, J. Electroanal. Chem. 376 (1994) 135–150. doi:10.1016/0022-0728(94)03539-3.

[109] M.F. Suárez-Herrera, M. Costa-Figueiredo, J.M. Feliu, Voltammetry of Basal Plane Platinum Electrodes in Acetonitrile Electrolytes: Effect of the Presence of Water, Langmuir. 28 (2012) 5286–5294. doi:10.1021/la205097p.

[110] H. Angerstein-Kozlowska, B. Macdougall, B.E. Conway, Electrochemisorption and reactivity of nitriles at platinum electrodes and the anodic H desorption effect, J. Electroanal. Chem. Interfacial Electrochem. 39 (1972) 287–313. doi:10.1016/S0022-0728(72)80153-0.

[111] M. Mezger, S. Schramm, H. Schröder, H. Reichert, M. Deutsch, E.J.D. Souza, J.S. Okasinski, B.M. Ocko, V. Honkimäki, H. Dosch, Layering of [BMIM]+-based ionic liquids at a charged sapphire interface, J. Chem. Phys. 131 (2009) 94701. doi:10.1063/1.3212613.

[112] M. Mezger, H. Schröder, H. Reichert, S. Schramm, J.S. Okasinski, S. Schöder, V. Honkimäki, M. Deutsch, B.M. Ocko, J. Ralston, M. Rohwerder, M. Stratmann, H. Dosch, Molecular Layering of Fluorinated Ionic Liquids at a Charged Sapphire (0001) Surface, Science. 322 (2008) 424–428. doi:10.1126/science.1164502.

[113] A. Uysal, H. Zhou, G. Feng, S.S. Lee, S. Li, P. Fenter, P.T. Cummings, P.F. Fulvio, S. Dai, J.K. McDonough, Y. Gogotsi, Structural Origins of Potential Dependent Hysteresis at the Electrified Graphene/Ionic Liquid Interface, J. Phys. Chem. C. 118 (2014) 569–574. doi:10.1021/jp4111025.

[114] E. Sloutskin, B.M. Ocko, L. Tamam, I. Kuzmenko, T. Gog, M. Deutsch, Surface Layering in Ionic Liquids: An X-ray Reflectivity Study, J. Am. Chem. Soc. 127 (2005) 7796–7804. doi:10.1021/ja0509679.

[115] K. Tamura, S. Miyaguchi, K. Sakaue, Y. Nishihata, J. 'ichiro Mizuki, Direct observation of Au(111) electrode surface structure in bis(trifluoromethylsulfonyl)amide-based ionic liquids using surface X-ray scattering, Electrochem. Commun. 13 (2011) 411–413. doi:10.1016/j.elecom.2011.02.006.

[116] K. Tamura, Y. Nishihata, Study on the Behavior of Halide Ions on the Au(111) Electrode Surface in Ionic Liquids Using Surface X-ray Scattering, J. Phys. Chem. C. (2016). doi:10.1021/acs.jpcc.5b09704.

[117] K. Tamura, B.M. Ocko, J.X. Wang, R.R. Adžić, Structure of Active Adlayers on Bimetallic Surfaces: Oxygen Reduction on Au(111) with Bi Adlayers, J. Phys. Chem. B. 106 (2002) 3896–3901. doi:10.1021/jp012960t.

[118] V.V. Pavlishchuk, A.W. Addison, Conversion constants for redox potentials measured versus different reference electrodes in acetonitrile solutions at 25°C, Inorganica Chim. Acta. 298 (2000) 97–102. doi:10.1016/S0020-1693(99)00407-7.

[119] R.M. Ishikawa, A.T. Hubbard, Study of platinum electrodes by means of thin layer electrochemistry and low-energy electron diffraction 0, J. Electroanal. Chem. Interfacial Electrochem. 69 (1976) 317–338. doi:10.1016/S0022-0728(76)80133-7.

[120] I.M. Tidswell, N.M. Markovic, P.N. Ross, Potential dependent surface structure of the Pt(1 1 1) electrolyte interface, J. Electroanal. Chem. 376 (1994) 119–126. doi:10.1016/0022-0728(94)03553-9.

[121] L.A. Kibler, A. Cuesta, M. Kleinert, D.M. Kolb, In-situ STM characterisation of the surface morphology of platinum single crystal electrodes as a function of their preparation, J. Electroanal. Chem. 484 (2000) 73–82. doi:10.1016/S0022-0728(00)00065-6.

[122] C.. Lucas, Surface relaxation at the metal/electrolyte interface, Electrochimica Acta. 47 (2002) 3065–3074. doi:10.1016/S0013-4686(02)00225-6.

[123] G.A. Garwood Jr., A.T. Hubbard, Superlattices formed by interaction of polar solvents with Pt(111) surfaces studied by LEED, Auger spectroscopy and thermal desorption mass spectrometry, Surf. Sci. 118 (1982) 223–247. doi:10.1016/0039-6028(82)90025-5.

[124] D. Jürgens, G. Held, H. Pfnür, Adsorbate induced relaxations of S/Ru(0001): p(2 × 2) and p(√3 × √3)R30° structures, Surf. Sci. 303 (1994) 77–88. doi:10.1016/0039-6028(94)90621-1.

[125] D. Menzel, Adsorbate-induced global and local expansions and contractions of a close-packed transition metal surface, Surf. Rev. Lett. 4 (1997) 1283–1289. doi:10.1142/S0218625X97001681.

[126] P. Fenter, M.T. McBride, G. Srajer, N.C. Sturchio, D. Bosbach, Structure of Barite (001)− and (210)−Water Interfaces, J. Phys. Chem. B. 105 (2001) 8112–8119. doi:10.1021/jp0105600.

[127] T. Roman, A. Groß, Structure of water layers on hydrogen-covered Pt electrodes, Catal. Today. 202 (2013) 183–190. doi:10.1016/j.cattod.2012.06.001.

[128] M. Osawa, M. Tsushima, H. Mogami, G. Samjeské, A. Yamakata, Structure of Water at the Electrified Platinum−Water Interface: A Study by Surface-Enhanced Infrared Absorption Spectroscopy, J. Phys. Chem. C. 112 (2008) 4248–4256. doi:10.1021/jp710386g.

[129] T. Iwasita, X. Xia, Adsorption of water at Pt(111) electrode in HClO4 solutions. The potential of zero charge, J. Electroanal. Chem. 411 (1996) 95–102. doi:10.1016/0022-0728(96)04576-7.

[130] A. Berna, V. Climent, J. Feliu, New understanding of the nature of OH adsorption on Pt(111) electrodes, Electrochem. Commun. 9 (2007) 2789–2794. doi:10.1016/j.elecom.2007.09.018.

[131] B.E. Conway, Electrochemical surface science: The study of monolayers of ad-atoms and solvent molecules at charged metal interfaces, Prog. Surf. Sci. 16 (1984) 1–137. doi:10.1016/0079-6816(84)90008-X.

[132] D. Strmcnik, K. Kodama, D. van der Vliet, J. Greeley, V.R. Stamenkovic, N.M. Marković, The role of non-covalent interactions in electrocatalytic fuel-cell reactions on platinum, Nat. Chem. 1 (2009) 466–472. doi:10.1038/nchem.330.

[133] M. Watanabe, D.A. Tryk, M. Wakisaka, H. Yano, H. Uchida, Overview of recent developments in oxygen reduction electrocatalysis, Electrochimica Acta. 84 (2012) 187–201. doi:10.1016/j.electacta.2012.04.035.

[134] G.A. Attard, A. Brew, K. Hunter, J. Sharman, E. Wright, Specific adsorption of perchlorate anions on Pt{hkl} single crystal electrodes, Phys. Chem. Chem. Phys. 16 (2014) 13689–13698. doi:10.1039/C4CP00564C.

[135] A.V. Rudnev, E.B. Molodkina, A.I. Danilov, Y.M. Polukarov, A. Berna, J.M. Feliu, Adsorption behavior of acetonitrile on platinum and gold electrodes of various structures in solution of 0.5 M H2SO4, Electrochimica Acta. 54 (2009) 3692–3699. doi:10.1016/j.electacta.2009.01.047.

[136] I. Srejić, M. Smiljanić, Z. Rakočević, S. Štrbac, Oxygen reduction on polycrystalline Pt and Au electrodes in perchloric acid solution in the presence of acetonitrile, Int. J. Electrochem. Sci. 6 (2011) 3344–3354.

[137] N. Markovic, P.N. Ross, The effect of specific adsorption of ions and underpotential deposition of copper on the electro-oxidation of methanol on platinum single-crystal surfaces, J. Electroanal. Chem. 330 (1992) 499–520. doi:10.1016/0022-0728(92)80327-Z.

[138] N.M. Marković, T.J. Schmidt, B.N. Grgur, H.A. Gasteiger, R.J. Behm, P.N. Ross, Effect of Temperature on Surface Processes at the Pt(111)−Liquid Interface: Hydrogen Adsorption, Oxide Formation, and CO Oxidation, J. Phys. Chem. B. 103 (1999) 8568–8577. doi:10.1021/jp991826u.

[139] A.M. Funtikov, U. Stimming, R. Vogel, Anion adsorption from sulfuric acid solutions on Pt(111) single crystal electrodes, J. Electroanal. Chem. 428 (1997) 147–153. doi:10.1016/S0022-0728(96)05051-6.

[140] T.J. Schmidt, P.N. Ross, N.M. Markovic, Temperature-Dependent Surface Electrochemistry on Pt Single Crystals in Alkaline Electrolyte: Part 1: CO Oxidation, J. Phys. Chem. B. 105 (2001) 12082–12086. doi:10.1021/jp0124037.

[141] C.A. Lucas, N.M. Markovic-acute, P.N. Ross, Adsorption of halide anions at the Pt(111)-solution interfacestudied by in situ surface x-ray scattering, Phys. Rev. B. 55 (1997) 7964–7971. doi:10.1103/PhysRevB.55.7964.

[142] J.M. Orts, R. Gómez, J.M. Feliu, A. Aldaz, J. Clavilier, Potentiostatic charge displacement by exchanging adsorbed species on Pt(111) electrodes—acidic electrolytes with specific anion adsorption, Electrochimica Acta. 39 (1994) 1519–1524. doi:10.1016/0013-4686(94)85129-8.

[143] T. Pajkossy, D.M. Kolb, Double layer capacitance of Pt(111) single crystal electrodes, Electrochimica Acta. 46 (2001) 3063–3071. doi:10.1016/S0013-4686(01)00597-7.

[144] P.J. Feibelman, First-principles calculations of stress induced by gas adsorption on Pt(111), Phys. Rev. B. 56 (1997) 2175–2182. doi:10.1103/PhysRevB.56.2175.

[145] A. Więckowski, The classification of adsorption processes of organic compounds on platinum electrode. The role of water molecules chemisorbed on platinum, Electrochimica Acta. 26 (1981) 1121–1124. doi:10.1016/0013-4686(81)85087-6.

10 APPENDICES

APPENDIX 1 COMPUTER CODE FOR THE CALCULATION OF A CTR PROFILE

This section contains snippets of code for which it should be possible to reconstruct a CTR calculation, such as the ones used to model the data. The code has been slightly simplified with certain things like error checking/validation not included to improve readability. Fitting, minimisation, error checking and graphing code not included. The code is written in python 2.7

```
'''This program almost certainly won't run, but instead demonstrates how the
calculations are done and is meant to be read'''

'''The program is based on a combination of a FORTRAN program by Chris Lucas and the ROD
fitting program by E. Vlieg. A useable version can be obtained from the author, Gary
Harlow, if required'''

'''The lmfit-py library to allow easy parametrisation of variables and the calculation
of confidence intervals and was used in the full version of this program'''

'''Python libraries used'''
import lmfit as lf
import numpy as np
import scipy

#Constants
geo = [VERSLIT, HORSLIT, HORBEAM, VERBEAM, RADIUS, DSLIT]
constants = [a, wavelength, bulkdwf]


'''Funcation to calculate the scattering factor using the Crommer-Mann equation'''
def f_atom(q, atom):

    #coefficents taken from International Tables for Crystallography Vol C. Ch 6.1
    #f1 and f2 taken from the Brennan-Cowan tabulation and need updating with energy
    if atom == "Au":
        #     a1      a2    a3  a4  b1  b2  b3  b4  c
        coeff = [16.8819,0.4611,18.5913,8.6216,25.5582,1.4826,5.86,36.3956,12.0658]
        f1=-11.35
        f2=3.96
    if atom == "Pt":
        coeff =[27.0059,1.51293,17.7639,8.81174,15.7131,0.424593,5.7837,38.6103,11.6883]
        f1=-2.157
        f2=8.020
    if atom == "O":
        coeff =[3.0485,13.2771,2.2868,5.7011,1.5463,0.3239,0.867,32.9089,0.2508]
        f1=-0.022
        f2=0.14
    if atom == "C":
        coeff = [2.31,20.8439,1.02,10.2075,1.5886,0.5687,0.865,51.6512,0.2156]
        f1=0.09
        f2=0.004
    if atom == "Cu":
        coeff = [13.338,3.58280,7.16760,0.247000,5.6158,11.3966,1.6735,64.6126,1.19]
        f1=-0.575
        f2=2.737
    if atom == "N":
        coeff = [12.2126,0.0057,3.1322,9.8933,2.0125,28.9975,1.1663,0.5826,-11.529]
        f1=0.01726
        f2=0.00917

    # add atoms here

    x=(q/(4*np.pi))**2 # sin(theta)^2/lambda^2
    if x > 1.5:
        print "WARNING: Scattering factor approximation not vaild at this Q!!"
        quit()
```

```
    f = coeff[8]
    for i in xrange(4):
        f += coeff[i*2]*np.exp(-coeff[i*2+1]*x)
    f +=f1+1j*f2

    return f

'''*****************************************************************************************
#Correction Factors
#*****************************************************************************************''
'
'''Correction based on code by C. Lucas for 4-circle diffractomer'''
def corr4c(hkl,q, qz ,qinp, params):

   #make code a bit more readable
    pi = np.pi
    h = hkl[0]
    k = hkl[1]
    l = hkl[2]
    wavelength = constants[1]
    t = params['transm'].value  #Transmission of beam (perpendicular)

    #calculate angles
    angi=np.arcsin(wavelength*qz/(4*pi))

    #if specular
    if(round(h)==int(rods[0]) and round(k)==int(rods[1])):
        ampcorr = 1/(np.sin(angi)**2)
        brat = params['brat_spec'].value    #beam to sample ratio
    else:
        brat = params['brat_offspec'].value #beam to sample ratio
        theta=np.arcsin(q*wavelength/(4*pi))
        chi=np.arctan(qz/qinp) # see Fenter guide to reflectivity appendix

        angi=np.arcsin(np.sin(theta)*np.sin(chi))
        ampcorr = 1/(np.sin(chi)**2 * (np.sin(theta)**2))

    #low angle area correction
    acorr=brat*np.sin(angi)
    if(acorr > 1): acorr=1

    #Transmission for a thin layer
    T = t**(2/(np.sin(angi)))

    #return correction
    return acorr*ampcorr*T

'''Correction factor for 2+3 diffractometer based on ana-rod programm'''
def diamond(hkl,angles):

    h = hkl[0]
    k = hkl[1]
    l = hkl[2]
    deg_to_rad = 0.0174532925
    pi = np.pi

    #read angles and convert to radians
    alpha = angles[0]*deg_to_rad
    delta = angles[1]*deg_to_rad
    gamma = angles[2]*deg_to_rad

    VERSLIT = geo[0]   #In plane beamslit width
    HORSLIT = geo[1]   #Out of plane beam slit width
    HORBEAM = geo[2]   #Horizontal beamwidth
    VERBEAM = geo[3]   #Vertical beamwidth
    RADIUS = geo[4]    #Sample radius
    DSLIT = geo[5]     #In-plane detector slit width

    #If specular use the similar Lorentz factor
    if h==0 and k==0:
        lor = np.sin(2*alpha)
    else:
        lor = np.sin(delta)*np.cos(alpha)

    #calculate beta out
    c_beta = np.sqrt(1-(np.cos(delta)*np.sin(gamma-alpha)))
```

```
    #rod interception
    rod = c_beta

    #horizontal and vertical polarisation factors
    p_hor = 1 - (np.cos(delta)*np.sin(gamma))**2
    p_ver = 1 - np.sin(delta)**2

    #Total polarisation correction
    ph = 1      #amount beam is horizontally polarised
    pol = (ph*p_hor + (1-ph)*p_ver)
    #area correction - not including beam profile and sample size
    #area_corr =c_beta/np.sin(delta)

    #Numerical sample area correction - From ANA program
'''-------------------------------------------------------------------------------'''
    '''Funcations taken from ANA program to numerically calculate geomterical
corrections'''
    def f_beam(x ,z):
        VERSLIT = geo[0]   #In plane beamslit width
        HORSLIT = geo[1]   #Out of plane beam slit width
        HORBEAM = geo[2]   #Horizontal beamwidth
        VERBEAM = geo[3]   #Vertical beamwidth
        if (abs(x) > VERSLIT/2.0) or (abs(z) > HORSLIT/2.0):
            return 0.0
        else:
            return (np.exp(-2.77*x*x/(VERBEAM*VERBEAM))*np.exp(-
2.77*z*z/(HORBEAM*HORBEAM)))

    def f_onsample(x,y):
        RADIUS = geo[4] #Sample radius

        if(((x*x)+(y*y)) > (RADIUS*RADIUS)):
            return 0.0
        else:
            return 1.0

    def f_detector(x):
        DSLIT = geo[5]  #In-plane detector slit width

        if(abs(x) > DSLIT/2.0):
            return 0.0
        else:
            return 1.0
'''-------------------------------------------------------------------------------'''
    c1 = np.sin(alpha)
    c2 = np.cos(delta)
    c3 = np.sin(delta)*np.cos(gamma-alpha)
    area_sum = 0

    #Determine integration limit along x (vertical) direction

    if(VERSLIT > 0.01):
        xlimit = VERSLIT/2+0.01
    else:
        xlimit = 1.0
    xstep = xlimit/50.0

    #Determine integration limit along y (horizontal) direction
    if(RADIUS > 0.01):
        ylimit = RADIUS*1.1
    else:
        ylimit = 10

    if(abs(2*HORBEAM/np.sin(alpha+0.001)) < ylimit):
        ylimit = abs(2*HORBEAM/np.sin(alpha+0.001))

    if(1.1*HORSLIT/(2*np.sin(alpha+0.001)) < ylimit):
        ylimit = 1.1*HORSLIT/(2*np.sin(alpha+0.001))
    ystep = ylimit/50.0

    for x in np.arange(-xlimit,xlimit+0.01, xstep):
        for y in np.arange(-ylimit,ylimit+0.01,ystep):
            area_sum +=f_beam(x,y*c1)*f_detector(x*c2-y*c3)*f_onsample(x,y)

    #Calculate effective vertical beam slit size
    bs_eff = 0.0
    for x in np.arange(-xlimit,xlimit,xstep/10):
```

```
            bs_eff += f_beam(x,0)
        bs_eff *= xstep/10

        area_corr = 1/((DSLIT*bs_eff)/(area_sum*xstep*ystep))
        t = params['transm'].value
        #Transmission for a thin layer (allows alpha != beta)
        T = t**(1/np.sin(alpha) +1/np.sin(np.arccos(c_beta)))


        return pol*lor*rod*area_corr*T

'''*****************************************************************************
# WATER MODELS
#*****************************************************************************
#The following two functions are taken from Mineral-Water interfaces by
#P. Fenter and N. Sturchio, Progress in Surface Science 2004'''

#Error function
def error_func(sigma, q,a):
        '''Esigma =rms width of water profile
        Edist is height above origin (include any surface layers in
        height when calling)'''

        pw = 0.033                      #density of water
        uc_area = a**2                  #unit cell area
        zwater = (9/8)*f_atom(q, "O") #scattering factor of water

        #This is error function
        flayer = 1j*zwater*(pw*uc_area)*np.exp(-0.5*(q*sigma)**2)/q
        return flayer

#Layered water model
def layered_model(sigma_0, sigma_bar, spacing,q,a):
        '''simga_0 is rms of water profile
        simga_bar is successive broadening where:
                simga_j = sqrt(simga_0**2 + j*sigma_bar**2)
        spacing is the layer spacing.'''

        pw = 0.033                       #density of water
        uc_area = a**2                   #unit cell area
        zwater = (9/8)*f_atom(q, "O")  #scattering factor of water

        temp = np.exp(-0.5*(q*sigma_bar)**2)*np.exp(1j*q*spacing)
        flayer = spacing*(zwater)*pw*uc_area*np.exp(-0.5*(q*sigma_0)**2)
        return flayer/(1-temp)

'''*****************************************************************************'''

def model(h,k,l,params,angles):
    '''This is the model function that is minmised'''
    #Different scale factors
    #specular
    if round(h) == int(rods[0]) and round(k) ==int(rods[1]):
        specular = True
        scale = params['scale00'].value
    #rod 1
    elif round(h) == int(rods[2]) and round(k) == int(rods[3]):
        specular = False
        scale = params['scale01'].value
    #rod 2
    elif round(h) == int(rods[4]) and round(k) == int(rods[5]):
        specular = False
        scale = params['scale10'].value
    else:
        print "Unrecognised rod!"
        quit()

    #constants
    pi = np.pi
    a = constants[0]    #lattice constant
    wavelength = constants[1]
    a3 = np.sqrt(3)*a   #height of unit cell


    #111
    #transform recp. unit cell
    h_cub = h*2/3 - k *2/3 + l/3
```

```
k_cub = h*2/3 + k*4/3 + l/3
l_cub = -h*4/3 - k*2/3 + l/3

hinp=h*2/3-k*2/3
kinp=h*2/3+k*4/3
linp=-h*4/3-k*2/3

q = 2*pi*np.sqrt(h_cub**2 + k_cub**2 + l_cub**2)/a
qinp=2*pi*np.sqrt(hinp**2+kinp**2+linp**2)/a
qz = (2*pi*l)/a3

#caluclate scattering factors
f_adlayer= [0, f_atom(q, atoms[3]), f_atom(q, atoms[4]),f_atom(q, atoms[5])]
f_metal =[0, f_atom(q, atoms[0]), f_atom(q, atoms[1]), f_atom(q, atoms[2])]

#BULK DWF
dwfbulk = constants[2]
#Debye Waller factors in rms displacement units
dwbulk = np.exp(-(q**2 * constants[2]**2)/2)

#Debye Waller factors if in B units
#dwbulk = np.exp((-1*constants[2]*q**2)/((16*pi**2)))

#SURFACE DWFs
dwl = [0]   #DWFs FOR METAL
dwad = [0]  #DWFs FOR ADLAYERS
for i in xrange(1,4):
    #Isotropic DWF
    if ('idwf'+str(i) in params):
        #Is this q or qz?
        dwl.append(dwbulk*np.exp(-(qz**2*params['idwf'+str(i)].value**2)/2))

        #Adlayers   (only calculated for specular positions)
    if specular:
        if ('iaddwf'+str(i) in params):
            dwad.append(np.exp(-(qz**2*params['iaddwf'+str(i)].value**2)/2))

#Bulk contribution to structure factor
ftot = (f_metal[1]*dwbulk)/(1-np.exp(2*pi*1j*((h/3)-(k/3)-(l/3))))

#Commensurate metal layers
shift = 0       #cumulative shift in layer height
metal_layer=0
for i in xrange(1,4):
    #Coverage
    cov = params['coverage'+str(i)].value

    #Shift in layer height converted from angstroms, added to previous shift
    shift += params['eps'+str(i)].value/a3

    #Scattering from a metal layer with no shift
    metal_layer = f_metal[i]*dwl[i]*cov*np.exp(2*pi*1j*i*(-h/3 + k/3 +l/3))

    #Shift the metal layer and add to structure factor
    ftot += metal_layer*np.exp(2*pi*1j*shift*l)

toplayer = shift #keep the position of the top metal layer
adlayers = 0

#Incommensurate Ad-layers
if specular:
    #adlayer
    for j in xrange(1,4):
        #Check layer coverage, if non-zero calculate layers
        cov = params['adcoverage'+str(j)].value
        if (cov != 0) :
            #Calculate layer height converting from angstroms
            shift = toplayer + params['adeps'+str(j)].value/a3
            #Scatterig from a single layer*dwf*1 unit cell shift
            temp = (f_adlayer[j])*dwad[j]*np.exp(2*pi*1j*l)
            #Shift the layer and add to structure factor
            adlayers += temp*cov*np.exp(2*pi*1j*shift*l)
    ftot += adlayers

water = 0

#possible water models
```

```
if specular:
    #layered water structure
    cov = params['Layer'].value
    if(cov != 0):
        #read parameters
        sigma0 =  params['Lsigma0'].value
        sigmabar = params['Lsigmabar'].value
        spacing = params['Lspacing'].value
        #calulcate distace from top of metal
        dist =  params['Ldist'].value/a3 + toplayer
        #Scattering from layered model, defined above
        layered_water = cov*layered_model(sigma0,sigmabar,spacing,q,a)
                        *np.exp(2*pi*1j*dist*l)*np.exp(2*pi*1j*l)
        #add to structure factor
        ftot += layered_water
        #keep this so we can graph it
        water = layered_water

    #error function
    cov = params['Error'].value
    if(cov != 0):
        #read parameters
        sigma = params['Esigma'].value
        #calulcate distace from top of metal
        dist = params['Edist'].value/a3 + toplayer
        #Scattering from the error function defined about
        error = cov*Ferror_func(sigma,q, a)
                *np.exp(2*pi*1j*dist*l)*np.exp(2*pi*1j*l)
        #add to structure factor
        ftot += error
        #keep this so we can graph it
        water = error

amp = abs(ftot*np.conjugate(ftot))

#apply correction factor
corr_fac = 1
if(corrtype=="4c"):
    corr_fac = corr4c((h,k,l),q, qz ,qinp, params)
elif(corrtype=="diamond"):
    corr_fac = diamond((h,k,l),angles,params)
else:
    print "No correction factor used, you gave:",corrtype,"!"
ampcorr = amp*corr_fac*scale

return ampcorr, water, adlayers,corr_fac
```

This is an example parameter file used by the full unsimplified version of the program,
included to demonstrate the range of options available.

```
C   PARAMETER FILE
C   ----------------------
C   SYSTEM:   EXAMPLE PARAMETER FILE
C
C   Systematic Error on Data Points
C   ------------------------------------------------
E   0.05
C
C   RODS
C   ------------------------------------------------
C   SPEC        ROD1        ROD2
R   0   0       0   1       1   0
C
C   ATOMS
C   ------------------------------------------------
C   METAL1  METAL2  METAL3  ADL1    ADL2    ADL3
A   Pt      Pt      Pt      C       C       C
C
C   CONSTANTS                   (NO EFFECT)
C   ------------------------------------------------
C   a   wavelength  bulkdwf units(B/u)  Face(111/100)
K   3.924   0.68878     0.3722      B       111
C
C   PARAMETER   VALUE       MIN MAX VARY(T/F)
C   ------------------------------------------------
P   scale00     5.330053    1e-10   1e10    F
P   scale01     0.010913    1e-10   1e10    F
P   scale10     5.517442    1e-10   1e10    F
C
C   SURFACE METAL LAYERS
C   ------------------------------------------------
P   coverage1   1           0       2       F
P   eps1        0.006906    -.2     .2      T
P   idwf1       0           0       .1      F
C
P   coverage2   1           0       2       F
P   eps2        0.024294    -.5     .5      T
P   idwf2       0.035951    0.0     .1      T
C
P   coverage3   1           0.05    2       F
P   eps3        0.092075    -.2     .2      T
P   idwf3       0.104993    0.0     .2      T
C
C   For isotropic DWF use: idwf(i)
C   For anisotropic DWF use: adwfxy(i) and adwfz(i)
C   #Next three sections only effect specular rods
C
C   INCOMMESURATE ADLAYERS
C   ------------------------------------------------
P   adcoverage1 0.959825        0       4       T
P   adeps1      2.864291        1.5     7       T
P   iaddwf1     0.2             0       2       F
C
P   adcoverage2 1               0.0     1.5     T
P   adeps2      3.691403        2       12      T
P   iaddwf2     0.2             0.0     1.5     F
C
P   adcoverage3 0               0       4       F
P   adeps3      3.669524        1       15      F
P   iaddwf3     0.2             0.0     3       F
C
C   LIQUID MODEL layer
C   ------------------------------------------------
P   Layer       0               0       2       F
P   Lsigma0     0.2             0.001   10      F
P   Lsigmabar   0.5             0       5       F
P   Lspacing    3               2       10      F
P   Ldist       3               0       10      F
C
C   Error Function MODEL
C   ------------------------------------------------
P   Error       0.79            0       2       F
P   Esigma      0.5             0       5       F
```

```
P   Edist       4               3       15      T
C
C   Data File
C   ------------------------------------------------
F   data.dat
C
C   ------------------------------------------------------------
C   Diffo Step
C   ------------------------------------------------------------
C   Correction to apply to theory line
Z   diamond
C
C   Parameters needed for numerical beam profile/sample size calc
C   VERSLIT HORSLIT HORBEAM VERBEAM RADIUS  DSLIT
J   0.5     0.5     0.3     0.2     5.0     25
C
C   Scale Raw Data (usefull if integrated intensity is very small or big)
X   100000
C
C
C   Fitting Settings
C   ------------------------------------------------------------
C   Fitting Settings
C   ------------------------------------------------------------
C   Minimisation method [leastsq/nelder/lbfgsb] - Experimental
M   leastsq
C
C   Display Confidence Intervals (T/F)
C   WARNING: Will take some time to calculate after fit
C   Default errors are estimated from the diags of the covariance matrix
I   F
C
C   Enable Log File (T/F)
L   T
C
C   Show formated final values with errors (disable for full report) (T/F)
V   T
C
C   Ignore Specular fit (T/F)
S   F
C
C   Divde Final Fit by Correction Factor T/F)
G  T
C
C   Fitting Tolerences
C   ------------------------------------------------
C   FTOL        XTOL      MAXFEV
T   1.e-17      1.e-17    999999999
C
C   Help:
C   arg     Default Value   Description
C   ------------------------------------------------
C   xtol    1.e-7       Relative error in the approximate solution
C   ftol    1.e-7       Relative error in the desired sum of squares
C   maxfev  2000*(nvar+1)   maximum number of function calls
 (nvar= # of variables)
```